ABSTRACT

HIGH RESOLUTION STUDIES OF COMPLEX SOLAR ACTIVE REGIONS

by
Na Deng

Flares and Coronal Mass Ejections (CMEs) are energetic events, which can even impact the near-Earth environment and are the principal source of space weather. Most of them originate in solar active regions. The most violent events are produced in sunspots with a complex magnetic field topology. Studying their morphology and dynamics is helpful in understanding the energy accumulation and release mechanisms for flares and CMEs, which are intriguing problems in solar physics.

The study of complex active regions is based on high-resolution observations from space missions and new instruments at the Big Bear Solar Observatory (BBSO). Adaptive optics (AO) in combination with image restoration techniques (speckle masking imaging) can achieve improved image quality and a spatial resolution (about 100 km on the solar surface) close to the diffraction limit of BBSO's 65 cm vacuum telescope. Dopplergrams obtained with a two-dimensional imaging spectrometer combined with horizontal flow maps derived with Local Correlation Tracking (LCT) provide precise measurements of the three-dimensional velocity field in sunspots. Magnetic field measurements from ground- and space-based instruments complement these data.

At the outset of this study, the evolution and morphology of a typical round sunspot are described in some detail. The sunspot was followed from disk center to the limb, thus providing some insight into the geometry of the magnetic flux system. Having established a benchmark for a stable sunspot, the attention is turned to changes of the sunspot structure associated with flares and CMEs. Rapid penumbral decay and the strengthening of sunspot umbrae are manifestations of photospheric

magnetic field changes after a flare. These sudden intensity changes are interpreted as a result of magnetic reconnection during the flare, which causes the magnetic field lines to be turned from more inclined to more vertical. Strong photospheric shear flows along the flaring magnetic inversion line exist several hours before the flare. The footpoints of magnetic field lines are sheared by this motion and magnetic free energy is thus stored in the flux system. This energy is then suddenly released during the flare.

Based on multi-wavelength studies of these shear flows, a new challenging phenomenon is found. The local shear flow and magnetic shear can increase right after the flare. This apparently contradicts the principle of conservation of energy, which requires an overall decrease in the magnetic free energy that powers the flare. The explanation considers the emergence of a twisted or pre-sheared flux rope near the neutral line. Since shear flows are also detected in flare-quiet sunspots, the conclusion is made that they are associated with flare occurrence but they are not a sufficient condition for flaring.

HIGH RESOLUTION STUDIES OF COMPLEX SOLAR ACTIVE REGIONS

by
Na Deng

A Dissertation
Submitted to the Faculty of
New Jersey Institute of Technology and
Rutgers, The State University of New Jersey - Newark
in Partial Fulfillment of the Requirements for the Degree of
Doctor of Philosophy in Applied Physics

Federated Physics Department

January 2007

APPROVAL PAGE

HIGH RESOLUTION STUDIES OF COMPLEX SOLAR ACTIVE REGIONS

Na Deng

Dr. Carsten Denker, Dissertation Advisor — Date
Assistant Professor of Physics, NJIT

Dr. Haimin Wang, Co-advisor — Date
Distinguished Professor of Physics, Associate Director of Center for
Solar-Terrestrial Research and Big Bear Solar Observatory, NJIT

Dr. Philip R. Goode, Committee Member — Date
Distinguished Professor of Physics, Director of Center for
Solar-Terrestrial Research and Big Bear Solar Observatory, NJIT

Dr. Dale E. Gary, Committee Member — Date
Professor of Physics, Director of Solar Array in
Owens Valley Radio Observatory, NJIT

Dr. Zhen Wu, Committee Member — Date
Professor of Physics, Department Chair, Rutgers University - Newark

BIOGRAPHICAL SKETCH

Author: Na Deng

Degree: Doctor of Philosophy

Date: January 2007

Undergraduate and Graduate Education:

- Doctor of Philosophy in Applied Physics,
  New Jersey Institute of Technology, Newark, NJ, 2007
- Bachelor of Science in Physics,
  Nanjing University, Nanjing, China, 2001

Major: Applied Physics

Publications:

Deng, N., Tritschler, A., Liu, C., Wang, H., & Denker, C., 2007, *The Center to Limb Passage of a Sunspot in NOAA 10773*, The Astrophysical Journal, in preparation.

Deng, N., Xu, Y., Yang, G., Cao, W., Liu, C., Rimmele, T. R., Wang, H., & Denker, C., 2006, *Multi-Wavelength Study of Flow Fields in Flaring Super Active Region NOAA 10486*, The Astrophysical Journal, 644, 1278-1291.

Deng, N., Liu, C., Yang, G., Wang, H., & Denker C., 2005, *Rapid Penumbral Decay in Active Region NOAA 9026 Associated with an X2.3 Flare*, The Astrophysical Journal, 623, 1195-1201.

Liu, C., Lee, J., Yurchyshyn V., Deng, N., Cho, K., Karlicky, M., Gary, D. E., & Wang, H., 2007, *The Eruption from a Sigmoid Active Region on 2005 May 13*, The Astrophysical Journal, submitted.

Chen, W., Liu, C., Song, H., Deng, N., Tan, C., & Wang, H., 2007, *Statistical Study of Rapid Penumbral Decay Associated with Flares*, The Astrophysical Journal, submitted.

Denker, C., Naqvi, M., Deng, N., Tritschler, A., & Marquette, W. H., 2007, *The Synoptic Observing Program at Big Bear Solar Observatory*, Coimbra Solar Physics Meeting on the Physics of Chromospheric Plasmas, ASP Conference Series, Vol, xxx.

Denker, C., Deng, N., Yurchyshyn, V., & Tritschler, A., 2007a, *Two-Dimensional Spectroscopy of a Small δ Spot in Solar Active Region NOAA 10756*, Solar Physics, submitted.

Denker, C., Deng, N., Verdoni, A., Tritschler, A., & Rimmele, T. R., 2007b, *Field Dependent Adaptive Optics Correction Derived with the Spectral Ratio Technique*, Solar Physics, submitted.

Liu, C., Lee, J., Deng, N., Gary, D., & Wang, H., 2006, *Large-Scale Activities in the 2003 October 29 Flare*, The Astrophysical Journal, 642, 1205-1215.

Liu, C., Deng, N., Liu, Y., Falconer, D., Goode, P. R., Denker, C., & Wang, H., 2005, *Rapid Change of δ Spot Structure Associated with Seven Major Flares*, The Astrophysical Journal, 622, 722-736.

Wang, H., Liu, C., Qiu, J., Deng, N., Goode, P. R., & Denker, C., 2004, *Rapid Penumbral Decay Following Three X-Class Flares*, The Astrophysical Journal Letters, 601, L195-L198.

Wang, H., Ji, H., Schmahl, E. J., Qiu, J., Liu, C., & Deng, N., 2002, *Sudden Disappearance of a Small Sunspot Associated with the 2002 February 20 M2.4 Flare*, The Astrophysical Journal Letters, 580, L177-L180.

Presentations:

Deng, N., et al. *High-Resolution Studies of Complex Solar Active Regions*, AAS/Solar Physics Division Meeting, Durham, New Hampshire, June 25 - 30, 2006.

Deng, N., Xu, Y., Yang, G., Cao, W., Rimmele, T. R., Wang, H., & Denker, C. *On the Relation Between Flow Fields and Magnetic Field Evolution in Flare Productive NOAA Active Region 10486*, American Geophysical Union, Spring Meeting, New Orleans, Louisiana, May 23 - 27, 2005.

Deng, N., Liu, C., Wang, H., Denker, C., & NJIT/CFSTR Team *High Resolution Observations of Complex Magnetic Structure in Active Region NOAA 10375*, American Astronomical Society Meeting, Denver, Colorado, May 31 - June 3, 2004.

Deng, N., Liu, C., Yang, G., Wang, H., & Denker, C. *Rapid Penumbral Decay in Active Region NOAA 9026 Associated with Two X-Class Flares*, AAS/Solar Physics Division Meeting, Laurel, Maryland, June 16 - 20, 2003.

To my family,
for their endless love and encouragement.

ACKNOWLEDGMENT

I am very thankful for all the help I have received throughout my Ph.D. studies. The following words are just a small token of my gratitude.

I am full of gratitude to my advisor Dr. Carsten Denker for his great efforts on advising me all the way through a fresh Bachelor to a Ph.D. He has been giving me a great deal of guidance on computer techniques, IDL language, solar observations, solar physics knowledge and research. I am deeply thankful for his continuing support, encouragement and understanding. After his careful and excellent polishing, the language and contents of my final papers and thesis have improved significantly. His rigorous approach, attitude and conscientiousness in both scientific research and education has deeply affected me and will be of important value in my future career.

I am also heartily grateful to my co-advisor Dr. Haimin Wang, who gave me the opportunity to pursue a Ph.D. degree at NJIT. What impressed me most are his lectures, which are extraordinarily attractive, since he can make complicated physics easier to understand by extracting the essence and using intelligible examples. He has remarkable insight into frontiers of solar physics and always provides vital ideas or hints in my research. He is such a nice advisor that his concern reaches not only through our education and research but also to our life and spirit.

I would like to thank Dr. Philip Goode, Dr. Dale Gary, and Dr. Zhen Wu for being my committee members and taking time to read carefully the drafts of the dissertation and providing valuable feedback.

All the help from Dr. Alexandra Tritschler, Dr. Jiong Qiu, Dr. Vasyl Yurchyshyn, Dr. Jeongwoo Lee and Dr. Ju Jing is sincerely appreciated. Their valuable suggestions and discussions have contributed to the improvement of my knowledge and research. I thank Dr. Guo Yang, Dr. Yan Xu, and Dr. Wenda Cao for sharing their wonderful data and providing valuable discussions about my research

and career. My gratitude also goes to Dr. Louis Strous for his detailed explanations to my questions regarding the use of programs in ANA. I have also benefited much from the SPD Summer Schools on Helioseismology and High Energy Solar Physics.

BBSO and NSO have provided me precious observing opportunities. The staffs at BBSO and NSO gave me indispensable assistance and support. The work of Christine Oertel, the secretary at the Center for Solar-Terrestrial Research, facilitates our academic life and thus we can spend more time on research rather than on many tedious tasks. I really enjoy the warmth of the Center family consisting of all the fellow students, faculty and staff. They are always willing to provide help in my research and life.

Without the loving support of Dr. Chang Liu, my husband, colleague and friend, my Ph.D. research and life would not have been so joyful and smooth. His seriousness and enthusiasm in study and research continues to encourage me and spur me on.

This dissertation was supported by NSF under grant ATM 02-36945, ATM 03-13591, ATM 03-42560, ATM 05-48952, and MRI AST 00-79482 and by NASA under grant NAG 5-13661.

TABLE OF CONTENTS

TABLE OF CONTENTS
(Continued)

Chapter **Page**

LIST OF TABLES

LIST OF FIGURES

Figure **Page**

LIST OF FIGURES
(Continued)

Figure **Page**

LIST OF FIGURES
(Continued)

Figure **Page**

LIST OF FIGURES
(Continued)

Figure **Page**

LIST OF FIGURES
(Continued)

Figure **Page**

LIST OF FIGURES
(Continued)

Figure **Page**

CHAPTER 1

INTRODUCTION

The Sun is a magnetic and dynamic star. Rotation and differential rotation of the plasma generate complex magnetic fields on the Sun. The elementary magnetic flux tubes interact with convective plasma flows. They merge to form active regions where solar eruptive phenomena, such as flares, filament eruptions, and CMEs, occur and affect the Earth's environment. Studying complex solar active regions, especially in high-resolution, is necessary for understanding the fundamental physical processes of these eruptions and for mitigating their potential hazards to Earth. Before presenting the studies and results of this dissertation in Chapters 3, 4 and 5, the relevant background of solar active regions and eruptions will be briefly introduced in this chapter followed by methods of high-resolution solar observations in Chapter 2.

1.1 Solar Active Regions

Solar active regions are the sites of intense photospheric magnetic fields and extend along concentrated magnetic flux loops into chromosphere, transition region and corona. The manifestations of active regions are quite different in different wavelength and solar atmospheric layers. In the photosphere, they appear as dark sunspots with distinct boundaries between umbra, penumbra and quiet sun in continuum or white-light. In the chromosphere observed at Hα, the isolated sunspots merge into a larger complex background with many penumbral and super penumbral filaments and perhaps one or several overlying large filaments. Active regions begin to be bright and hot starting from the transition region and throughout the corona as observed in Extreme Ultraviolet (EUV) and X-ray images.

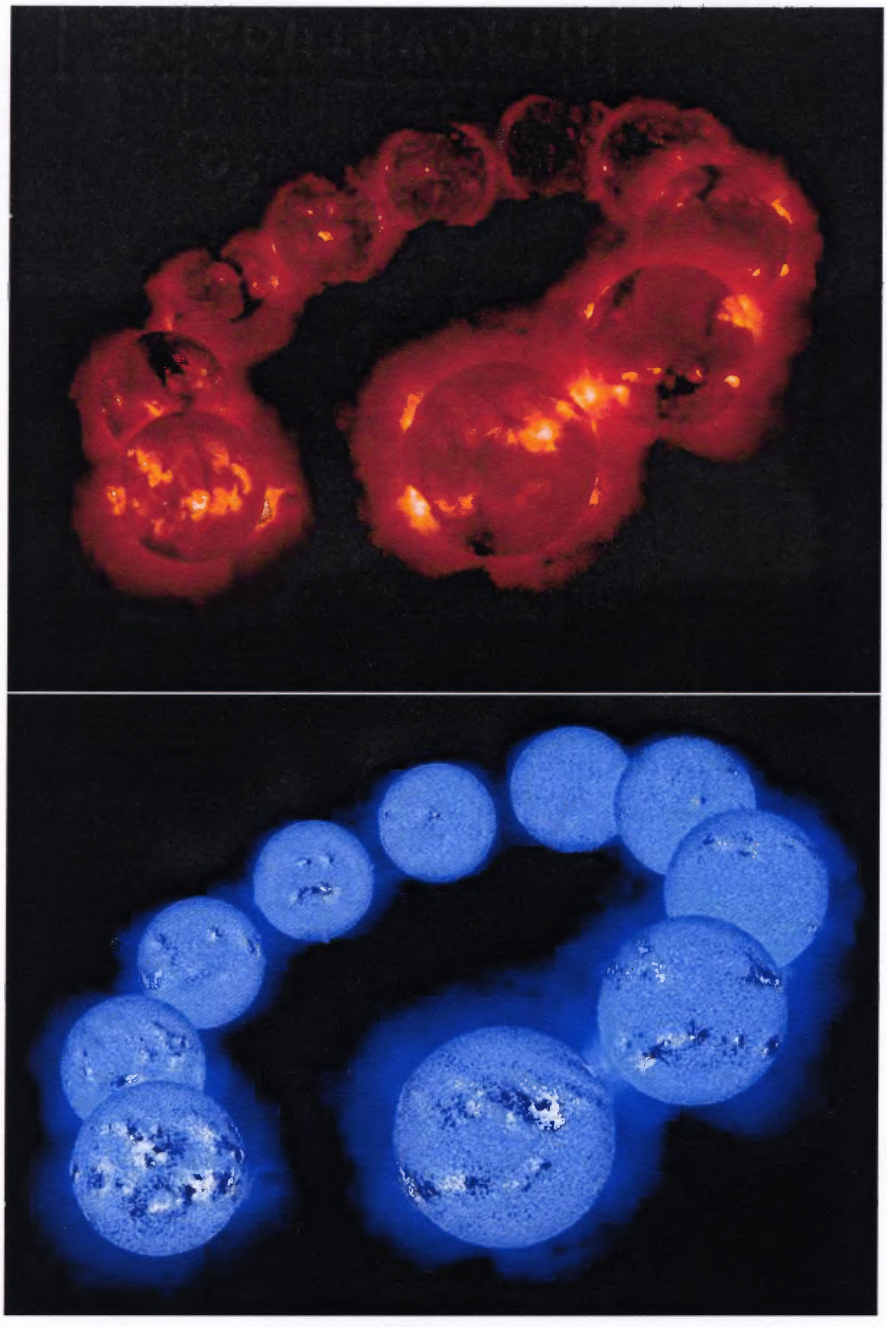

Figure 1.1 Time-series of the Sun in soft X-rays (top) and magnetic field strength (bottom) over a solar maximum-minimum-maximum period from 1992 to 2001. The magnetograms show the reversal of the magnetic polarity of active regions during solar minimum. This figure is adapted from http://solar.physics.montana.edu/sxt/Images/ The_Solar_Cycle_XRay_ med.jpg and http://sohowww.nascom.nasa.gov/spaceweather/lenticular /Solar_Cycle_blue.jpg

The unceasing motions at the base of active regions in the convection zone and subphotosphere govern the evolution of the magnetic topology in the solar atmosphere. Solar flares occur in situ when the magnetic configuration reaches a critical non-potential point, which in turn affects more or less the future evolution of the underlying base by changing the flux systems via magnetic reconnection.

Active regions vary over an 11-year period in emerging latitude, number, size, complexity and activity level, which is known as the cycle of solar activity, or the sunspot cycle, which is half of a complete 22-year magnetic cycle. The magnetic polarities reverse when starting a new solar cycle. Since dark sunspots only reflect magnetic field strength, not polarity, they show similar behavior in each 11-year half of the magnetic cycle. The appearance of sunspots at high latitudes ranging from 25° to 35° marks the beginning of a new solar cycle, when the sunspots are usually few, small, simple and inactive, corresponding to solar minimum. As time goes on toward solar maximum, more and more sunspots with increasing size and complexity appear in lower and lower latitude. They are located at latitudes between 15° and 20° during solar maximum, ranging about four to seven years after the start of the cycle. The Sun is most active at solar maximum, i.e., flares and CMEs occur most frequently and powerfully. Then the appearance of new sunspots keeps drifting toward the equator but with smaller number and lower activity. They lie within $\pm$ 10° of the solar equator near the end of the cycle, solar minimum again. In the meantime, a new solar cycle begins, repeating the behavior of the old one but with reversed magnetic polarities (Hale 1909; Hale et al. 1918). Figure 1.1 shows active regions in soft X-ray images and magnetograms and their variation over a solar maximum-minimum-maximum period.

The data in this thesis study were obtained from 2000 to 2006 and relate to the period of solar cycle 23 when it went from its maximum to minimum, in which the positive polarity leads the negative polarity in the northern hemisphere and the

situation is opposite in the southern hemisphere. In the next solar cycle 24 that is expected to start in 2007 and peak around 2012, the leading polarity will be negative in the northern hemisphere and positive in the southern hemisphere.

1.2 Sunspots

Sunspots are the manifestation of the strongest magnetic concentrations on the surface of the Sun. The umbra is the dark central part of a sunspot. The penumbra is a radial, filamentary structure surrounding the umbra. The magnetic field strength decreases gradually from about 3000 G at the center of the umbra to about 800 G at the outer part of the penumbra and vanishes abruptly slightly outside the penumbra (e.g., Denker 2005). In high-resolution observations, many fine structures in the umbra and penumbra, such as umbral dots, light bridges, penumbral grains and dark core, have been found, which makes it difficult to construct a comprehensive sunspot model. Sunspots can be classified by different methods. The frequently used one is the so-called Mt. Wilson classification, in which sunspots are classified as α, β, γ and δ types according to their morphology and magnetic complexity. $\beta\gamma\delta$ configurations are the most likely host for solar flares because they tend to store large amounts of magnetic free energy. δ-spots are also flare productive because strong magnetic gradient and shear are often observed near the magnetic neutral lines.

1.2.1 δ-spots

A δ-spot is formed when two sunspots with opposite polarities get close enough to each other such that a portion of magnetic flux of one polarity resides within the penumbra of the main sunspot of the other polarity (Künzel 1960; Zirin 1988). In other words, two magnetic polarities share a common penumbra. One must employ both white-light images and magnetograms to identify a δ-spot. Most δ-spots have strong localized magnetic shear between the two opposite polarities because penumbral fibrils

that trace the direction of photospheric magnetic fields lie nearly parallel to the magnetic inversion line (Zirin & Liggett 1987). The direct measurements of the magnetic fields using vector magnetographs also showed that the transverse fields are nearly parallel to the magnetic inversion line of δ-spots (e.g., Patty & Hagyard 1986; Zhang 1995). This magnetic shear naturally provides free energy that can be released violently in solar flares. A δ-spot is usually present in a multipolar active region that has several magnetic flux systems and neutral lines resulting in a complex coronal magnetic topology. Among these flux systems and in the corona somewhere above the δ-spot, there must exist a magnetic null-point, where magnetic reconnections often occur (Aulanier et al. 2000). Therefore, δ-spots are the most expected sites for flaring.

The origin of δ-spots is still under debate. They can be formed by contraction of flux tubes of different polarities in the photosphere. They can also exist before emerging from the photosphere. For example, Leka et al. (1996) observed the emergence of magnetic fields of a δ-spot with a pre-existing shear, while Linton et al. (1999) favors a global view of the formation of δ-spots, in which highly twisted flux tubes emerging from the subphotosphere by kink instability play the dominant role.

Due to the complexity of the δ-spot structure, the photospheric flow field is also rich in detail. Shear flows, which are defined as anti-parallel flows, usually exist in the penumbra of the δ-spot along its magnetic inversion line. The role of these shear flows in flare processes is still under debate (see, e.g., Lites et al. 2002).

1.2.2 Evershed Effect in Sunspot Penumbra

The respective red-shift and redward asymmetry of photospheric spectral lines at the limb-side and blue-shift and blueward asymmetry at the center-side of sunspots are collectively called the Evershed effect (Evershed 1909). The Evershed effect indicates an outward mass flow in the photospheric layers of penumbrae. Currently two models

are used to interpret the Evershed effect. One is the so-called "siphon flow" model, in which a magnetic flux tube forms an arch straddling two footpoints that have different gas pressure at the same geometrical height, the flow is then driven by a pressure difference from the high-pressure end to the low-pressure end. The second and more successful model is the "moving-tube model" (Schlichenmaier et al. 1998a,b), which is based on a simulation of the behavior of a thin flux tube. There the flux tube keeps rising adiabatically from the magnetopause until it meets the photosphere and suddenly bends in situ horizontally. A high temperature is sustained at the bending point by the up-flow of hot gas within the tube, which is interpreted as the observed bright penumbral grains. This model also yields a horizontal pressure gradient along the tube, which drives an outward flow, as in the siphon model.

1.3 Filament/Prominence Eruptions

Filaments and prominences are relatively cool and dense material suspended high in the hot and tenuous corona by the magnetic tension force of an arcade-type magnetic field (Priest 1982). They appear black on the bright solar disk (filament) and bright at the limb (prominence) against the dark background of space. They tend to lie along magnetic inversion lines in active regions or near polar regions. When the dynamical equilibrium is broken by continuous twisting of the filament, flux emergence near the magnetic arcade, or the movement of the anchor footpoints, the filament can erupt abruptly.

1.4 Flares

A solar flare is a sudden release (usually within minutes) of up to 10^{32} ergs of magnetic free energy via magnetic reconnection in the solar atmosphere, mostly in the corona. The released energy not only heats the local plasma up to 10^8 K (Chaisson & McMillan 2002) so that it emits electromagnetic radiation from X-rays, through

ultraviolet and visible light to radio emissions, but also accelerates particles to nearly relativistic velocities. Some of these energetic particles move outward and escape from the Sun producing Solar Energetic Particle (SEP) events and Type II radio bursts in the interplanetary space. Some of them move downward along magnetic flux tubes, impact and heat the Sun's lower atmosphere, and produce ribbon-like local brightenings in the chromosphere and photosphere. The particles may acquire their initial energy impulsively at the onset of the flare, or be accelerated over time by processes such as shock acceleration or stochastic acceleration (Miller et al. 1997).

Two-ribbon flares represent the majority of big and long-duration events (Svestka 2001). The standard two-ribbon flare scenario includes a filament or a sheared arcade above a current sheet of a magnetic inversion line (Priest 1982). When the entire structure loses its equilibrium, the flare begins, reconnection and the energy release occur at the current sheet, and the filament or the sheared arcade erupts outward (Priest 1982; Priest & Forbes 1986; van Ballegooijen & Martens 1989; Vrsnak 1990; Vrsnak et al. 1991). Some of the released energy is transported downward along the field lines by electron beams and thermal conduction to heat the transition region, chromosphere and even photosphere. Therefore, bright ribbons are formed at both sides of the magnetic inversion line. As the reconnection proceeds, outer field lines anchored at successively larger distances from the neutral line enter into the current sheet and reconnect, the manifestation of which is the outward expansion of the bright flare ribbons from the inversion line and the growth of the flare/postflare loops (Vrsnak 2005).

1.5 Coronal Mass Ejections

CMEs are the most powerful disturbances in the solar system and a main source of space weather effects. They are giant magnetic "bubbles" of ionized coronal material ejected radially outward from the Sun. They carry a large amount of coronal mass

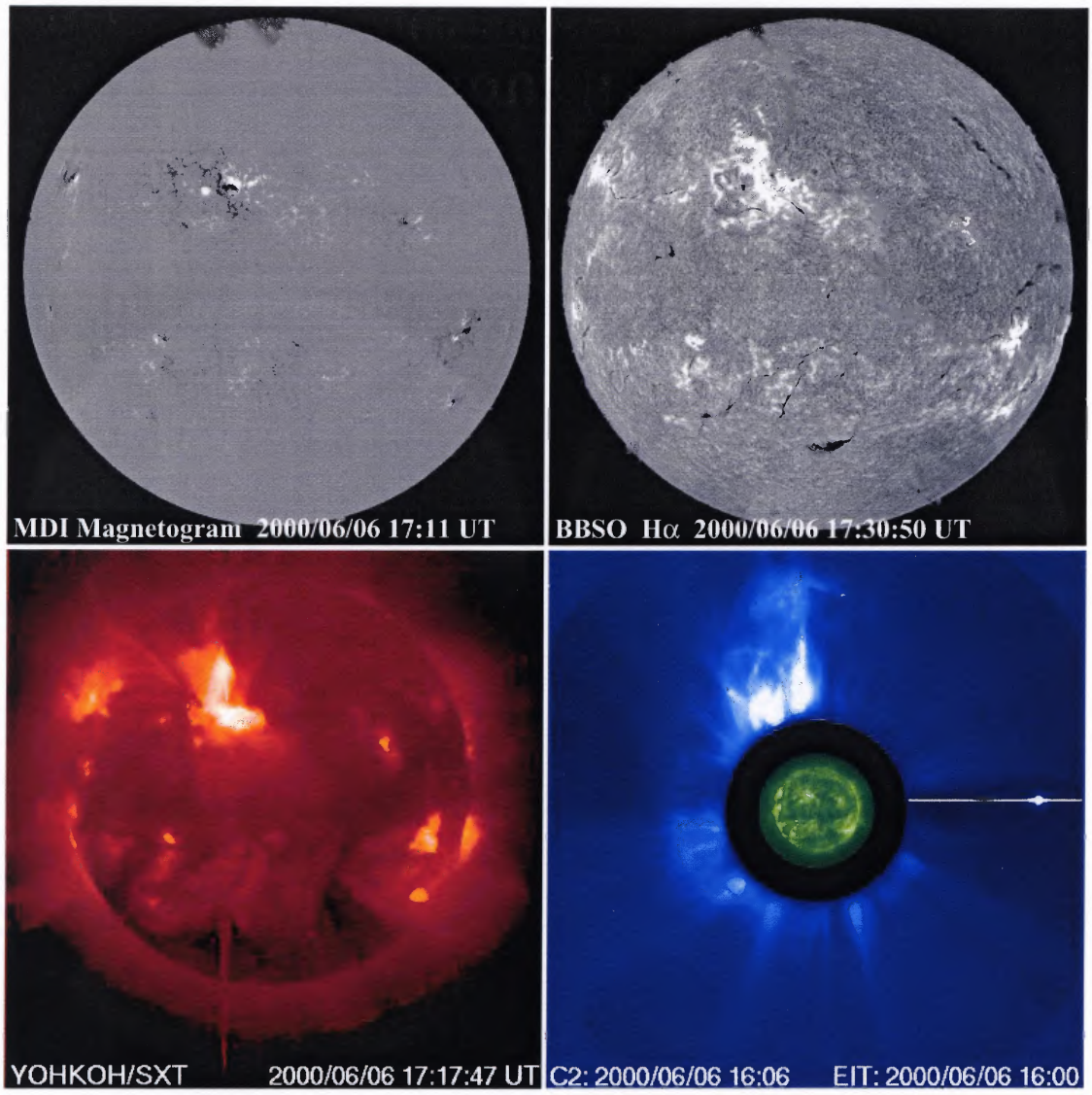

Figure 1.2 A particular type of solar eruptive event, i.e, a CME accompanied by a filament eruption and a two-ribbon flare. *Upper Left:* MDI magnetogram showing the magnetic field configuration in the photosphere. A δ-spot is located in the north-eastern part of the Sun. *Upper Right:* BBSO Hα image showing bright flare ribbons and an erupting filament lying on the magnetic inversion line of the δ-spot. *Lower Left:* Yohkoh soft X-ray image of the flare/postflare loops in the corona. *Lower Right:* LASCO C2 image of the associated halo-CME.

(10^{15} – 10^{16} g) and energy with fast speeds ranging from 100 to 2000 km s^{-1} (Gosling et al. 1976; Howard et al. 1985; St. Cyr et al. 1999). These magnetic field-carrying energetic eruptions, when directed toward Earth, can potentially cause hazardous effects on Earth and in the near Earth environment, especially when their magnetic fields happen to be oriented in a way such that they can reconnect with Earth's magnetic fields, thus affecting communications, the power grid, the safety of satellites and humans in space, etc. CMEs occur about once per week during solar minimum. While at times of solar maximum, their occurrence rate can be up to two or three times per day (Howard et al. 1985; Chaisson & McMillan 2002).

The CME accompanied by a filament eruption and a two-ribbon flare is a quite common type of solar eruptive phenomenon. A core structure is often observed in CMEs. This core is usually interpreted as the dense material that was previously contained in the filament/prominence (van Driel-Gesztelyi 2005). Many studies show that these three phenomena, flares, filament/prominence eruptions, and CMEs, occur at nearly the same time, which suggests that they are strongly correlated (e.g., Munro et al. 1979; Webb & Hundhausen 1987; Gilbert et al. 2000; Zhang et al. 2001; Zhou et al. 2003). Therefore, these three coronal phenomena may be connected by a common underlying physical mechanism.

Figure 1.2 shows an X2.3 two-ribbon flare/filament eruption/halo-CME event in large scale, which occurred in active region NOAA 9026 on 2000 June 6. To trace these phenomena back to the photosphere and to see what is their ultimate cause, high-resolution observations are needed that focus on the continuum structure and photospheric magnetic fields of their source active regions.

1.6 The Importance of High-Resolution Observations

Studying dynamic phenomena on small scales has the potential to shed more light onto global phenomena that are frequently encountered in the context of space

weather, e.g., flares, filament eruptions, and CMEs. As they are the primary cause of space weather disturbances, their properties, especially their ultimate origin, precursors, and near-Sun evolution need to be understood in order to predict them accurately. Since the source region of geo-effective CMEs can be usually identified with flares or filament eruptions, studying flare-producing active regions, e.g., their magnetic structure and evolution, is extremely important to understand the triggering, precursor, and underlying physics of the eruptions. In principle, non-eruptive active regions should receive the same attention for a comprehensive picture. Otherwise, the view of eruptive criteria might be skewed and one could diagnose eruption-associated signatures that might be common to non-eruptive scenarios as well. This is particularly true for high-resolution observations, which are rich in detail and highly dynamic.

For a long time, flares were considered to be phenomena merely in the solar atmosphere and they have no effect down to the photosphere and subphotosphere. One of the things that led to this belief was the lack of sufficient resolution to reveal the small but significant flare signatures in the photosphere. Because the pressure scale height and the photon mean free path of the solar atmosphere in the photosphere is in the order of $0.1''$ (Lites et al. 2004), spatial resolution on this order is needed to ultimately resolve the individual structures and discover the fundamental dynamic origins of flares, filament eruptions and CMEs. In summary, observations with high temporal, spatial, and spectral resolution as well as with sufficient magnetic sensitivity are vital in advancing the understanding of solar eruptive phenomena and how they affect the Earth and the near-Earth environment.

This research is focused on photospheric high-resolution observations of the morphology, vector flow, and magnetic fields of active regions with and without flare occurrence in order to find any flare-related changes or pre-cursors in the source sunspot group. New advanced instrumentation provides high temporal, spatial, and

spectral resolution data from ground- and space-based observatories, which places us finally in a position to discover the photospheric signatures of flares and CMEs. The observational results will have a strong impact on theoretical flare/CME models.

CHAPTER 2

HIGH-RESOLUTION SOLAR OBSERVATIONS

Since ancient times back to at least 5000 B.C., people have realized the importance of the Sun to life on Earth and begun to observe and study it (Kumar 2006). Nowadays, modern solar astronomy prepares to take the next steps in advancing our knowledge of the Sun. Ground-based solar observations are becoming more sophisticated, with larger and larger telescope apertures and more and more advanced techniques to achieve higher resolution and better quality solar images. Meanwhile, space-based solar observations provide important complementary information at wavelengths that cannot be observed from the ground, which contributes to a better and more comprehensive understanding of solar activity.

2.1 Ground-Based Solar Observations

Even though space-based solar observations have recently received more attention, observing the Sun from the ground is still an irreplaceable approach in studies of solar physics. All high-angular resolution studies are made using ground-based telescopes, since large-aperture telescopes (over 0.5 m) are only possible at present from the ground. On the ground, instruments are easier to operate and maintain. They also have long-term potentials of adjustment, repair, and upgrade.

2.1.1 Large-Aperture Solar Telescopes

According to the "Rayleigh criterion"

$$\theta_{min} = 1.22\frac{\lambda}{D}, \tag{2.1}$$

the angular resolution of a circular aperture telescope is dependent on its diameter, i.e., the larger the diameter, the smaller a feature can be resolved. Therefore, scientists have made great efforts on enlarging the aperture of telescopes. For example, in visible light and at diffraction-limit, the 65 cm vacuum reflector at BBSO has an angular resolution of 0.2″, the 76 cm Dunn Solar Telescope (DST) at the National Solar Observatory/Sacromento Peak (NSO/SP) has an angular resolution of 0.15″, and the 1 m Swedish Solar Telescope (SST) has an angular resolution of 0.12″. They have provided the finest detail and sharpest solar images so far. In particular, when the resolution reaches sizes comparable to the local pressure scale height on the solar surface, it can reveal structures in three spatial dimensions. The pressure scale height decreases from the outer to the inner Sun and with the decrease of the magnetic field strength. For example, the pressure scale height is about 60000 km in the lower corona and 500 km in the chromosphere. However, it is only of order 100 km in the photosphere. That is why with present resolution one can easily see 3D structures in the corona or chromosphere, but find it difficult to do so in the photosphere (Lites et al. 2004).

To resolve the fundamental feature and see 3D structure in the photosphere, an angular resolution down to 0.1″ or better is needed. Three main efforts are currently underway toward the unprecedented large-aperture telescopes, i.e., the GREGOR telescope on Tenerife of Spain (Volkmer et al. 2003), the New Solar Telescope (NST) at BBSO (Goode et al. 2003; Denker et al. 2006b), and the Advanced Technology Solar Telescope (ATST) led by the National Solar Observatory (Keil et al. 2003). GREGOR is a 1.5 m Gregory-type solar telescope with open structure currently being assembled by the German consortium (Volkmer et al. 2003). NST is a modern 1.6 m, off-axis telescope with an unobstructed aperture. It is currently under construction and expected to have first light in 2008 (Goode et al. 2003; Denker et al. 2006b). ATST is a 4 m, off-axis facility with open-air and all-reflecting design. It reaches the design

and technology limit of large-aperture solar telescopes. It has completed the design stage and is expected to commence operation in 2014 (Keil et al. 2003). The science goal of all these telescopes is to disentangle the basic processes of magneto-convection even at infrared wavelengths and to resolve the fundamental magnetic and flow scales in the photosphere and chromosphere.

2.1.2 Atmospheric Seeing

The biggest drawback of ground-based observations is summarized in the technical term: "seeing", which describes the sunlight propagating through the thick, non-uniform, and ever changing atmosphere of the Earth. In most cases, image resolution and quality are not determined by the telescope size but by the seeing conditions.

The Earth's atmosphere acts as a system of optical lenses with inhomogeneous refractive indices in front of the telescope entrance aperture and within the optical path of an open telescope before reaching the image detector. The air turbulence will cause spatial and temporal fluctuations of the refractive indices, therefore destroying the plane geometry of an incoming wavefront and distorting the image of the original object. The seeing effects include rigid image shift, differential image motion, image distortion or degradation, and image blurring. The biggest problem is image degradation and blurring, since they lead to information loss at high spatial frequencies. Even under good seeing conditions, the spatial resolution of a solar image is limited by seeing to about $1''$ (e.g., Denker et al. 2004b). For example, a 1-meter class telescope at 5000 Å could resolve a feature of 75 km on the Sun by mere optical constraints. However, the seeing severely limits the resolution to about 750 km. Without solving the seeing problem, the best attainable spatial resolution of solar observations in visible light corresponds to a diffraction-limited telescope of only 10 cm aperture.

In order to make the most of large-aperture telescopes, seeing must be overcome. Scientists have extensively thought about ways to overcome seeing effects. They are mainly in two domains. One is real-time optical compensation and correction, i.e., AO, in which a mirror is deformed in real-time to compensate for the wavefront aberrations. The other approach is post-facto image processing and restoration, e.g., speckle masking imaging, in which many degraded short-exposure images are taken within a short time period. They are used as input and produce a single image, which contains high spatial frequency information. Both of the two methods were used in this study. They will be discussed in detail in the next sections.

2.1.3 Adaptive Optics

AO is one of the most important tools for obtaining high-spatial resolution data. It is an approach to correcting wavefront distortions in real-time, where information of the atmospheric turbulence is extracted from images in real-time by wavefront sensor and immediately transferred to a deformable mirror to minimize seeing effects in a feed-back loop (Rimmele 2000).

The BBSO 65 cm vacuum reflector has been equipped with a high-order AO system since 2004. It was a collaboration with NSO/SP. The hardware, including a 97 actuator deformable mirror, a Shack-Hartmann wavefront sensor with 76 subapertures, and an off-the-shelf digital signal processor system, is almost identical to its twin AO system operated at the NSO Dunn Solar Telesope (Denker et al. 2006a). Figure 2.1 illustrates the optical layout of the AO system at BBSO designed by Didkovsky et al. (2003) and Ren et al. (2003). Its characteristics are summarized in Table 2.1. It feeds the Real-Time Image Restoration (RTIR) system and two imaging magnetograph systems (Denker et al. 2001), i.e., Visible-light Imaging Magnetograph (VIM) and InfraRed Imaging Magnetograph (IRIM).

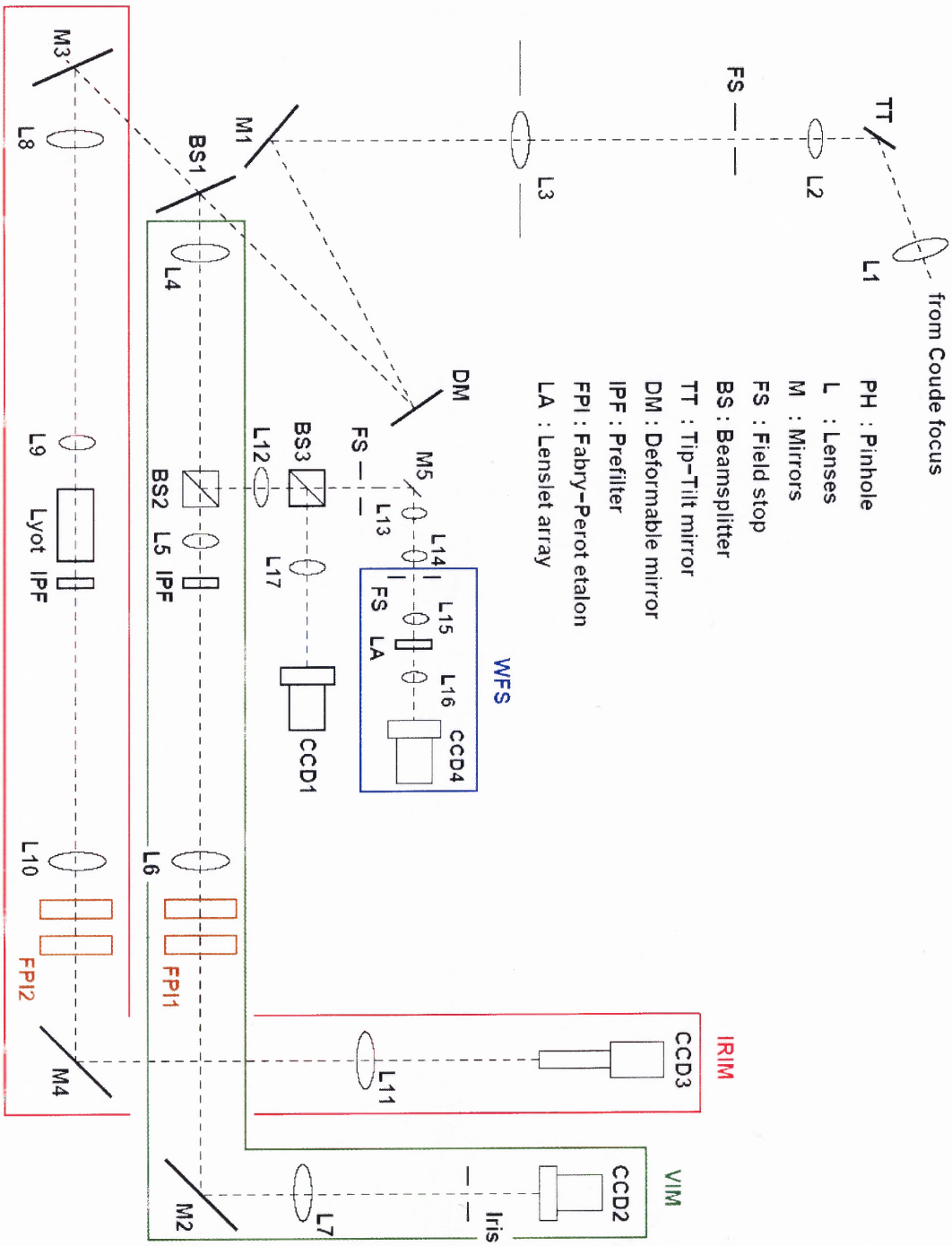

Figure 2.1 Sketch of the optical layout of the coudé light path and the AO system.

Table 2.1. BBSO AO System Characteristics (Denker et al. 2006a).

System Feature	
Corrected modes	35
Subapertures	76
Actuators	97
Bandwidth	120 Hz
Residual wavefront error	1.9 rad^2 (AO off)
Mean squared wavefront error	0.58 rad^2 (AO on)
Wavelength range for WFS	broadband visible
Intensity contrast (lock point)	~0.65 @ 5500 Å
Light fraction (WFS)	~5%

In summary, the AO imaging system is a complex optical and electronic system based on the combination of a wavefront sensor (WFS) measuring the wavefront deformations, a processor unit mapping the WFS measurements into real-time control signals, and a deformable mirror, whose face sheet can be modified at high speeds in response to electrical signals sent by the processor unit (Denker et al. 2006a).

2.1.4 Post-Facto Image Reconstruction

Image reconstruction is an objective approach to retrieving information that has been lost or obscured in the imaging process, based on mathematical and statistical models (Denker et al. 2004b; Löfdahl et al. 2007).

The *Atmospheric Seeing* section mentioned that seeing severely limit the effective resolution of a solar telescope. This is even more true for a long-exposure image, since the seeing conditions across the image keep changing during the exposure. For a short-exposure image, the situation is much better because the seeing or the wavefront aberrations can be frozen in the snapshot, resulting in conservation of the diffraction-limited information. In principle, the exposure time should be as short as possible, but it cannot be too short considering signal-to-noise ratio and photometric/polarimetric precision. What is then the upper limit of the exposure time

for such a snapshot? Based on experience, the typical seeing correlation time-scale for daytime observations is about 40 ms. Therefore, most short-exposure images used for image reconstructions are taken within a fraction of that, typically 10 ms or less (Denker et al. 2004b).

Although short-exposure images retain the diffraction-limited information, it is not the direct image of the real object, but rather an image modulated by the different instantaneous seeing conditions. To retrieve the information of the real object, large amounts of such short-exposure images are needed, from which the seeing conditions can be extracted and removed and the object information is restored and reinforced. Therefore, the foundation of many image restoration methods, such as speckle masking imaging, deconvolution techniques, wiener filter, phase diversity or blind deconvolution techniques, is a set of short-exposure data frames of the same object but with different phases of seeing induced wavefront aberrations. The underlying assumption is that all the short-exposure frames image the same unchanged object. However, the dynamic processes on the solar surface can violate this assumption as time goes on. Thus, the time to collect images containing sufficient statistical information on atmospheric turbulence has to be short. It is usually less than one minute for solar observations (Denker et al. 2004b).

In this section, the speckle masking restoration method that was used in this study will be described in some detail.

Spectral Ratio Technique (SRT) The core algorithm used in speckle masking reconstruction is the spectral ratio technique. In this section, the basic idea of SRT is introduced. It is adapted from Denker et al. (2007b).

The intensity distribution $i(\vec{x})$ in the focal plane of a telescope is given by the convolution of the intensity distribution of the object $i_0(\vec{x})$ and the point spread function (PSF) $s(\vec{x})$ that describes the atmospheric turbulence along the line-of-sight

(LOS). The imaging equation is

$$i(\vec{x}) = i_0(\vec{x}) * s(\vec{x}) \quad . \tag{2.2}$$

Fourier transformation of Equation 2.2 yields

$$I(\vec{q}) = I_0(\vec{q})S(\vec{q}) \quad , \tag{2.3}$$

where S is the Fourier transform of the PSF, which is called the optical transfer function (OTF). The upper case letters I and I_0 denote the Fourier transforms of the observed and the object intensity distribution, respectively. The two-dimensional spatial frequency $\vec{q}$ has been normalized with respect to the cut-off frequency $f_c = D/\lambda R$ of the telescope, where λ is the wavelength of the incident light, D the diameter and R the focal length of the telescope.

The spectral ratio (SR) is the ratio of long- and short-exposure power spectra of the observed intensity distribution, $|\langle I(\vec{q})\rangle|^2$ and $\langle |I(\vec{q})|^2\rangle$, which can be directly derived from the observations.

$$\mathcal{E}(\vec{q}) = \frac{|\langle I(\vec{q})\rangle|^2}{\langle |I(\vec{q})|^2\rangle} = \frac{|\langle I_0(\vec{q})\rangle|^2}{\langle |I_0(\vec{q})|^2\rangle}\frac{|\langle S(\vec{q})\rangle|^2}{\langle |S(\vec{q})|^2\rangle} = \frac{|I_0(\vec{q})|^2}{|I_0(\vec{q})|^2}\frac{|\langle S(\vec{q})\rangle|^2}{\langle |S(\vec{q})|^2\rangle} = \frac{|\langle S(\vec{q})\rangle|^2}{\langle |S(\vec{q})|^2\rangle} \quad , \tag{2.4}$$

where $\langle \ldots \rangle$ denotes an ensemble average. Assuming that the object intensity distribution is stationary, Equation 2.4 is independent of the object, since the power spectrum $|I_0(\vec{q})|^2$ of the object intensity distribution on the right side of the equation simply cancels resulting in only a ratio between long- and short-exposure transfer functions $|\langle S(\vec{q})\rangle|^2$ and $\langle |S(\vec{q})|^2\rangle$ (Fried 1966; Korff 1973). $\langle |S(\vec{q})|^2\rangle$ is the so called speckle transfer function (STF). $|S(\vec{q})|^2$, the modulus of the OTF, is the modulation transfer function (MTF). The two different average transfer functions $|\langle S(\vec{q})\rangle|^2$ and $\langle |S(\vec{q})|^2\rangle$ only depend on a single parameter — the Fried-parameter r_0 (Fried 1982), which is derived based on the theory of wave propagation through a turbulent medium (Kolmogorov turbulence).

The Fried-parameter r_0 describes the combined ground-layer and high altitude free atmosphere and therefore can be used to characterize the seeing conditions. Roughly, the Fried-parameter corresponds to the aperture of the largest telescope that would just be diffraction limited. The spectral ratio technique in turn is used to derive the Fried-parameter (von der Lühe 1984). To measure the Fried-parameter, the observed spectral ratios are compared with tabulated theoretical values of the STF (Korff 1973) and the average short-exposure MTF (Fried 1966).

Speckle Masking Imaging The light of a point source taking different paths through the turbulent atmosphere into the telescope will form randomly moving bright points in the focal plane of the telescope. These points are referred to as "speckles". Each speckle represents the diffraction-limited image of the point source. The individual speckles can be smeared out into the seeing disk when the exposure time is long (e.g., Denker et al. 2004b).

Speckle masking imaging requires a sequence of short-exposure images to separate the information of the object and of the atmospheric turbulence. In practical applications, the exposure time of each snapshot is set to 4 ms. Within 30 s, 200 short-exposure images are taken, from which the best 100 images with the highest rms-contrast are selected and saved in a burst that will be used to reconstruct one diffraction-limited image.

The reconstruction procedure works in the Fourier domain, where the influence of the atmospheric turbulence can be described by an amplitude reduction and phase modulation of the object's Fourier transform. The algorithm splits these two effects and treats them separately (de Boer 1993).

Before transforming the data into Fourier space, preprocessing must be carried out in real space for providing eligible input data. Each short-exposure image in the burst must first be dark- and flat-field corrected. Then the best image in the

burst (that with the highest rms-contrast) is selected to serve as a reference for removal of rigid and differential image displacements within the burst. Since speckle interferometry is only valid for a small region, the so-called isoplanatic patch, the images have to be divided into mosaics of partially overlapping small subimages that will be treated separately. Each subimage has a size of typically $5'' \times 5''$. For a 1024×1024 pixel image size and $0.14''$ resolution, which is the case of this study, a subimage size of 64×64 pixels is selected for fast computation, which results in 30×30 image stacks of such 50% overlapping subimages (Denker et al. 2005).

In the next steps, each stack of subimages is transformed into Fourier space and the spectral ratios are calculated, from which the quality of the seeing is computed. Based on the seeing quality, an empirical STF is selected to restore the amplitude of the Fourier transform of the object in the subimage.

The amplitudes of the object's Fourier transform are corrected according to the classical method of Labeyrie (1970)

$$|I_0(\vec{q})|^2 = \frac{\langle |I(\vec{q})|^2 \rangle}{\langle |S(\vec{q})|^2 \rangle} \quad . \tag{2.5}$$

To derive the phases of the object's Fourier transform, the speckle masking method (Weigelt 1977; Weigelt & Wirnitzer 1983; Lohmann et al. 1983; de Boer 1993) is used.

$$\langle I^3(\vec{q},\vec{p}) \rangle = I_0^3(\vec{q},\vec{p}) \langle S^3(\vec{q},\vec{p}) \rangle \quad , \tag{2.6}$$

where $I^3(\vec{q},\vec{p}) = I(\vec{q})I(\vec{p})I^*(\vec{q}+\vec{p})$ is the speckle masking bispectrum and $*$ denotes a conjugate complex quantity, $\langle S^3(\vec{q},\vec{p}) \rangle$ is the average speckle masking transfer function (SMTF). A detailed description of the technical aspects of the phase reconstruction algorithm is given by Pehlemann & von der Lühe (1989). A sensitive noise filter (de Boer 1996) is applied during the calculation of these phases.

Putting the modulus and phases of the object's Fourier transform together and transforming them back to spatial domain yields a mosaic of partially overlapping

speckle reconstructed small subimages. They are aligned and connected very accurately to form the final full reconstructed image (Denker et al. 2005).

2.1.5 Combination of AO and Speckle Masking Imaging

Generally, AO systems can only operate in a partially compensating mode leaving a residual wave front error. In addition, AO systems are innately imperfect, since the number of corrected modes is finite and consequently higher order modes are not corrected. A much better compensation can be obtained by combining real-time AO with post-facto image restoration techniques such as speckle masking imaging (Denker et al. 2005).

This section will present an example of such combination based on the most recent observations taken at BBSO. It is adapted from Denker et al. (2007b).

AO senses and effectively compensates only low order aberrations of the optical system implying that higher orders are only partially compensated. The uncompensated fraction of the wavefront error can vary considerably with seeing. Speckle imaging takes all residual aberrations into account.

A generalized Fried-parameter can be derived after partial wavefront compensation with an AO system (Cagigal & Canales 2000). If the atmospheric turbulence profile is known for a specific site and time, the generalized Fried-parameter

$$r_0 = \left[0.423k^2 \sec\phi \int_0^Z C_n^2(z)\,dz\right]^{-3/5} \quad \text{[cm]} \tag{2.7}$$

and the isoplanatic angle

$$\theta_0 = \left[2.91k^2 \sec^{8/3}\phi \int_0^Z C_n^2(z) z^{5/3}\,dz\right]^{-3/5} \quad [\mu\text{rad}] \tag{2.8}$$

can be calculated. In Equations 2.7 and 2.8, k represents the wavenumber $(2\pi/\lambda)$, ϕ is the zenith angle, z is the height above ground, and C_n^2 is the index of refraction structure constant (Roddier 1981).

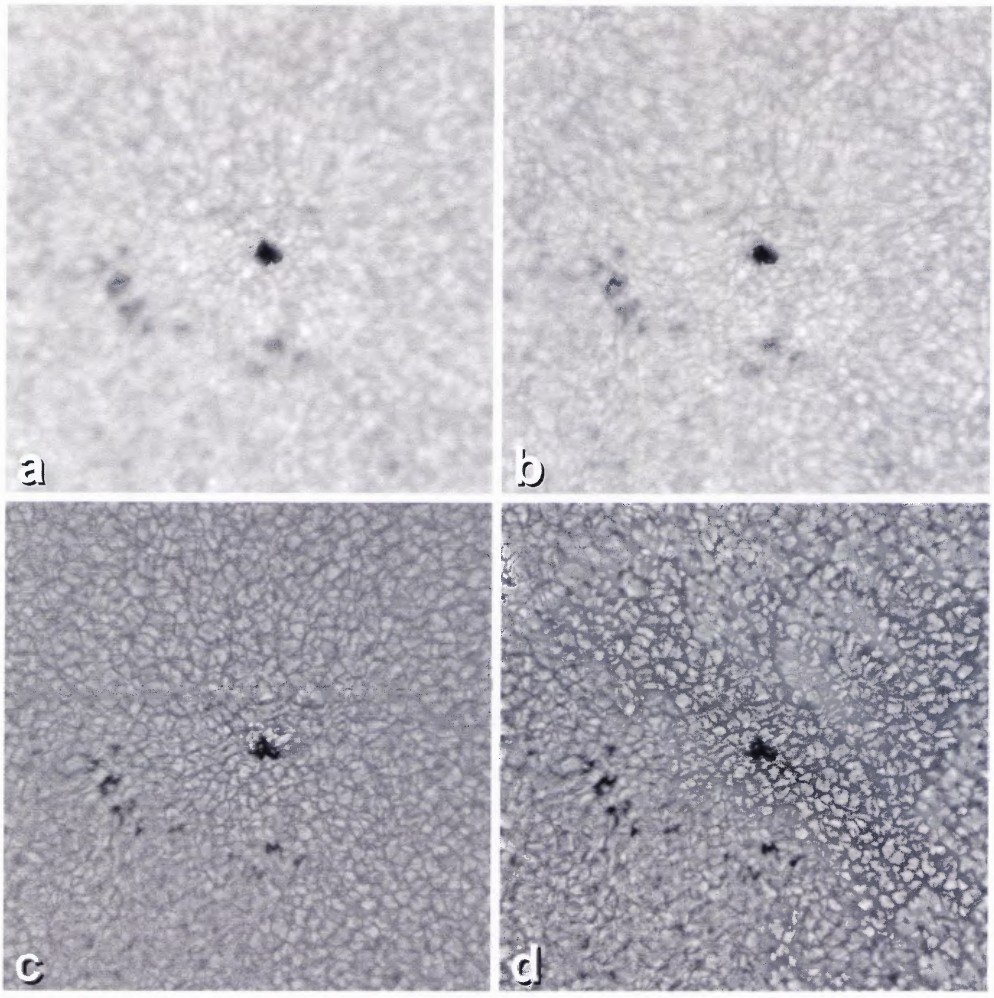

Figure 2.2 High resolution observations of solar active region NOAA 10803 observed at 17:12 UT on 2005 August 30 with the 65 cm vacuum telescope at BBSO. (a) Long-exposure image, (b) short-exposure image, (c) speckle restoration with constant STF, and (d) speckle restoration with field dependent STF (Figure 1 in Denker et al. 2007b).

Figure 2.2 illustrates different stages of the speckle masking image restoration process in combination with AO. Figure 2.2a shows the long-exposure image (400 ms effective exposure time), which is the average of 100 short-exposure images. The short-exposure (4 ms) image with the highest granular rms-contrast is depicted in Figure 2.2b. Both images clearly demonstrate the AO correction for an extended object such as the Sun. The correction near the lock point of the AO, i.e., the small

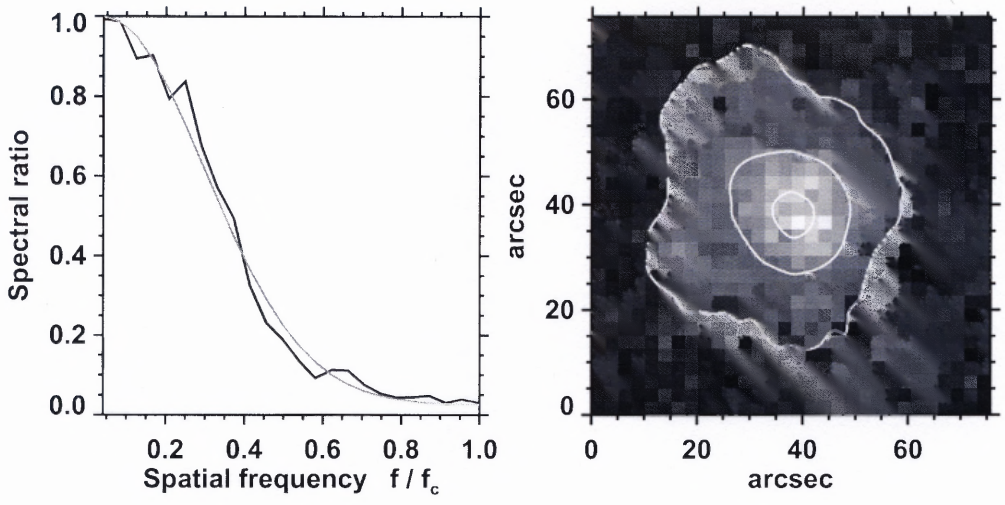

Figure 2.3 *Left:* Azimuthal average of the spectral ratio for a single isoplanatic patch in the center of Figure 2.2. *Right:* Field dependence based on the standard deviation of the SR f_σ/f_c. SRs were determined for 30×30 isoplanatic patches covering a FOV of about $75.6'' \times 75.6''$. The white contour lines correspond to $f_\sigma/f_c = 0.20$, 0.25 and 0.30, respectively. The data were smoothed before computing the contours (Figure 2 in Denker et al. 2007b).

pore in the center of the field-of-view (FOV), is much higher than in the periphery of the image. If a single STF is used to restore each of the 30×30 isoplanatic patches (see Figure 2.2c), the Fourier amplitudes will be over-corrected near the AO lock point and underestimated at the periphery. Note that the generalized Fried-parameter r_0 derived from AO corrected data no longer describes the combined ground-layer and free atmosphere and should not be used as a measure of the seeing conditions. Therefore, it is necessary to find appropriate STFs for the entire FOV, which properly calibrate the Fourier amplitudes. An example based on semi-empirical STFs is shown in Figure 2.2d. The field dependence of the STFs was derived with SRT. The long- and short-exposure transfer functions (Fried 1966; Korff 1973) were scaled such that the granular contrast is an accordance with theoretical models (e.g., Stein & Nordlund 1998) and speckle observations obtained without AO (e.g., Wilken et al. 1997). This method is very similar to Method B in Puschmann & Sailer (2006).

The performance of field dependent AO correction can be measured by SRT. The left panel in Figure 2.3 shows the azimuthal average of the two-dimensional SR $\mathcal{E}(\vec{q})$ (see Equation 2.4) as a black curve, which was measured in the central part of NOAA 10803 (see Figure 2.2). Since individual SRs tend to be noisy, a Gaussian fit was applied (gray curve) to determine the standard deviation σ of the SRs. The non-linear least squares Gaussian fit is using a gradient expansion algorithm with the assumption that the maximum is unity and located at the lowest frequency. The only free fit parameters were a constant offset to reflect the noise characteristics and the standard deviation σ of the SRs. The standard deviation is expressed as a spatial frequency f_σ normalized with respect to the cut-off frequency f_c of the telescope. The gray scale image in the right panel of Figure 2.3 represents f_σ. Each square corresponds to one of the 30×30 isoplanatic patches in the FOV. The white contour lines indicate the diminished AO correction with distance from the AO lock point. The contours of the normalized spatial frequencies related to the standard deviation of the SRs increase from the periphery to the center of the FOV. The respective values are $f_\sigma/f_c = 0.20$, 0.25 and 0.30. These contour levels were chosen mainly for display purposes and do not necessarily carry any specific scientific meaning. A simple four subimage-wide boxcar average has been applied to smooth the contour lines.

2.1.6 Two-Dimensional Imaging Spectrometer

Some parts of this section were adapted from Denker et al. (2007a). As for now, the VIM system at BBSO is used just as a two-dimensional imaging spectrometer. Polarization optics will be added to the imaging spectrometer in 2007, which will enable the measurement of the full Stokes vector. Then VIM will become a true spectro-polarimeter. The design of the imaging magnetograph systems at BBSO has been outlined in Denker et al. (2003a,b). The two-dimensional imaging spectrometer was carefully tested, which includes a detailed characterization of the Fabry-Pérot

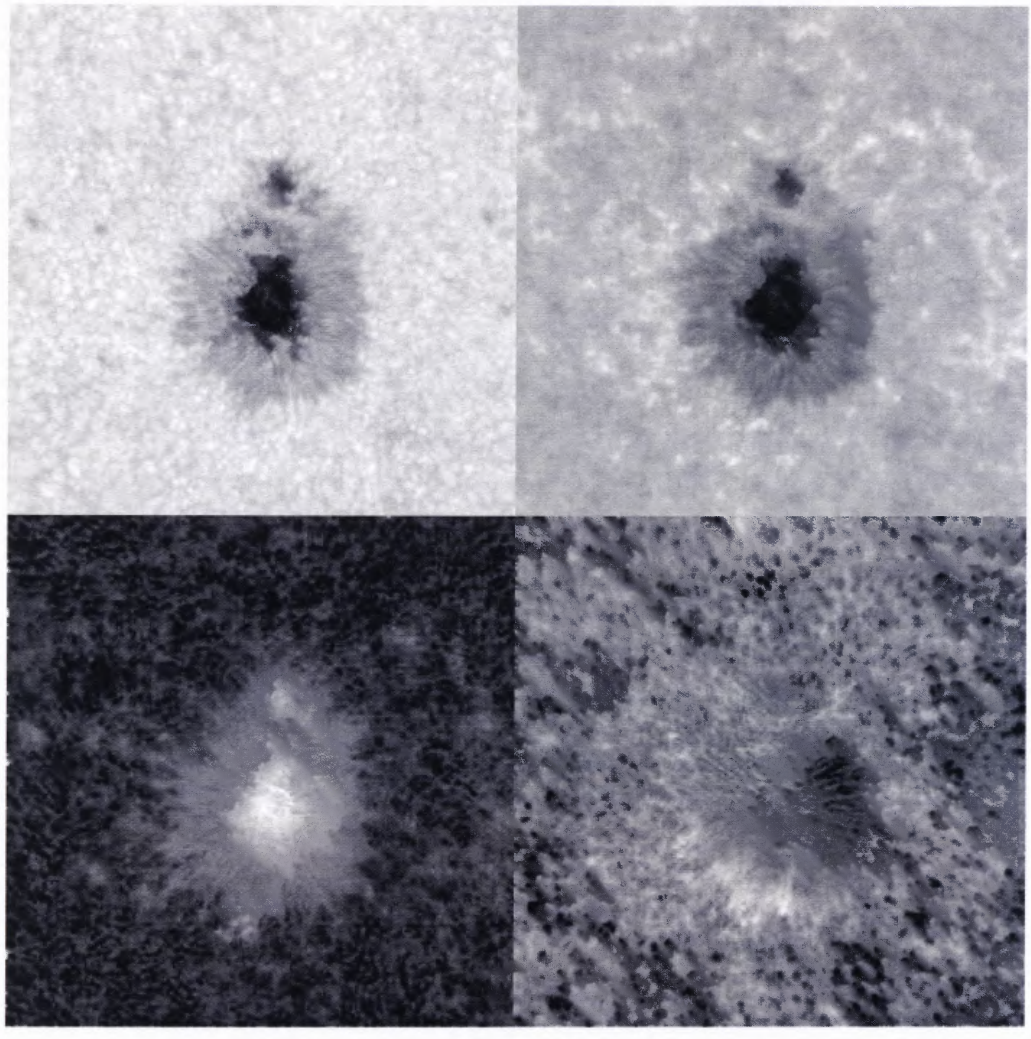

Figure 2.4 *Upper Left:* Continuum image. *Upper Right:* Line-core image. *Lower Left:* Line-FWHM image. *Lower Right:* Dopplergram. They are the output of the two-dimensional imaging spectrometer at BBSO.

etalon (Denker & Tritschler 2005). The two-dimensional spectroscopic observations were made in the Fe I 6301.5 Å line. They have a FOV of about $84'' \times 84''$. The CCD camera is usually operated in a 2×2 pixel binning mode, thus, the image scale is about $0.16''$ pixel^{-1}. The cadence of the spectral line scans is typically 16–19 s and a total of about 200 scans can be obtained in one observing run. The filtergrams are taken at 91 wavelength points in the Fe I line separated by 1.2 pm corresponding to a

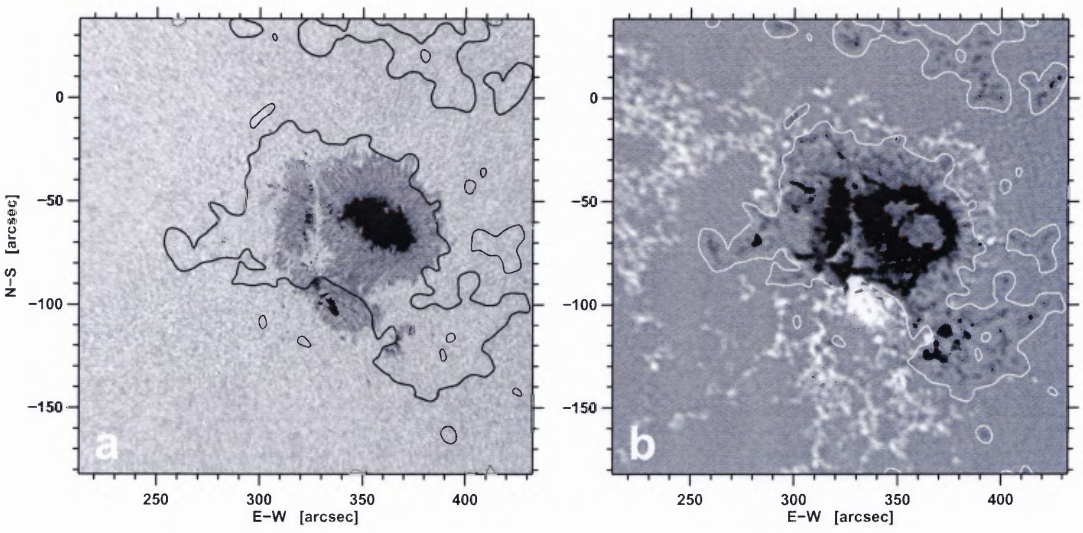

Figure 2.5 (a) Ca I 6103 Å line wing filtergram and (b) longitudinal magnetogram obtained with BBSO's DVMG system at 17:52 UT on 2005 May 2. The magnetogram is displayed between ±500 G and the black (a) and white (b) contours represent the magnetic polarity inversion line (Figure 1 in Denker et al. 2007a).

scanned wavelength interval of 1.1 Å. The exposure time of the filtergrams is usually 80 ms.

The output of the two-dimensional imaging spectrometer includes the continuum image, the line-core image that shows information in the highest layer of the line formation range, the image of the FWHM of the spectral line that hints at the magnetic field strength, and the Dopplergram showing the LOS velocity. Figure 2.4 illustrates the aforementioned VIM output. The advantages of a Fabry-Pérot-based two-dimensional imaging spetrometer are the high-spatial resolution, fast data acquisition, and the possibility of post-facto image restoration. While the disadvantage is the only moderate spectral resolution compared to the grating-based spectrograph.

Next, the high-resolution observations of solar active region NOAA 10756 on 2005 May 2 will be presented based on two-dimensional imaging spectroscopy and speckle masking imaging at BBSO.

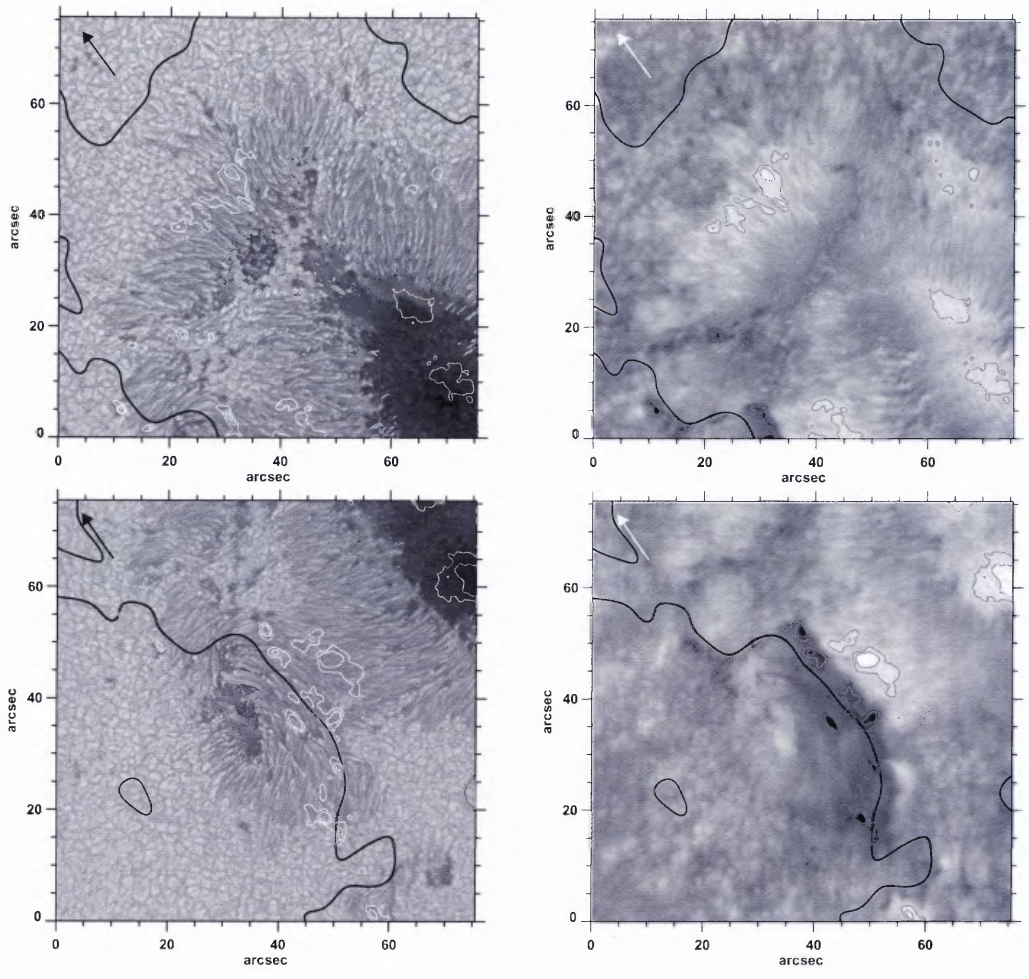

Figure 2.6 *Left Column:* Speckle reconstructions of the north-east and south-east parts of active region NOAA 10756 obtained on 2005 May 2 with BBSO's 65 cm vacuum reflector. The δ spot is located in the center of the lower left panel. *Right Column:* The respective Dopplergrams displayed in the range of ± 1.25 km s^{-1} obtained with VIM system. In all the panels, the thick black contours represent the magnetic polarity inversion line, the thin contours outline regions with LOS speeds greater than 0.8 and 1.0 km s^{-1}, respectively, the arrows in the upper left corner indicate the direction toward disk center (Figures 2 and 3 in Denker et al. 2007a).

Figure 2.5 shows the entire active region in a quasi-continuum image and a LOS magnetogram obtained with the Digital Vector Magnetograph (DVMG, Spirock et al. 2001). A small δ-configuration with opposite polarity can be found in the southern part of the region. Note that the magnetogram shown in Figure 2.5 has only a moderate spatial resolution of about $1''$. The spatial resolution can improve to $0.2''$ with VIM in the near future, thus providing highly detailed and accurate measurements of the photospheric magnetic field.

The small δ-configuration was targeted by the 65 cm reflector with AO, speckle imaging and VIM for high-resolution studies. Figure 2.6 shows the high-spatial resolution speckle reconstructed white-light images and Dopplergrams in two parts of the active region including the small δ-configuration. Strong LOS velocity kernels were observed near the magnetic polarity inversion line of the δ-configuration. After applying LCT to the one-hour-long time-series of speckle restored images, strong horizontal shear flows were found along the same magnetic inversion line. Figure 2.7 depicts the horizontal flow field near the δ-configuration in separate azimuth and speed maps.

The δ-configuration plus the strong horizontal shear and vertical flows on the two sides of the magnetic inversion line were considered as an important pre-flare signature. Yang et al. (2004) and Deng et al. (2006) have observed such strong and persistent horizontal and vertical shear flows along the main magnetic inversion line in a complex sunspot before a major flare. The results from Deng et al. (2006) will be presented in Chapter 5 of this dissertation. Therefore, flare eruptions were expected in the δ-configuration triggered by these shear flows. However, NOAA 10756 was very quiet without any major flares occurring throughout the observing run. After investigating the larger structure of the active region extending from photosphere, through chromosphere, to the corona using Hα and EUV images, a magnetic field topology that was close to potential was found in the large-scale flux system of

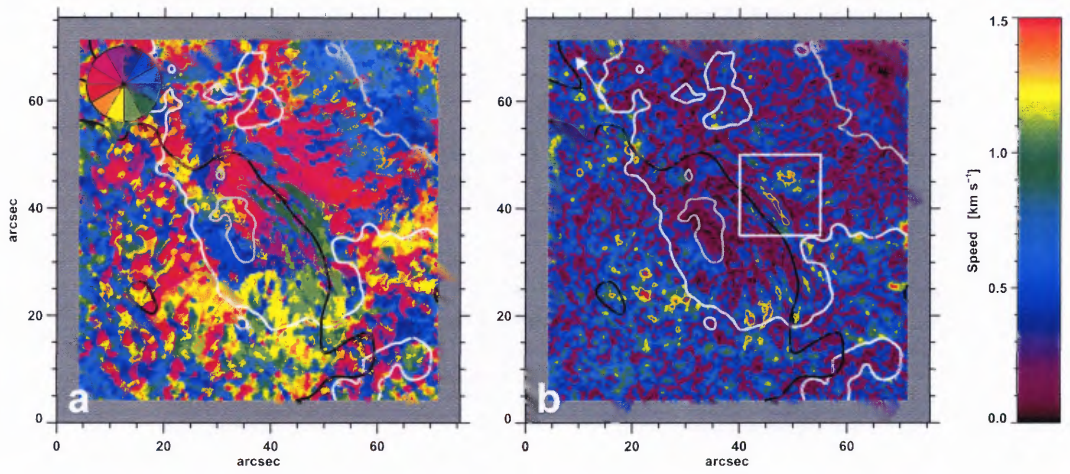

Figure 2.7 Horizontal flow fields in NOAA 10756 (southern part). LCT was applied to a sequence of 60 speckle reconstructions obtained during the time period from 17:40 UT to 18:10 UT on 2005 May 2. The white box indicates the region with strong horizontal shear flows (Figure 5 in Denker et al. 2007a).

the active region, which may account for the quiet state of the active region. Combining the shear flow observations from this quiescent sunspot and from the very active sunspot (Yang et al. 2004; Deng et al. 2006), a conclusion is made that the photospheric shear flow observed in active regions is associated with flare occurrence but it is not a sufficient condition for flaring.

2.2 Space-Based Solar Observations

Many satellites have been launched into space to observe the Sun during the last decades (Kumar 2006), including NASA's Orbiting Solar Observatories (OSO), Solar Maximum Mission (SMM), the European Space Agency/NASA Ulysses probe, Japan/US/UK Yohkoh (also called Solar-A), the Solar and Heliospheric Observatory (SOHO), the Transition Region and Coronal Explorer (TRACE), the Reuven Ramaty High Energy Solar Spectroscopic Imager (RHESSI), as well as recent efforts of Solar-B now named Hinode (Japanese for "Sunrise"), Solar TErrestrial RElations Observatory (STEREO), and Solar Dynamics Observatory (SDO).

SOHO, TRACE, and RHESSI have provided significant complementary data for this study. Hinode, STEREO, and SDO will play a more important role in solar research in the near future.

The primary scientific goals of SOHO include (1) to answer basic questions about solar corona and solar wind, such as, how is the solar corona formed and heated? What is the physical process to give rise of coronal material to the expanding solar wind? (2) to investigate the fundamental causes of activities observed on the solar surface, and (3) to infer the interior structure of the Sun (Domingo et al. 1995). It has very accurate pointing in order to perform its mission of helioseismology study. Therefore, the data from SOHO can be used as a reference in the co-alignment between different data sources. The Michelson Doppler Imager (MDI) (Scherrer et al. 1995) on board SOHO provides a unique opportunity to study the structure and evolution of the longitudinal component of magnetic and velocity fields by continuously taking full-disk data.

TRACE observes the Sun in multi-wavelengths, mostly in the ultraviolet (UV) and EUV ranges that are formed in chromosphere, transition region, and lower corona. TRACE has provided spectacular images of the 3D structure of magnetic loops in the solar atmosphere, which give us clues on coronal heating and trigger mechanisms of solar flares (Handy et al. 1999; Schrijver et al. 1999).

RHESSI targets high-energy solar physics in hard X-rays, typically related to solar flares. Its scientific aims include particle acceleration and energy release mechanisms during solar flares (Lin et al. 2002).

Observing the Sun from space outside the Earth's atmosphere avoids seeing. More importantly, since Earth's atmosphere blocks much of the solar electromagnetic spectrum and particle radiation, they can only be observed in space. The main drawbacks of space-based observations are the high cost and risk, the limited aperture, the complex technology, and the short lifetime. Despite these shortcomings, space-

based observations have made major contributions in advancing solar physics studies and will help to answer many of the intriguing questions related to solar eruptions and space weather.

CHAPTER 3

THE CENTER-TO-LIMB PASSAGE OF A SIMPLE SUNSPOT

In this chapter, high-resolution observations during the decaying phase of a simple sunspot are presented. The sunspot was continuously observed over several days at BBSO using AO, high-cadence speckle masking imaging, and the two-dimensional spectrometer. The evolution of its morphology and flow fields is studied in detail. This work is on-going and will be submitted to the Astrophysical Journal (Deng et al. 2007).

3.1 Abstract

High-resolution observations of a simple, almost round, decaying sunspot are presented during the passage of the sunspot from disk center to the limb. Daily, diffraction-limited, AO-corrected, 30 minute-long time sequences of active region NOAA 10773 were obtained from 2005 June 7 to June 12 with the 65 cm vacuum reflector at BBSO. White-light images and two-dimensional spectroscopic data were obtained almost simultaneously. The speckle masking technique was applied to AO-corrected white-light images to further improve the image quality and spatial resolution. The evolution of sunspot characteristics has been studied, including sunspot area and the center-to-limb-variation (CLV) of penumbral and umbral contrasts. LCT (November et al. 1986) was applied to the time-series of restored white-light images providing two-dimensional maps of transverse flow fields. A distinct dividing line was observed between radially inward and outward optical flows in the penumbra. This dividing line can be correlated with moving flux tubes in the penumbra. Two-dimensional maps of Doppler velocities with sub-arcsecond resolution

were derived from imaging spectroscopy, which show the Evershed effect during the decaying phase of the sunspot.

3.2 Introduction

The properties and photometric evolution of sunspots have been extensively studied for centuries (see, e.g., Solanki 2003; Howard & Murdin 2000, and references therein). Only recently, continuous, high-resolution, ground-based observations with a spatial resolution of $0.2''$ or better became available (e.g., Thomas & Weiss 2004, and references therein). These data are the result of AO correction and image restoration, which enable studies of sunspot evolution that require several days of observations with consistent high quality. This chapter provides an example of such an effort obtained with new post-focus instruments at BBSO. Photometric properties of a decaying sunspot will be studied, including its size, umbral and penumbral contrasts, and the Evershed effect and related flow fields.

The decay of sunspots is still an elusive problem in sunspot physics. It raises the question of how the magnetic flux of sunspots is dissipated in the photosphere (Martínez Pillet 2002)? Sunspot decay can occur at any time: during the growing phase of the active region, as soon as the sunspot is completely formed, or after a long standing stable state (McIntosh 1981). Chapman et al. (2003) analyzed the decay properties of many sunspots at the San Fernando Observatory (SFO). They find a strong correlation of the sunspot decay rate with the total sunspot area and the umbral to total area ratio. Meanwhile, they find a non-significant correlation between the decay rate and the radius of the sunspot. They claim that the decay rate is not a constant. Bray & Loughhead (1964) observed that when a pore's extension is greater than 3.5 Mm ($\sim 5''$), penumbral structure will begin to develop around it. According to the mirror process of the formation and decay of a penumbra mentioned in Leka & Skumanich (1998), the penumbra may disappear when the diameter of the umbra

is smaller than 3.5 Mm. The formation and decay of penumbrae does not seem to be a phenomenon immediately related to the variance of the sunspot magnetic flux, but a phenomenon related to the dramatic change in the photospheric convection and flow field around the flux concentration (Weiss et al. 1996). Indeed, Leka & Skumanich (1998) find that the umbral flux does not decrease during the formation of its penumbra. Furthermore, there is no significant increase in the total magnetic flux of the sunspot once the penumbra is formed (Zwaan 1992).

A widely used observable to study the thermal stratification of active regions is the CLV of the sunspot's brightness contrast, which provides necessary boundary conditions for theoretical models of energy transport in active regions (Solanki 2003). The brightness contrast, for the umbra for example, is defined as $\alpha = 1 - I_U/I_{QS}$, where I_U/I_{QS} is umbra/photosphere intensity ratio. However, observations are still ambiguous. One result is that I_U increases towards the limb resulting in a decrease in the umbral contrast (Rödberg 1966; Wittmann & Schröter 1969; Schatten 1993). The other result is that the umbral contrast has almost no net change with $\mu = \cos\theta$ (θ is the heliocentric angle) even though I_U decreases towards the limb in some measurements (Albregtsen & Maltby 1981a,b; Maltby et al. 1986). On the other hand, several semi-empirical umbral models (e.g., Zwaan 1974, 1975; Kollatschny et al. 1980) have predicted an increase in the umbral contrast toward the limb, which was verified by investigations of the umbral limb-darkening in the infrared spectral range (Albregtsen et al. 1984). Various authors (e.g., Zwaan 1968; Maltby & Mykland 1969; Maltby 1970, 1972; Wöhl et al. 1970; Bray 1981) have separately measured umbral and penumbral contrasts. They range between $\alpha_U = 0.5 - 0.8$ and $\alpha_P = 0.15 - 0.25$, respectively.

The respective red-shift and redward asymmetry of photospheric spectral lines at the limb-side and blue-shift and blueward asymmetry at the center-side of sunspots are collectively called the Evershed effect (Evershed 1909). In general, the degree

of the line shift and asymmetry increases from the inner to the outer edge of the penumbra (Solanki 2003). The Evershed effect indicates an outward mass flow in the photospheric layers of penumbrae. A penumbral sector immediately displays Evershed flow after its formation. Leka & Skumanich (1998) and Yang et al. (2003) detected Evershed flow as soon as the penumbral magnetic field lines are inclined. Rimmele & Marino (2006) observed individual Evershed flow channels and studied their temporal evolution. They confirm that penumbral grains are the inner footpoints of horizontal Evershed flows where a hot upflow occurs. There are significant similarities between the upflow and horizontal flow in their behavior and evolution, which suggests that they belong to a common feature. Evidence of downflows in the outer penumbra have been found in other studies (e.g., Rimmele 1995; Westendorp Plaza et al. 1997; Schlichenmaier & Schmidt 1999, 2000; Schmidt & Schlichenmaier 2000), which suggest a convex structure of Evershed flow and returning flux back to the solar interior in the surroundings of the sunspot.

November et al. (1986) applied LCT to time-series of a sunspot and observed a radial outflow in the penumbra, which extended into the adjacent photosphere, forming an annulus about 5″-wide around the sunspot. An inward motion of bright and possibly dark features in the inner penumbra and outward motion in the outer penumbra have been observed by many authors (e.g., Schröter 1962; Muller 1976; Toenjes & Woehl 1982; Kitai 1986; Zirin & Wang 1989; Wang & Zirin 1992; Molowny-Horas 1994; Denker 1998; Lites et al. 1998; Sobotka et al. 1999; Bovelet & Wiehr 2003). In particular, Molowny-Horas (1994) observed inside the penumbra a ring-like area of approximately zero horizontal velocity and positive divergence dividing the penumbra into two regions. Inward flows occurred predominantly in the inner region with an average velocity of 0.29 km s^{-1}, whereas outward flows took place mostly in the outer part of the penumbra, where they reach velocities as high as 1.5 km s^{-1} with an average velocity of 0.5 km s^{-1}. Denker (1998) also observed this line of

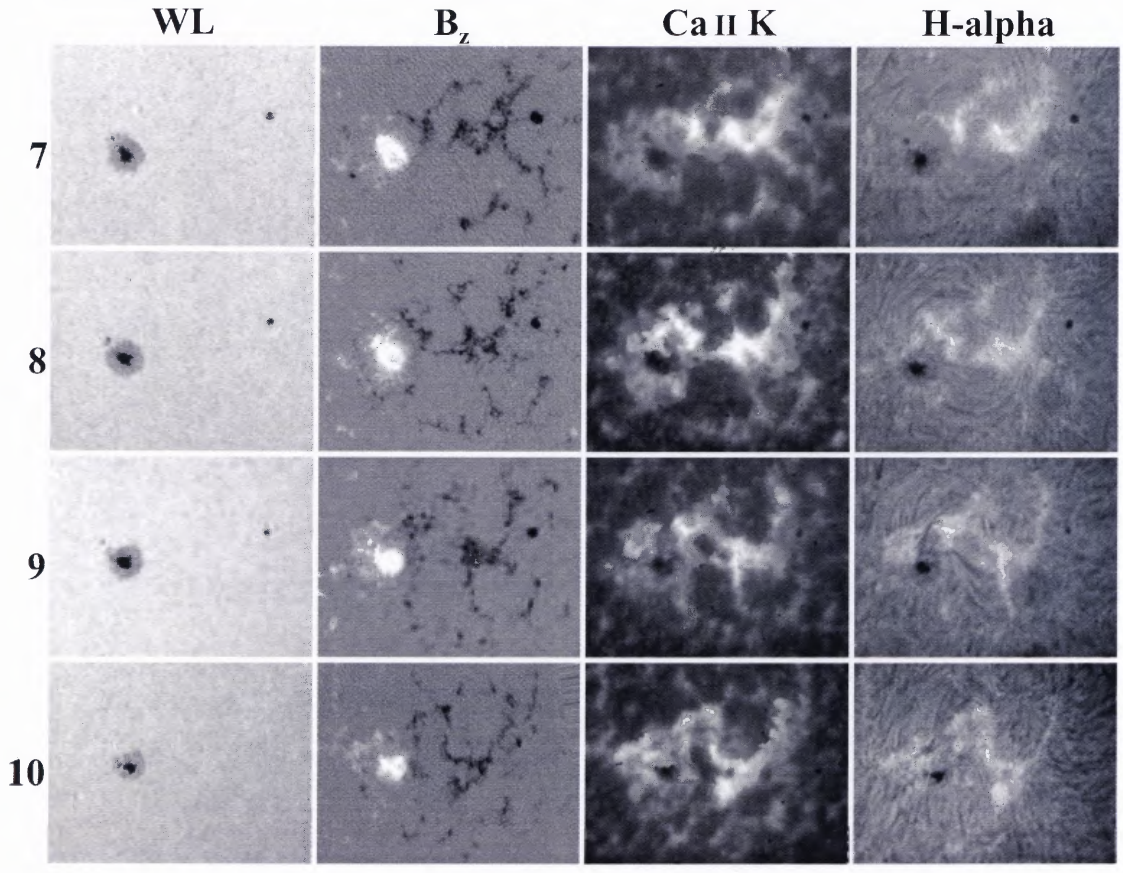

Figure 3.1 Evolution of active region NOAA 10773 from 2005 June 7 to 10. The columns (from left to right) represent white-light (WL) images, LOS magnetic field (B_z), and Ca II K and Hα filtergrams.

positive divergence with horizontal velocity near zero in the middle of the penumbra dividing the inward and outward flow using images restored with the speckle masking technique as input for LCT. The line of positive divergence may result from rising flux tubes when their footpoints, indicated by the bright penumbral grains, move towards the umbra (Wang & Zirin 1992; Molowny-Horas 1994). This idea is consistent with the moving tube model presented by Schlichenmaier et al. (1998a,b).

3.3 Observations

The observations were performed with BBSO's 65 cm vacuum reflector using its new high-order AO system (Rimmele et al. 2004; Denker et al. 2006a). An isolated,

small, slightly asymmetric, round sunspot was observed in active region NOAA 10773 during its disk passage from disk center to the limb. The data were obtained on five days: 2005 June 7 ($\mu \approx 0.965$), June 8 ($\mu \approx 0.947$), June 10 ($\mu \approx 0.770$), June 11 ($\mu \approx 0.608$), and June 12 ($\mu \approx 0.434$). NOAA 10773 was also monitored every day by BBSO's 25 cm refractor. These data include vector magnetograms and Hα and Ca II K filtergrams.

Figure 3.1 shows the whole active region and its evolution in white-light (WL) images, LOS magnetograms, and Ca II K and Hα filtergrams mostly observed by BBSO's 25 cm refractor. On June 9, the WL and B_z data are from MDI, since no synoptic BBSO data were available. The active region was in the south hemisphere (S15°). The relatively stable and round spot at the left side in the panels of Figure 3.1 is a following spot (in the sense of solar rotation and magnetic polarities) with positive magnetic polarity. The high-resolution observations with BBSO's 65 cm reflector were targeting this spot. The leading spot on the right side is otherwise small and has less concentrated magnetic field. This configuration is an exception of most normal cases, in which the more stable and concentrated spot should be the leading spot. The bright areas in Ca II K and Hα filtergrams trace the plage regions that are spatially correlated with magnetic fields.

White-light images at 6000 $\pm$ 50 Å and two-dimensional spectroscopic data were almost simultaneously obtained on two optical benches in the coudé laboratory of the 65 cm telescope. Both data sets were AO-corrected. Every 30 seconds, the best 100 short-exposure (10 ms) white-light images were automatically selected from 200 frames captured at 15 frames s^{-1} with a fast CCD camera system for image restoration. These 100 short-exposure and AO-corrected images were combined to create one restored image using speckle masking image reconstruction (e.g., Denker et al. 2005, and references therein). The cadences of the speckle restored images and the spectroscopic data are about 30 s and 20 s, respectively.

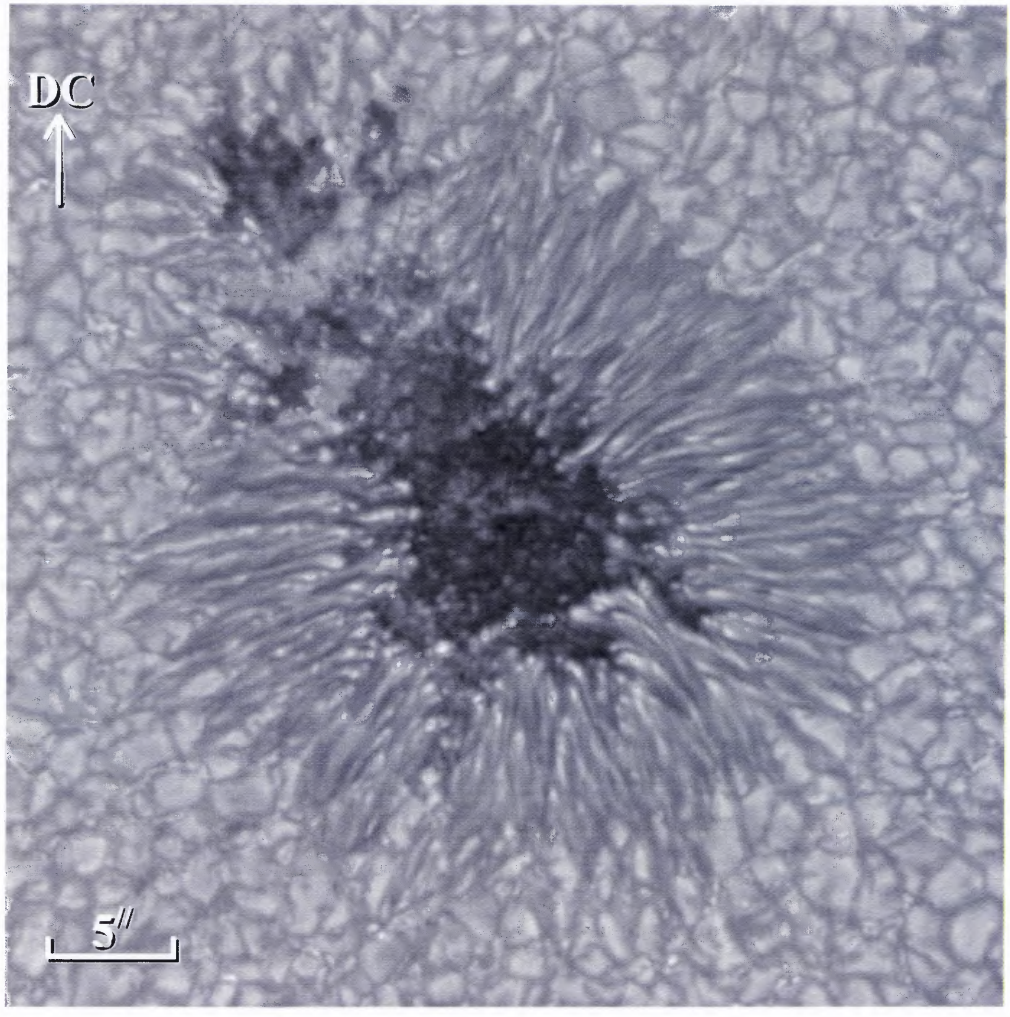

Figure 3.2 Speckle reconstructed white-light image of the following sunspot in active region NOAA 10773 on 2005 June 7. The white arrow points towards disk center (DC).

The FOV of the speckle restored images is about $79'' \times 79''$ with an image scale of about $0.07''$ pixel^{-1}. The two-dimensional spectroscopic observations in the Fe I 6301.5 Å line have a slightly larger FOV of $84'' \times 84''$. The CCD camera was operated in a 2×2 pixel binning mode. Thus, the image scale was about $0.14''$ pixel^{-1}. The filtergrams were taken at 91 wavelength points in the Fe I line separated by 1.2 pm corresponding to a scanned wavelength interval of 1.1 Å. The exposure time of the filtergrams was 80 ms. Each observing run typically lasted 30 min, resulting in 60

speckle reconstructed white-light images and 100 two-dimensional spectroscopic data sets as one data sequence. After this sequence, the AO wavefront sensor needed to be re-aligned to take the pupil rotation into account. Time and seeing permitting, this observing and alignment procedure was repeated. In this study, the best 30-minute data sequence was selected for each observing day. Further details of the observations are given by Denker et al. (2007b), who provide a detailed description of the high-resolution observations and a performance evaluation of the AO system.

Figure 3.2 is one of the high-resolution speckle reconstructed white-light images of the sunspot observed on June 7, which clearly shows the sunspot fine structures, such as numerous umbral dots, the dark cores in the penumbral grains, and the twist and writhe of the penumbral fibrils. The penumbral grains are brighter in the limb-side than those in the center-side penumbra.

3.4 Data Reduction

The speckle reconstructed white-light images and spectroscopic data in each sequence were first aligned for each data set and then carefully co-aligned with the other data. The white-light images were also co-aligned with the corresponding MDI intensity images in order to acquire accurate locations and orientations of the sunspot on different days. Note that image rotation is not corrected by any optical means and has to be compensated in the data analysis. A subsonic filter was applied to the time-series of white-light and spectroscopic data in order to remove the 5-minute oscillation and residual seeing distortions.

Dopplergrams were obtained with the imaging spectrometer. The LOS velocity is determined by a Fourier phase method, which uses the entire line profile to determine the line center position and is very insensitive to noise. The convention is followed that redshifts are positive and blueshifts are negative. Thus, bright areas in the Dopplergrams move away from the observer, while dark areas move towards the

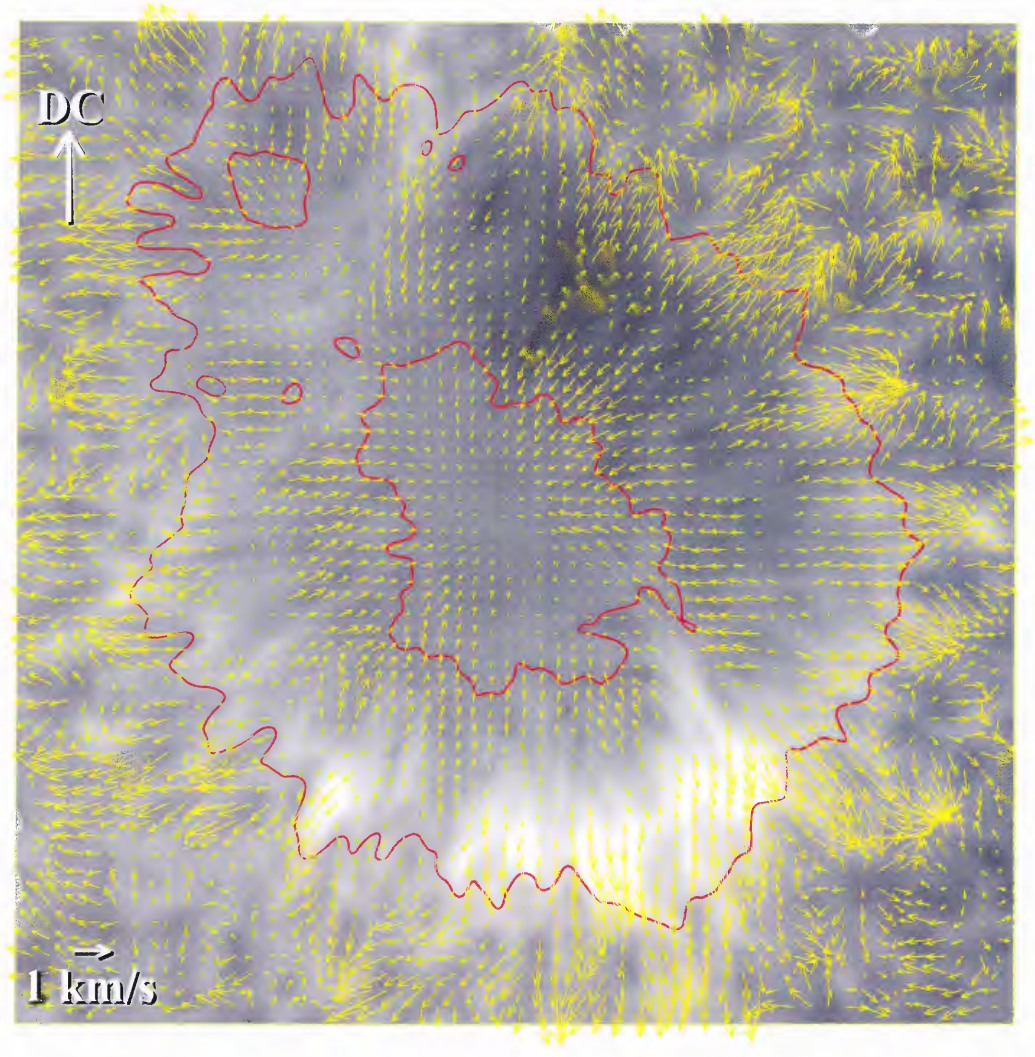

Figure 3.3 Three-dimensional flow field of the following sunspot in NOAA 10773. Arrows show a 30-minute average of horizontal LCT flow fields derived from speckle restored images. The gray-scale background image represents the LOS velocity, which is the 30-minute average of Dopplergrams derived from two-dimensional spectroscopy. Redshifts are positive and correspond to bright areas.

observer. The Fe I 6301.5 Å line is broadened by the Zeeman effect. Thus, the LOS velocities are entangled with asymmetries of the line profiles caused by unresolved magnetic flux tubes. This limitation will cause some errors in the final results. These ambiguities will be avoided by acquiring pre-filters for the imaging spectrograph for non-Zeeman ($g = 0$) lines. Since a wavelength reference is missing for the absolute line positions, the Doppler maps are calibrated using MDI Dopplergrams as reference,

although MDI uses the Ni I 6767.8 Å line, which forms at slightly different heights. Since the long-term evolution of flow fields in the sunspot will be determined from disk center to the limb, geometrical corrections have to be applied. The solar rotation signal is subtracted from the Doppler images first and then the overall offset between BBSO and MDI Dopplergrams for the same FOV is subtracted.

LCT was applied to the speckle reconstructed white-light time-series resulting in 59 individual flow maps. The average of the 59 individual LCT flow maps represents the observed average transverse flow over 30 min. The average of 100 individually calibrated Dopplergrams represents the observed average LOS flow for the same time period. The combination of the two averaged flow maps gives the observed 3D flow field. Figure 3.3 shows the combined high-resolution three-dimensional flow field of NOAA 10773 on 2006 June 7.

Inverse cork maps can be used to visualize the divergence of a flow field (Molowny-Horas 1994). The same technique is used here, i.e., 22,500 corks (artificial tracer particles) are distributed evenly across the LCT flow field and their movements are traced for 10 h backwards in time. The corks will concentrate at locations of the strongest divergences of the flow field. The resulting cork map traces the location of the dividing line between inward and outward flows in sunspot penumbrae. Figure 3.4 shows the evolution of the sunspot over six days in speckle reconstructed white-light images. The perspective foreshortening has been corrected based on the sunspot's locations on the Sun. The white contours show the borders of umbra and penumbra. The yellow dots correspond to the corks, which are concentrated along lines in the middle of the penumbra. The first panel is a line core intensity image at Fe I 6301.5 Å containing information in higher photospheric layers. It shows small-scale brightenings in the vicinity of the sunspot known as "line gaps" (e.g., Wiehr et al. 2004). These features are related to small-scale magnetic fields, which can be seen as moving magnetic features in magnetograms.

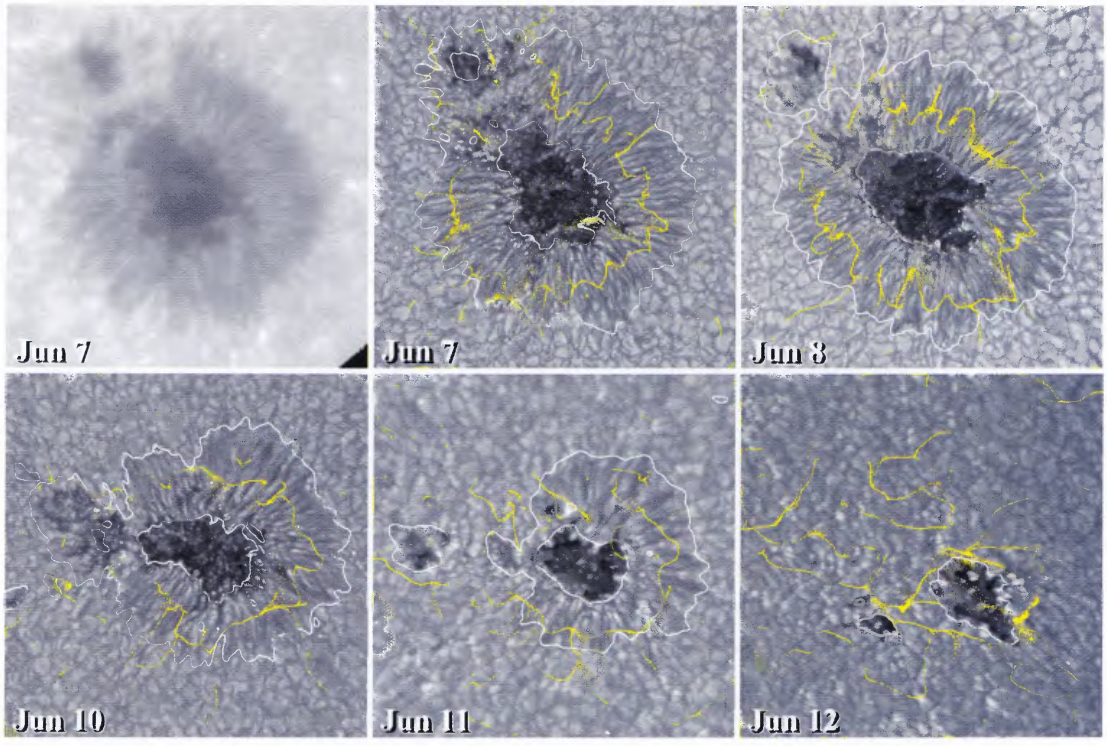

Figure 3.4 Evolution of the sunspot over six days during its decaying phase. Geometrical foreshortening has been corrected in the speckle reconstructed white-light images. The white contours outline the umbral and penumbral boundaries. The yellow corks trace the dividing lines of the inward and outward flows in the penumbra. The first panel is a Fe I 6301.5 Å line core image derived from two-dimensional spectroscopy where brightenings in the vicinity of the sunspot are associated with small-scale magnetic fields and moving magnetic features.

3.5 Results

3.5.1 Photometry of the Decaying Sunspot

The sunspot has a quasi round shape with a small trailing satellite component. The umbra is elongated in the direction of the small umbral satellite component. Numerous umbral dots can clearly be seen from day to day in Figure 3.4. The penumbral area grew from June 7 to 8. Starting on June 8, the spot decayed fast. The satellite component became larger at first and then separated from the main spot. On June 12, near the west limb, the penumbra completely disappeared and the

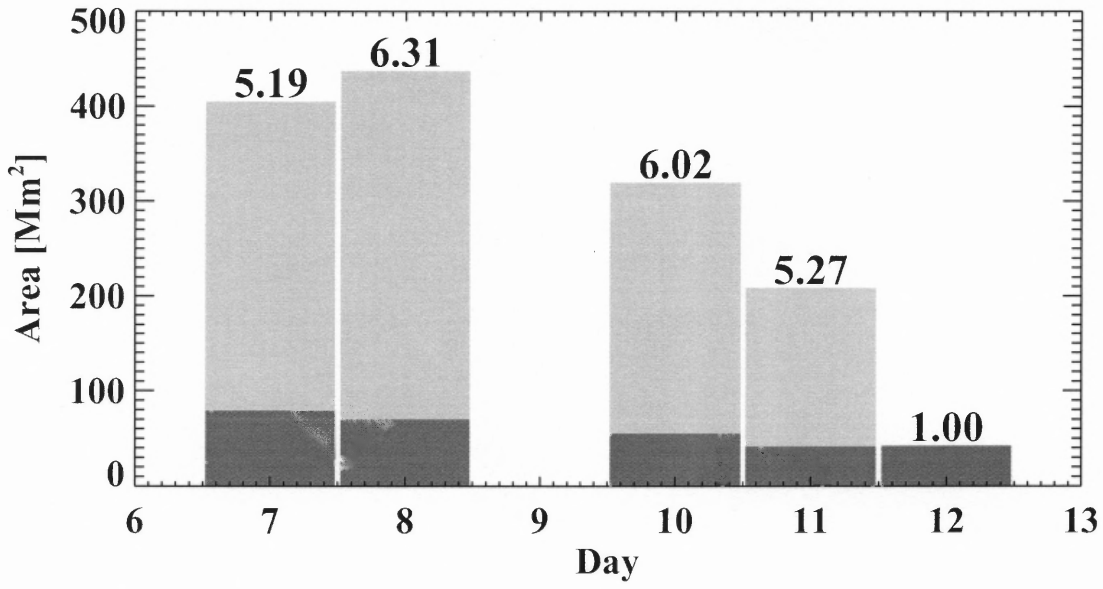

Figure 3.5 Evolution of the sunspot area. The gray bars represent the penumbra, dark bars correspond to the umbra, and their sum relates to the total area of the sunspot.

spot and its satellite component became a pair of pores. In addition, the sunspot rotated counterclockwise by about 45° during the five days from June 7 to 11.

Figure 3.5 shows the evolution of the penumbral, umbral and total area of the sunspot. The total-to-umbral area ratio ($r_A = A_{\mathrm{TOT}}/A_U$) for each day was calculated and annotated accordingly on the top of each bar in Figure 3.5. The geometrical foreshortening was corrected for these area calculations. The published results of r_A range from 4.0 to 6.3 but are mostly distributed between 5.0 and 6.0 (see Solanki 2003, for a summary). The result from this study shows that r_A ranges from 5.19 to 6.31, which is in agreement with previous measurements. The penumbral area apparently changes more than the umbral area, i.e., the monotonic drop of r_A from 6.31 to 5.27 from June 8 to 11 indicates that the sunspot penumbra decays faster than the umbra.

3.5.2 CLV of Umbral and Penumbral Brightness

Figures 3.6 and 3.7 show the CLV of the relative brightness (I/I_{QS}) of areas corresponding to penumbra (P), penumbral grains (PG), penumbral filaments (PF), umbra (U), umbral dots (UD) and umbral core (UC). The intensity ratios were calculated from 30-minute averages of speckle reconstructed white-light images and line core images, respectively. At first sight, there are distinct and large monotonic increases with heliocentric angle in the relative umbral brightness for all parameters U, UD and UC. The increases are smaller and less distinct in the relative penumbral brightness for all parameters P, PG and PF. In the observed heliocentric range, I_U/I_{QS} increases by 43% towards the limb for both white-light and line core images. I_{UC}/I_{QS} increases by 47% and 67% for white-light and line core images, respectively. I_{UD}/I_{QS} increases by 21% and 18%, respectively. In other words, the brightness contrasts of the overall umbral area, umbral core and umbral dots decrease from center to limb for both white-light and line core images.

Figure 3.6 shows that penumbral grains are always the brightest features of the sunspot in white-light images. Umbral dots are always darker than penumbral grains but brighter than the overall penumbra when approaching the limb. Penumbral filaments are always brighter than the overall umbra.

Figure 3.7 contains information from higher photospheric layers. It shows that penumbral grains are no longer the indisputably brightest features in the sunspot, since umbral dots are brighter than or at least as bright as penumbral grains when approaching the limb. Umbral dots are always brighter than the overall penumbra. Penumbral filaments are still always brighter than the overall umbra. In summary, both umbral and penumbral features tend to appear relatively brighter from the lower to the upper photosphere. While, the relative brightness of umbral features increases with height faster than that of penumbral features.

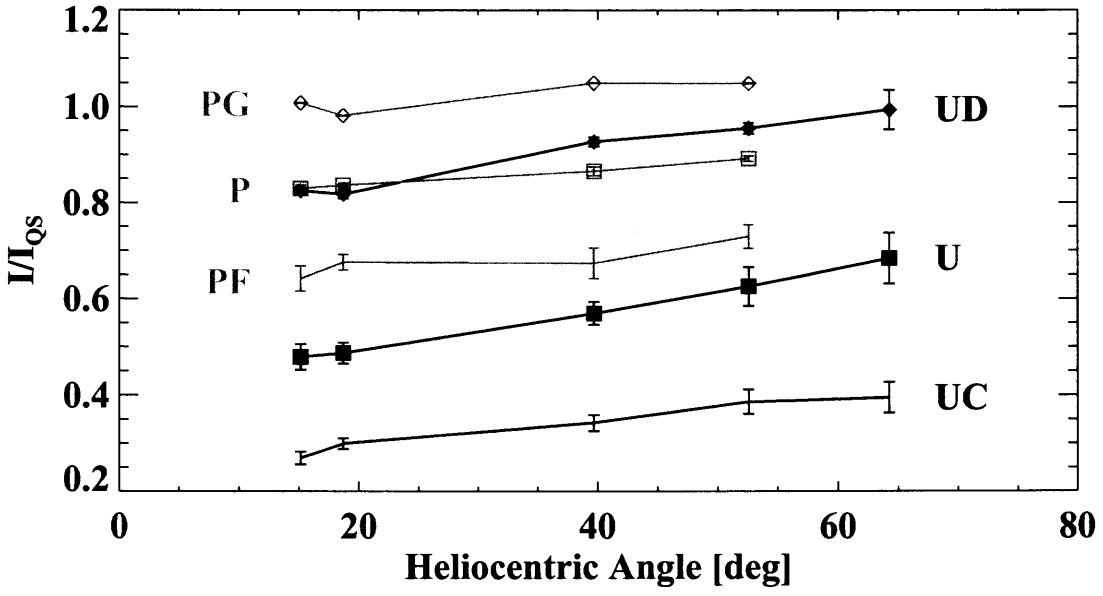

Figure 3.6 CLV of the intensity ratio between selected sunspot regions and quiet sun calculated from 30-minute averages of speckle reconstructions (P: penumbra, PG: penumbral grains, PF: penumbral filaments, U: umbra, UD: umbral dots, and UC: umbral cores).

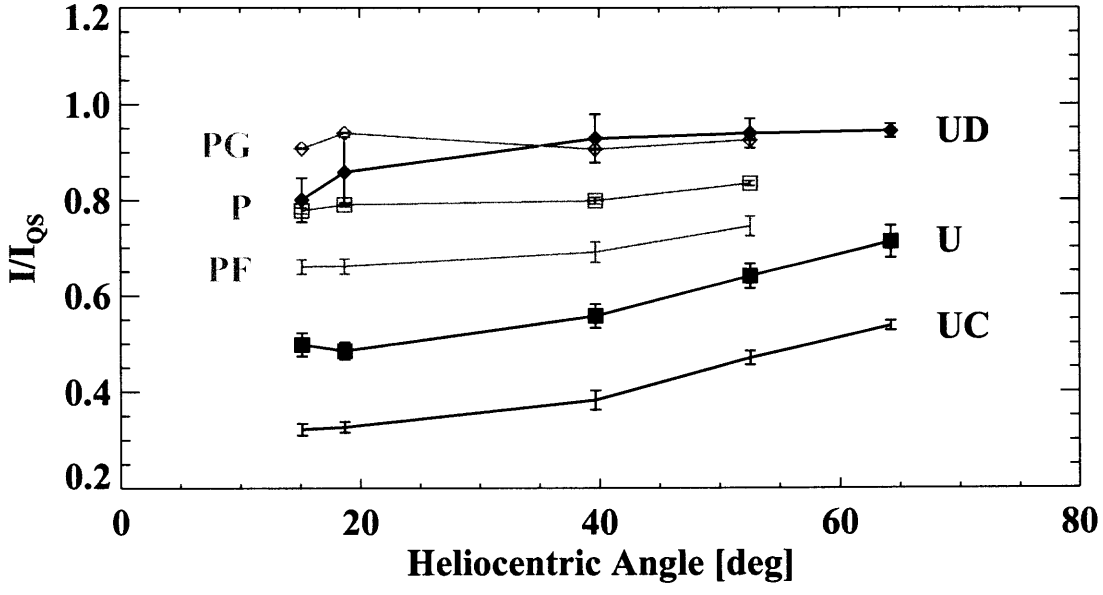

Figure 3.7 Same as Figure 3.6 but from 30-minute mean line core images.

3.5.3 Flow Field in the Decaying Sunspot

Figure 3.4 clearly shows the dividing lines, which separate the inward and outward LCT flows in the penumbrae. The dividing lines always reside in the middle of the penumbrae. They tend to be symmetric when the sunspot penumbra has a more symmetric configuration (see the June 8 panel in Figure 3.4). They lose symmetry when the sunspot penumbra becomes less symmetric (see the other panels in Figure 3.4). Interestingly, even after the penumbra completely disappears and the sunspot decays to a pore, there are still distinct dividing lines surrounding the remaining pore, although they are less symmetric and complete (see the June 12 panel in Figure 3.4).

In order to take full advantage of the high-resolution observation, the LCT flow fields (as shown in Figure 3.3) are decomposed into two components, i.e., magnitude $|v_{\rm LCT}|$ and azimuthal direction $\phi_{\rm LCT}$. They are displayed for each pixel in the left and middle columns of Figure 3.8. The flow's fine structure is more distinct in this type of display. The LOS velocities $v_{\rm LOS}$ for each day are also displayed in the right column of Figure 3.8. Blue colors represent blueshifts and red colors correspond to redshifts. Each row of Figure 3.8 shows the average result for a 30-minute data sequence on each day. The $\phi_{\rm LCT}$ component shows the radially inward motion in the inner sunspot (including the umbra and the inner part of penumbra) and radially outward motion in the outer sunspot. The outward motion extends to the neighboring photosphere for at least $5''$.

The $|v_{\rm LCT}|$ component shows that there are two ring-like structures of large $|v_{\rm LCT}|$. One is surrounding the penumbra-umbra border corresponding to the inward motion of penumbral grains, which has relatively small magnitude (with average speeds of about 0.4 km s^{-1} and a maximum speed reaching up to 0.8 km s^{-1}) and a width of about $3''$ or about 2200 km on the solar surface. The other is surrounding the penumbra-photosphere border corresponding to the outward motion of penumbral

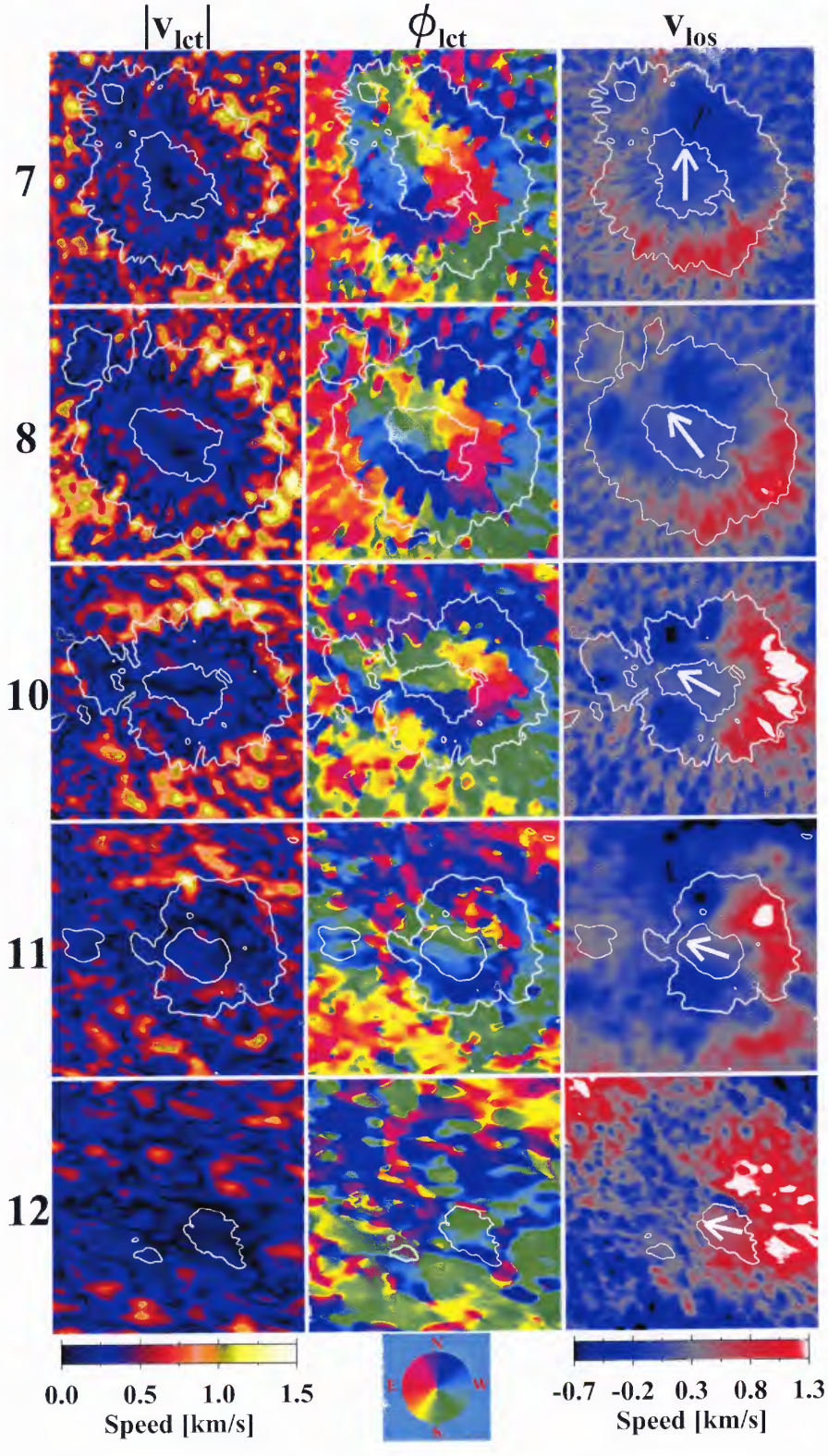

Figure 3.8 Decomposition of the three-dimensional flow field into speed (*left column*), direction as indicated by a color-coded disk at the bottom (*middle column*), and LOS speed (*right column*). The arrow in the umbra points towards the direction of disk center.

filaments, which has a distinctly larger magnitude (with an average speed of about 0.8 km s^{-1} and a maximum speed reaching up to 1.4 km s^{-1}) and a width of about 5″ or 3700 km. The outer ring of the large LCT speed, which was called "annulus", was also detected by November et al. (1986) in the horizontal flows around sunspots. Both of the two rings lose their symmetry when the sunspot decays and becomes less symmetric. One remarkable feature should be noticed, i.e., both inner and outer rings are skewed/shifted toward the limb-side for about 2″ or 1500 km. As can be seen in Figure 3.8, the rings at the center-side occur at the penumbra-photosphere or penumbra-umbra borders, while the rings at the limb-side occur outside corresponding borders.

The $v_{\rm LOS}$ component clearly shows the Evershed effect in the sunspot. It was accepted that the Evershed flow is most prominent in the outer penumbra, while the results from this study show that it is true only for the limb-side Evershed flow. At the center-side, the Evershed flow is most prominent in the middle of the penumbra. Therefore, the Evershed effect is also skewed toward the limb-side by about 2″ or 1500 km, i.e., the blueshifts are confined to the penumbral region, while the redshifts extend to the neighboring photosphere. The blueshifts and redshifts have velocities 0.30 ± 0.16 and 0.54 ± 0.22 km s^{-1}, respectively. The magnitude of redshifts is larger than that of blueshifts by about 0.24 km s^{-1}.

3.6 Conclusion and Discussion

A photometric and spectroscopic high-resolution study has been presented showing the decay of an isolated, quasi-round following sunspot covering six days in June 2006. Martínez Pillet (2002) critically reviewed several aspects related to the decay of leading and following sunspots and summarized the current state of knowledge of the physical mechanisms that are involved in sunspot evolution. In general, a long period of stability is rarely found in the following sunspots, since they decay very

fast, typically within several days or less after their formation. They usually possess irregular shapes and incomplete penumbrae. Only 3% of the observed following spots have the full round shape, so-called α configuration (Bray & Loughhead 1964). In contrast, it is very likely for a leading sunspot to develop a complete round and slowly decaying configuration that can last very long up to many weeks (e.g., Martínez Pillet 2002). The underlying physics of the different characteristics between the two poles of the active region is still not fully understood and the observations presented in this study provide a rare exception of the aforementioned rule.

The separation of the small trailing satellite component from the main body observed in this sunspot could be explained in terms of the fluting instability of the magnetic flux. Parker (1975) discussed the development of fluting instability in a concave boundary between magnetic flux and field free region, which can lead to the photometric fragmentation of the sunspot. However, Martínez Pillet (2002) has shown that the decay of following spots through a rapid process of the fluting instability is self-contradictory. It cannot satisfactorily reconcile the conflict between the fast decay rate and the overall inclination angle of the following polarity in the loop system of the active region. Another and more likely explanation of the photometric decay of sunspots is the diffusion model, in which the magnetic flux of the spot is spread out by an outward diffusive process over larger and larger areas with decreasing strength. Thus, some magnetic flux is transformed to small-scale magnetic features such as faculae, small pores, and magnetic knots (Martínez Pillet 2002).

An increase in relative brightness or equivalently a decrease in contrast of the sunspot was observed from center to limb. The rate of temperature increase with height in the sunspot is larger than in the quiet Sun. The relative umbral brightness increases faster with height than that of the penumbra. Although this result is in contrast to previous semi-empirical umbral models (e.g., Zwaan 1974, 1975; Kollatschny et al. 1980) that predict a decrease in umbral brightness toward

the limb, it is in agreement with the overall tendency of the sunspot temperature changing with height. Sunspots are only relatively cool in the photosphere. Starting from transition region and throughout the corona, they are much hotter than the surroundings. In addition, the stronger the magnetic field is, the hotter is the site. This tendency requires that the temperature gradient with height is larger in sites with stronger magnetic field. To understand how the energy is efficiently transported through the sunspot's magnetic flux is important for solving the coronal heating problem. Therefore, more studies are needed to establish a solid observational result and statistically quantify the height dependence of the sunspot temperature. Since observations in the infrared wavelength region (Albregtsen et al. 1984) show opposite behavior of the umbral contrast CLV, multi-wavelength studies are also necessary to complete the picture.

The skew of the blue- and redshifts of Evershed effect toward the limb-side observed in this study, i.e., the red-shift occurs farther from the umbra than the blue-shift, supports the opinion that the Evershed flow follows a convex path (see e.g., Solanki 2003). If the flow indeed curves downward near the outer penumbral edge, one would expect that the overall magnitude of the redshift is larger than the blueshift, which is confirmed by this study. Consequently, the convex flow structure implies that there exist returning flux or downflows at the outer footpoints near the sunspot/quiet Sun boundary. In fact, Westendorp Plaza et al. (1997) have shown evidence for such returning fluxes observed in dark penumbral filaments, which are believed to be the main agent for Evershed flows. They turn back down into the subphotosphere at certain locations of the outer penumbral boundary carrying almost all the mass inside.

Inward motions in the inner penumbra and outward motions in the outer penumbra were observed, which are separated by the distinct dividing line located in the middle of the penumbra. Schlichenmaier et al. (1998a,b) presented a magnetic

flux tube model, which can synthetically explain the penumbral fine structures such as penumbral filaments and grains, the Evershed effect and the observed inward motion of penumbral grains. The hot gas originating at subphotospheric levels pumps upward and flows horizontally outward along a thin magnetic flux tube, i.e., a penumbral fibril. The bright penumbral grains are the manifestation of the hot inner footpoints of these flux tubes. The appearance of their inward motions toward the center of the sunspot stems from a continuous rise of the magnetopause, i.e., the boundary between field and field free regions, toward the magnetic canopy. The observed inward motion in the inner penumbra and outward motion in the outer penumbra is in accordance with this penumbra model.

The observed similarity of motions between sunspot penumbrae and the pore's neighboring granulation, i.e., inward motion in the core of magnetic flux and outward motion in its outer surroundings, supports the idea of giant convection rolls in deep layers beneath the concentrated magnetic flux (sunspot or pore), i.e., converging and downward rolls beneath the inner part, next to diverging and upward rolls under the outer part (outer penumbra and neighboring photosphere) around the sunspot (see Figure 12 in Bovelet & Wiehr 2003, as an example). Using tomographic methods, Duvall et al. (1996) and Kosovichev (1996) have discovered large-scale downflows under sunspots, which were previously predicted by Parker (1992). These giant subphotospheric convective vortex rolls were later reproduced in MHD numerical simulations by Hurlburt & Rucklidge (2000). Recent discoveries in helioseismology (Gizon et al. 2000; Zhao et al. 2001; Kosovichev 2002) not only reinforce the existence of the large-scale convective cells beneath sunspots, but also quantitatively reveal a complex flow structure in these cells. Their studies show that the inflows feeding the downflows at depths of 1.5 Mm to 3.0 Mm turn into outflows at depths of 5.0 Mm to 9.0 Mm, which form a collar patten under the sunspot.

Both the magnetic flux tube and the subsurface giant convective roll models, which are supported by this study, favor the "cluster or spaghetti model" (Parker 1979; Choudhuri 1986) of sunspots over a "single monolithic flux tube" sunspot model (Cowling 1957; Knobloch & Weiss 1984). In the former one, the sunspot consists of many individual thin magnetic flux tubes at subphotospheric levels. A converging and downward mass flow right beneath the sunspot is necessary to confine and stabilize the flux cluster (Parker 1979; Choudhuri 1986). The monolithic model assumes that sunspot is a large uniform magnetic flux tube down to the convection zone. It has successfully explained the energy transport around the sunspot. However it cannot explain many other aspects of the sunspot, such as the fine structures in the sunspot, and the inward motion in the core of the magnetic flux tube and outward motion in its surrounding.

CHAPTER 4

RAPID PENUMBRAL DECAY ASSOCIATED WITH FLARES

The gradual decay of a simple quasi-round sunspot without any flare occurrence was presented in the previous chapter. Recently, rapid penumbral decay has been related to flares in complex sunspots Wang et al. (2004a). This new phenomenon is in contrast to the aforementioned gradual sunspot decay and challenges the long-standing opinion that solar flares have no lasting signatures in the photosphere and subphotosphere. A new flare model presented by Liu et al. (2005) has successfully explained this phenomenon. A statistical study of flare-associated, rapid structural change of sunspots has been presented by Chen et al. (2007). In this chapter, rapid penumbral decay associated with a special case (flare accompanied by filament eruption and CME) is presented and explained using the "magnetic breakout" model (Antiochos 1998; Antiochos, Devore, & Klimchuk 1999). This work was previously published in Deng et al. (2005).

4.1 Abstract

Observations of rapid penumbral decay associated with major flare activity is presented in solar active region NOAA 9026 on 2000 June 6. Within 1.5 hours, an X2.3 flare accompanied by an 11-degree long filament eruption and a full-halo CME originated near the neutral line of a large δ-spot region, which was associated with significant changes in white-light structure and magnetic field topology: an increase of moving magnetic features, flux emergence and cancellation, and in particular the rapid disappearance of two penumbral segments located in opposite polarity regions on the north and south side of the δ-spot. The rapid penumbral decay is believed to be the result of magnetic field topology change that was caused by rapid magnetic

reconnection during the flare rather than part of the overall long-term evolution. A possible explanation is presented for this event using the magnetic breakout model (Antiochos 1998; Antiochos, Devore, & Klimchuk 1999) for solar flares considering its complex multipolar δ-configuration and associated filament eruption and CME, i.e., previously closed magnetic field lines opened up and reconnected at a null point above the neutral line of this δ-spot. The magnetic breakout caused an energy release from a highly sheared magnetic field in the umbrae and a transition of the magnetic arcades from low-lying to high-arching, which led to an increase of the inclination angle of the magnetic field lines in the peripheral penumbrae, i.e., the magnetic field turned from more inclined to more vertical and turned toward the inner umbrae. Once the magnetic field in the penumbrae was vertical enough, the Evershed flow ceased, the manifestation of which in white-light structure is the disappearance of peripheral penumbrae. Other possible flare models are also discussed for this event. They are compared with respect to several observational features. The present observations provide further evidence that highly energetic events have a distinct associated photospheric magnetic field signature and support the findings of recent analysis of photospheric LOS magnetograms from BBSO and MDI that show rapid and permanent changes of photospheric magnetic fields associated with flares.

4.2 Introduction

Flare-related photospheric magnetic field changes have been sought for many decades. They may provide clues as to how an active region stores and releases flare energy. However, the evolution of photospheric magnetic fields associated with flares is still not well understood and the results have not been conclusive. For example, Severny (1964), Zvereva & Severny (1970), Moore et al. (1984), and Kosovichev & Zharkova (1999, 2001) reported that the magnetic field strength or flux decreases after solar flares. Some other authors debated that the changes are not related to flares but

embedded in a general trend in the overall evolution of the magnetic field of active regions (see Sakurai & Hiei 1996, for a review). After studying over 20 M-class flares, Chen et al. (1994) claimed that there is no distinct change in magnetic field before and after the flares. Ambastha, Hagyard, & West (1993) and Hagyard, Start, & Venkatakrishnan (1999) showed inconclusive results, i.e., the morphology of the photospheric magnetic field of an active region may or may not change as the result of a solar flare. Several recent studies based on newly developed high-spatial and high-temporal resolution ground- and space-based observations provide new exciting results related to this topic. Spirock et al. (2002) detected an increase in the magnetic flux of the leading polarity and an inapparent change in the following polarity after an X20 flare. Wang et al. (2002b) studied six X-class flares and concluded that rapid, permanent, and perhaps unbalanced flux increase might be a common property of major solar flares. Wang et al. (2004b) and Yurchyshyn et al. (2004) provided evidence for the emergence of unbalanced magnetic flux associated with flares. Other than looking for flare-related large-scale magnetic flux changes in active regions, in the last five years, attention has been paid to the correlation between major flares and local small-scale changes of white-light structure in complex sunspots (Wang et al. 2002a, 2004a; Liu et al. 2005). In order to thoroughly understand the correlation of magnetic flux change with energetic solar flares, more precise observations are needed and a conclusive model needs to be established. However, accurate measurements of sunspot magnetic fields can only be achieved by high-resolution two-dimensional spectro-polarimetry instead of the currently used filter-based magnetograph systems, which are not well suited for measurements of strong magnetic fields in the sunspot umbrae because of Zeeman saturation.

Antiochos (1998) and Antiochos, Devore, & Klimchuk (1999) proposed one possible mechanism named magnetic breakout model that can interpret CMEs, eruptive flares, and magnetic field changes during the eruptions. The multipolarity

of the photospheric magnetic field of the active region plays a crucial role in this model. In multipolar topologies, the eruption is triggered by magnetic reconnection at the high null point between a sheared arcade and the neighboring flux systems, i.e., reconnection takes away the high-arching potential field above the low-lying, highly non-potential core flux near the neutral line, so that the originally closed core flux opens violently and releases its energy eruptively. Aulanier et al. (2000) studied an M-class flare that was accompanied by a CME and occurred in a δ-sunspot region. They found evidence supporting the magnetic breakout process as the trigger of the eruptive flare.

Even though the aforementioned studies and the present analysis focus on highly energetic events, smaller events in the lower M- and C-class range may show a similar signature when observed with sufficient spatial and temporal resolution. For example, Denker & Wang (1998) presented speckle-reconstructed, diffraction-limited observations of a small δ-spot, where strong proper motion of magnetic features led to a C-class flare with properties similar to major flares (Wang et al. 1991).

4.3 Observations

On 2000 June 6, the GOES satellite recorded an X2.3 flare in a δ-sunspot located at N20E18 in solar active region NOAA 9026, which started at 14:58 UT, peaked at around 15:25 UT and decayed slowly afterward. The X2.3 flare was accompanied by an 11-degree long filament eruption and a full-halo CME.

The evolution of the δ-sunspot structure was studied and observations showed that two penumbral segments at the periphery of the spot decayed rapidly and permanently within 1.5 hours, which was associated with the X2.3 flare. These observations are quite apparent in a movie of white-light images obtained in broadband white-light roughly centered at 5000 Å from TRACE.

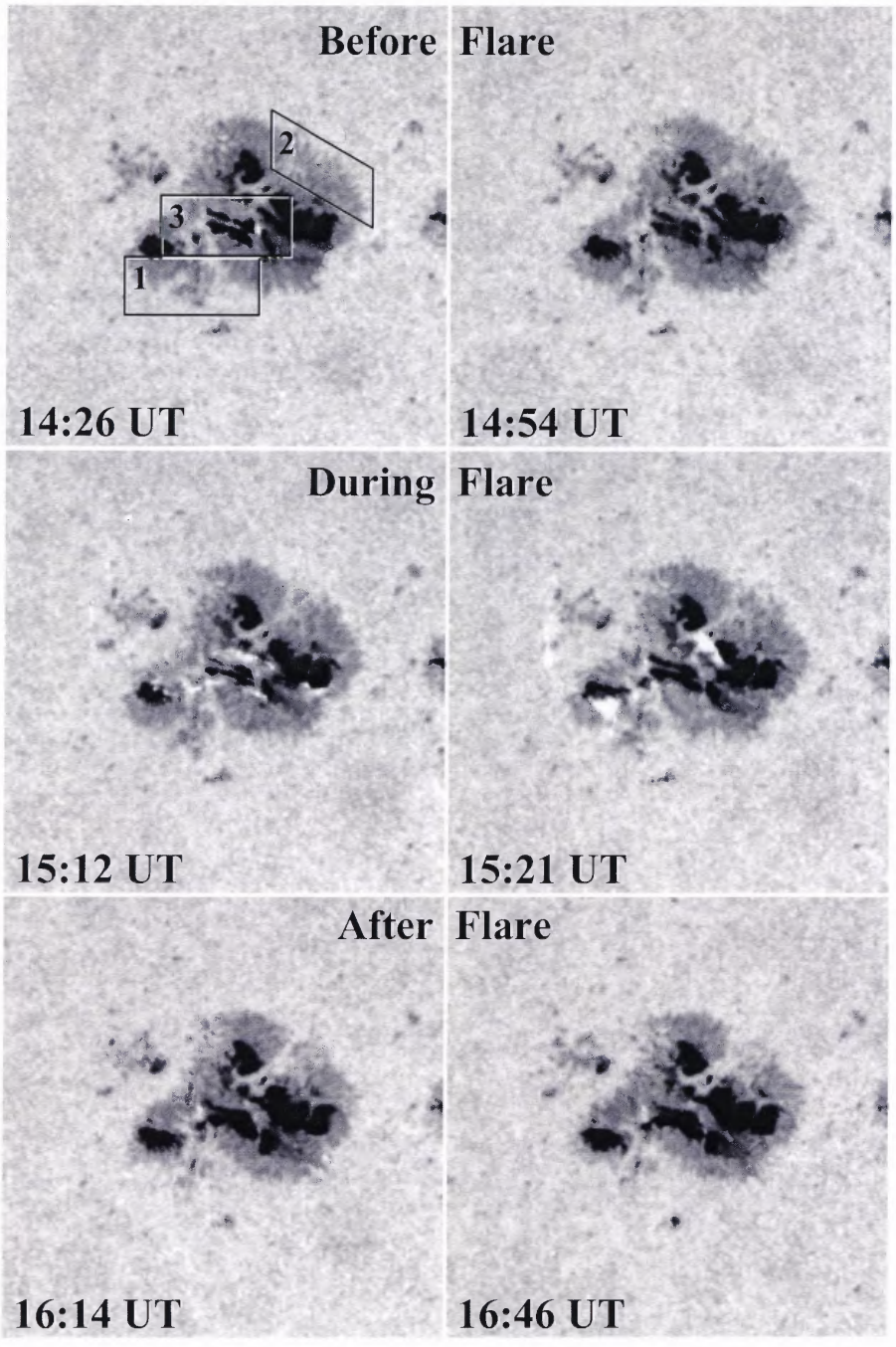

Figure 4.1 Time sequence of TRACE white-light images at 5000 Å obtained on 2000 June 6 showing the evolution of active region NOAA 9026. Area 1 (A1) and area 2 (A2) outlined by boxes 1 and 2, respectively, refer to the two disappearing penumbrae. Area 3 (A3) outlined by box 3 includes the darkening central umbra. The FOV is $150'' \times 150''$.

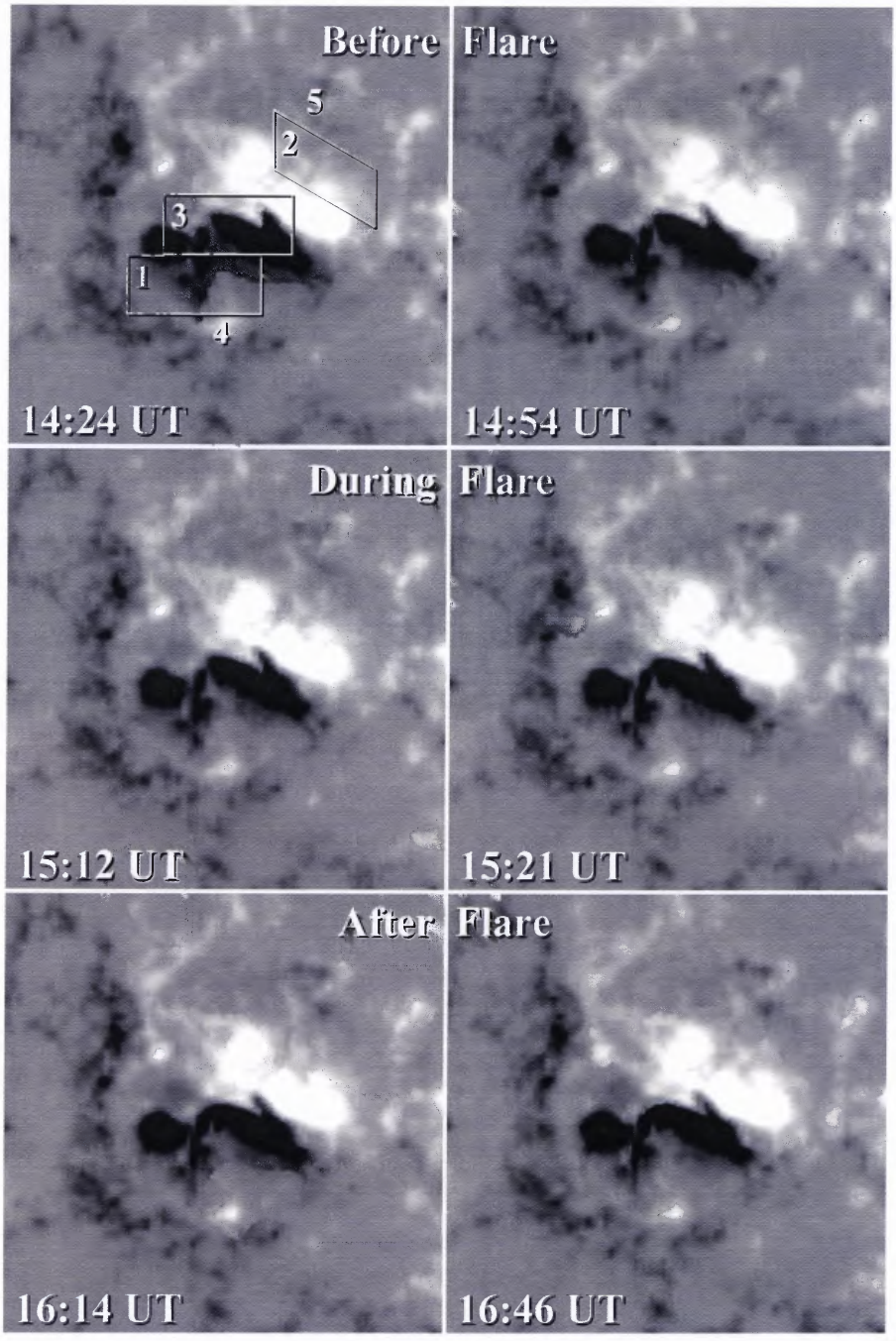

Figure 4.2 Time sequence of MDI LOS magnetograms corresponding to Figure 4.1. A1, A2, and A3 are the same regions as shown in Figure 4.1. The labels 4 and 5 denote the localized emerging/strengthening opposite polarity regions around the δ-sunspot.

The typical cadence is less than a minute and the spatial resolution is about 1″, which make these data ideally suited for high-resolution studies of active regions (Handy et al. 1999). Unfortunately, there were only four white-light images during the time period from 14:54 UT to 16:14 UT on 2000 June 6 that covered the flare period, which can only give an association of the penumbral decay with the flare within 1.5 hours.

Then, the LOS magnetograms from MDI were examined to investigate the photospheric magnetic field evolution. The magnetic flux in the decaying penumbral regions experienced a rapid and permanent change associated with the X2.3 flare. MDI provides full-disk longitudinal magnetograms with a cadence of one minute and spatial resolution of about 4″. The magnetograms are obtained by scanning five wavelength settings covering the Ni I 6768 Å line. A detailed description of MDI observation and data reduction is given in Scherrer et al. (1995).

High-resolution Hα full-disk images obtained at BBSO (Denker et al. 1998) are used to study the filament eruption associated with the flare. The Hα images have 2032×2032 pixels, the cadence is one image every minute, and the spatial resolution is about 2″. The Hα raw data were corrected by subtracting a dark frame and applying a flat-field frame. In addition, a limb darkening function was subtracted to enhance the image contrast.

4.4 Results

Studying dynamic phenomena on small scales has the potential to shed more light onto global phenomena that are frequently encountered in the context of space weather, e.g., flares, filament eruptions, and CMEs. In the present study, all three phenomena occur associated with rapid and permanent changes of white-light structure and photospheric magnetic fields in a δ-sunspot.

In Figures 4.1 and 4.2, the evolution of NOAA 9026 is illustrated from about 14:24 UT to 16:46 UT in TRACE white-light images and MDI LOS magnetograms. The X2.3 flare peaked at around 15:25 UT within this time range. The penumbrae, in two regions outlined by boxes 1 and 2, partially disappeared within 1.5 hours as a consequence of the X2.3 flare. Meanwhile, the central umbral region outlined by box 3 strengthened and was related to the flare and the penumbral decay. This event also produced a Type II radio burst (1189 km/s), a Type IV radio burst, an 11-degree long filament eruption, and a full-halo CME. Figure 4.3 shows the location of the 11-degree long filament eruption in a detailed view of BBSO full-disk Hα images.

By examining movies of intensity maps and magnetograms, the most straightforward way to study the evolution of sunspot structure and magnetic fields, the δ-spot in NOAA 9026 was found to consist of four major and several minor umbral cores, which are separated by light-bridges and surrounded by complex penumbrae. The dominant magnetic neutral line is aligned with one of the light-bridges and splits the δ-spot into a northern hemisphere of positive polarity and a southern hemisphere of negative polarity. The whole δ-spot is surrounded by a ring of small sunspots and pores with an average distance from the δ-spot penumbrae of about $20''$ to $40''$. These small sunspots are associated with moving magnetic features, especially near the northern penumbra. During the flare the number of moving magnetic features near the northern part of the penumbra is increasing. Most noticeably three to four distinct negative polarity magnetic features denoted by "5" in Figure 4.2 appear and become stronger during the period from about 14:00 UT to 17:30 UT, even though there are indications that there is continuous cancelation with positive polarity features. All these negative polarity magnetic features show strong motions radially outward but become stationary once they reach the outer ring of small sunspots and pores. The flux emergence scenario in the southern hemisphere is quite different. Here, a large, isolated positive polarity magnetic feature denoted by "4" in Figure 4.2

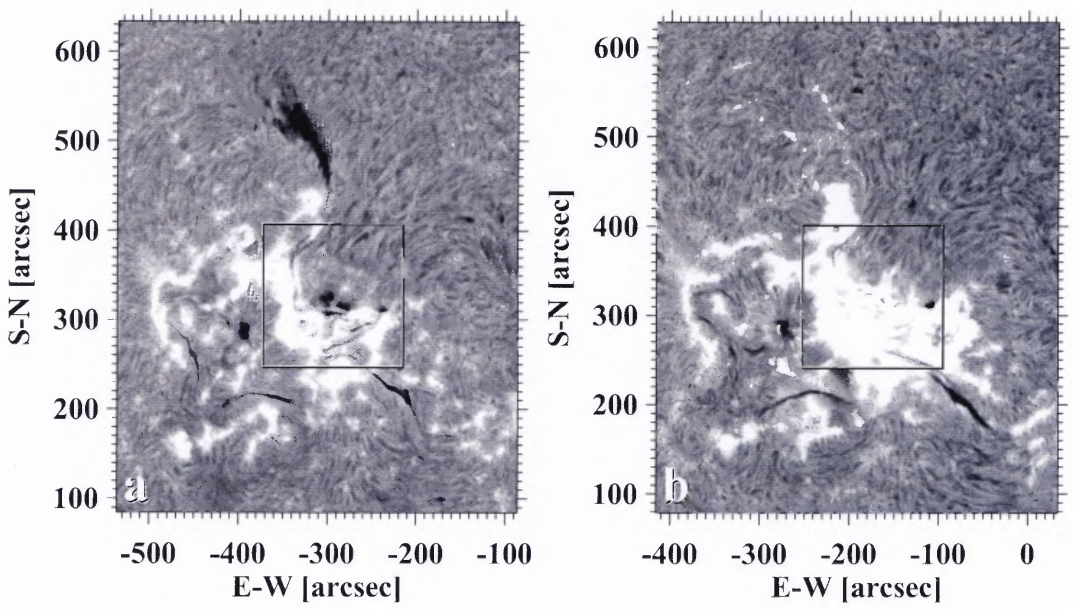

Figure 4.3 Detailed view of BBSO full disk Hα images (a) on 2000 June 5 at 23:28:46 UT before and (b) on 2000 June 6 at 16:14:21 UT after the flare showing the location of the 11-degree long filament eruption. The filament was essentially located above the neutral line of the δ-spot before the flare. The region indicated by the box is the same FOV as shown in Figures 4.1 and 4.2.

is strengthening while propagating toward the west. No evidence was found for flux cancelation in this region. In both cases, however, localized emergence and strengthening of opposite polarity flux is involved in the flare and the subsequent disappearance of the penumbrae.

The X2.3 event is a two ribbon flare originating at the neutral line of the δ-spot, where strong gradients of the magnetic field and strongly sheared horizontal magnetic fields tend to initiate flares (Wang et al. 1994). Even before the flare started, a sporadically appearing, well defined point-like brightening was observed moving along the neutral line at a velocity of about 0.5 km s^{-1} or less. This brightening is located within a light-bridge, i.e., the location where the southern umbral cores begin to fragment.

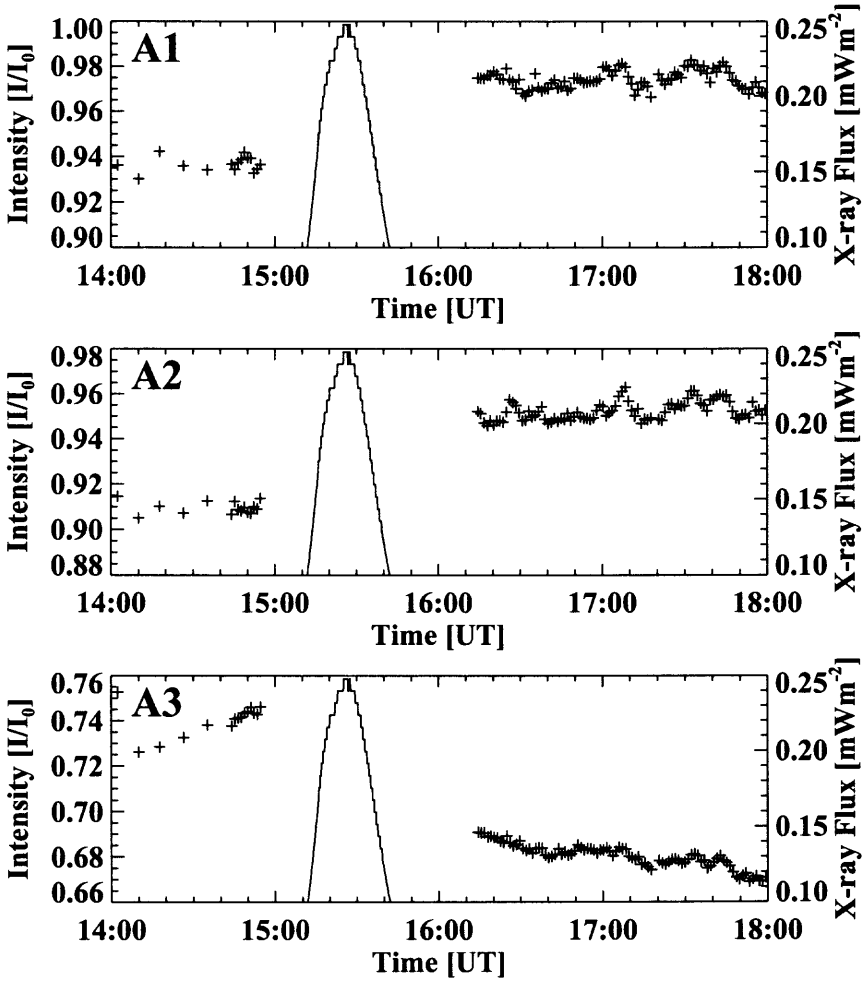

Figure 4.4 Temporal evolution of the average intensity from TRACE white-light images in areas A1, A2, and A3 (plus signs). The GOES X-ray flux in the 1 Å to 8 Å band is depicted in each panel with solid lines to illustrate the X2.3 flare. The data gap between 14:54 UT and 16:14 UT results from eliminating the data during the flare when bright flare ribbons traverse areas A1, A2, and A3.

The bright channel in the eastern part of the southern umbra is co-spatial with the initial flare line of the X2.3 flare. The two ribbons of the X2.3 flare separate at a speed of about 20 km s^{-1} with a maximum velocity of about 30 km s^{-1} at the initiation of the flare. Subsequently, the ribbons decelerate and the final velocity is about 15 km s^{-1} before the flare fades away in the TRACE white-light images.

In this chapter, the normalized intensity is defined as the average intensity of a certain region outlined by boxes 1, 2, and 3 in Figure 4.1 divided by the photospheric intensity outside the sunspot in a quiet sun region that is located at the upper-right corner of the FOV in Figure 4.1. An intensity of 1.0 means that the region is free of sunspots. A smaller intensity value represents a larger and/or darker sunspot in the area. In Figure 4.4, the intensities in areas A1 and A2 have a rapid, 4–5% increase within 1.5 hours associated with the X2.3 flare, which represents the rapid penumbral decay in these two regions, while the intensity in central umbral area A3 has a rapid, 8% decrease correlated with the flare and the penumbral decay. Four data points during the flare were excluded in order to avoid the influence of the bright flare ribbons that may provide false intensity information when they moved across the selected regions. No noticeable change was found in the average intensity in other small sunspots outside this δ-sunspot region before and after the flare. Therefore, the observed penumbral decay and umbral darkening are not related to image quality, but are really associated with the flare.

As shown in Figure 4.5, the magnetic flux decreases rapidly by 17% in A1 and is well correlated with the X2.3 flare. In A2, the magnetic flux decreases gradually instead of rapidly. Since A2 was associated with fast moving magnetic features, the large velocity of fast moving magnetic features may introduce some errors into the measurement of the LOS magnetic field. Therefore, it does not show distinct rapid flux decrease in A2 associated with the flare.

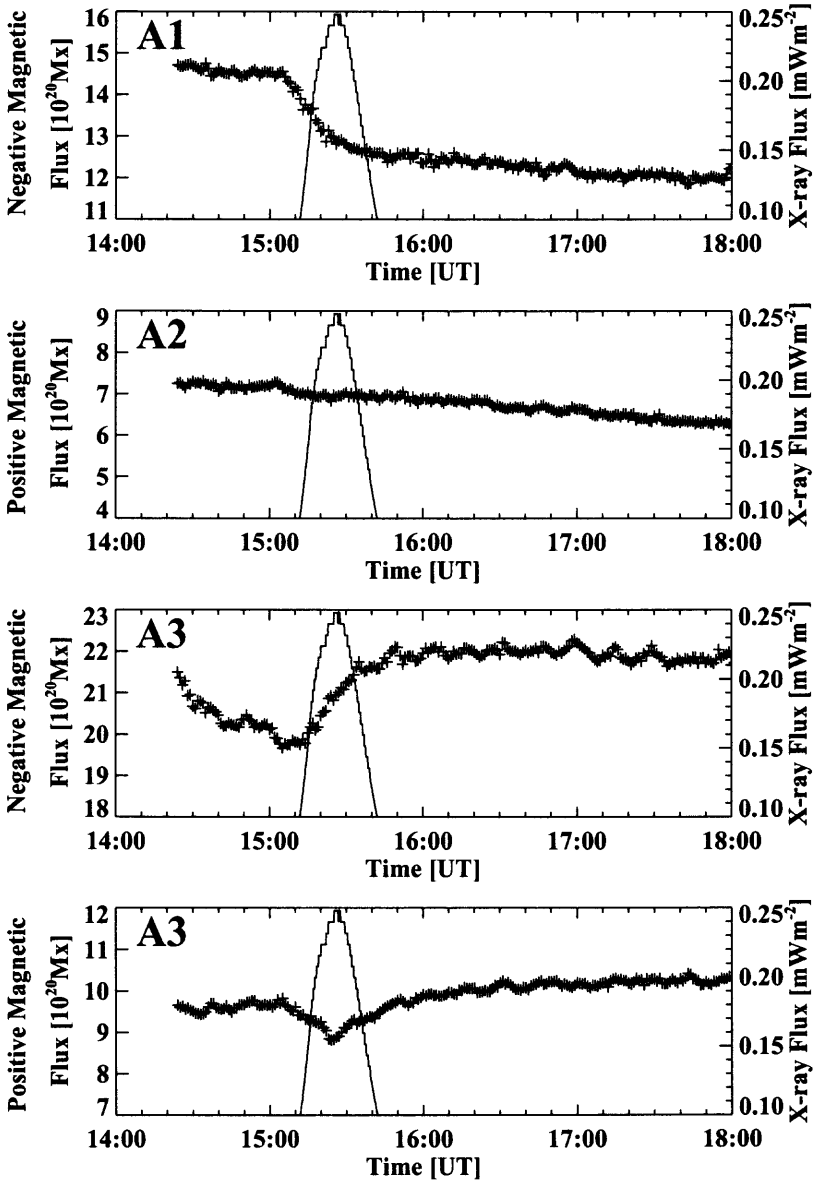

Figure 4.5 Temporal evolution of the average magnetic flux from MDI LOS magnetograms in areas A1, A2, and A3 (plus signs). The GOES X-ray flux in the 1 Å to 8 Å band is depicted in each panel with solid lines to illustrate the X2.3 flare.

Meanwhile, both the negative and positive magnetic fluxes in the central umbral area A3 increase by 4–7% after the flare. Note that the flare response of the Ni line used for the MDI observations causes temporary flux dips for about 30 minutes during the flare. However, the flare emission cannot cause a permanent change after the flare. Therefore, the flux change during the long time period shown in Figure 4.5 is not due to the transient flare emission but relates to a real photospheric magnetic field change associated with the flare.

4.5 Summary and Discussion

The rapid decay of two sunspot penumbrae and the strengthening of the central umbrae within 1.5 hours associated with an X2.3 flare have been presented in a δ-sunspot.

A natural question arises: Is the rapid penumbral decay a coincidental phenomenon involved in the general sunspot decay or closely related to the flare in particular? Kurokawa, Wang, & Ishii (2002) studied the same flare-productive active region NOAA 9026 for its long-term evolution and found that drastic changes in the δ-sunspot configuration started several hours before the big flares of 2000 June 6. In particular, they reported the catastrophic decay of the central umbrae from 10:00 UT of June 6 to 16:00 UT of June 7. They constructed a schematic model of an emerging twisted flux rope to explain the drastic evolution based on magnetic flux changes in the whole active region and evolution of the umbrae. However, they did not mention the penumbral decay and umbral darkening phenomenon. There was no penumbra represented in their cartoon. One should distinguish between the flare-related rapid changes (penumbral decay and central umbral darkening) in the present chapter and the long-term evolution (umbral decay) in Kurokawa, Wang, & Ishii (2002). The long-term change is the total flux change in the whole active region, which is involved in the overall evolution of the sunspot, while the flare-related change is a flux change

localized in small patches caused by short-term magnetic reconnection. However, it is a very challenging topic to combine flare-related impulsive change and long-term evolution of an active region to see what role solar flares play in the overall evolution of sunspots (Wang et al. 2005).

Two additional papers reported flare-related, short-term penumbral decay in more flare events that occurred in other active regions, which proves that this kind of phenomenon can not be coincidental. Wang et al. (2004a) clearly showed the penumbral decay and central umbral darkening associated with three X-class flares by using the white-light difference images. They provided the following interpretation: magnetic fields turned from more inclined to more vertical after flares, which caused the outside penumbrae to decay and the central umbrae to strengthen. However, the light curves and physical models are not included in that paper. Liu et al. (2005) carried out a preliminary statistical study of rapid changes of δ-spot structure associated with seven major flares. They proposed a reconnection picture in which the two components of a δ-spot become strongly connected after the flare.

The essential reason for penumbral decay and umbral darkening is that the magnetic field lines in peripheral penumbrae turned from more inclined to more vertical and turned toward the central umbrae, which was caused by magnetic reconnection during the flare. Once the inclination angle (the angle between magnetic field lines and the surface) is larger than 45°, the Evershed flow will cease, the continuum-intensity signature of which is the disappearance of the associated penumbrae (Leka & Skumanich 1998).

In this study, a proper flare model needs to be pursued to interpret the observed flare-related rapid changes in the multipolar photospheric magnetic configuration. The emerging twisted flux rope model presented in Kurokawa, Wang, & Ishii (2002) is well suited in explaining umbral change involved in long-term evolution but is weak in explaining the flare and flare-related penumbral change. The reconnection scenario

proposed by Liu et al. (2005) can successfully explain the flare-related penumbral decay, central umbral darkening, and associated CME. However, this model is weak in explaining the accompanied filament eruption. Besides these two models that could be used to explain this event, let us discuss the classical Kopp-Pneuman model (Kopp & Pneuman 1976), in which the overlying coronal fields are torn open by the dark filament and reconnection of field lines happens subsequently, which eventually restore the pre-flare magnetic configuration. This model has been successful in explaining two-ribbon flares, filament eruption, and the associated CME. However, it can hardly explain the change of the magnetic field configuration after the flare, as the photospheric magnetic structure is finally restored to the pre-flare configuration. Another well-known standard picture for flare/filament eruptions is the so-called "tether-cutting" model (Sturrock 1989; Moore & Roumeliotis 1992), which involves only a single sheared magnetic arcade in bipolar regions that have a single neutral line in the photosphere where the vertical field component changes sign. However, this model cannot explain CMEs very well, since there is no observational proof of non-anchored bubble-like CMEs predicted by this model and tether-cutting eruption has not been directly discovered in any of the simulations so far. Finally, much attention was paid to the newly-developed magnetic breakout model for CMEs and eruptive flares. This model not only can explain the flare event accompanied by filament eruption and CME, but also naturally includes the decay of penumbrae by changing the orientation of field lines from inclined to more vertical configuration. The resulting opened field lines also account for the central umbral darkening. The following critical observational factors for this event need to be considered for qualifying the proper models: (1) multipolar complex δ-configuration plays a crucial role, (2) can explain accompanied filament eruption, (3) can explain accompanied CME, (4) can make magnetic field turn from more inclined to more vertical after magnetic reconnection. The above five models are summarized in Table 4.1.

Table 4.1. Summary of Models and Matching of Observational Constraints.

Model	Multipolarity Plays Crucial Role	Explain Filament Eruption	Explain CME	Magnetic Topology Changes
1	Yes	No	No	Yes
2	Yes	No	Yes	Yes
3	No	Yes	Yes	No
4	No	Yes	No	Yes
5	Yes	Yes	Yes	Yes

Note. — Model 1: Kurokawa, Wang, & Ishii (2002). Model 2: Liu et al. (2005). Model 3: Kopp & Pneuman (1976). Model 4: Tether-Cutting model—Sturrock (1989); Moore & Roumeliotis (1992). Model 5: Magnetic Breakout model—Antiochos (1998); Antiochos, Devore, & Klimchuk (1999); Lynch et al. (2004).

In this section, the explanation of the flare-related change in photospheric magnetic field topology is discussed in detail in terms of the magnetic breakout model. In the multipolar topology of active region NOAA 9026, the overlying potential flux above the low-lying, sheared core flux is removed by fast magnetic reconnection between the sheared arcade and the neighboring flux systems near the neutral line of the δ-spot, which initiates the breakout of the whole system. The core flux opens explosively, which triggers the flare, the associated filament eruption, and the subsequent CME. The magnetic arcades turn from low-lying to high-arching after the flare due to magnetic reconnection, which causes magnetic fields in the photosphere to turn from more inclined to more vertical after the flare.

Panels (a) and (c) of Figure 4.6 show cartoons of the magnetic field state before the X2.3 flare. The magnetic polarity regions of the δ-spot have a symmetric structure with the symmetry axis along the central neutral line. Two main opposite polarity kernels (the δ-sunspot) are located close to the central neutral line. Two minority opposite polarity footpoints (A4 and A5) are located beside these kernels.

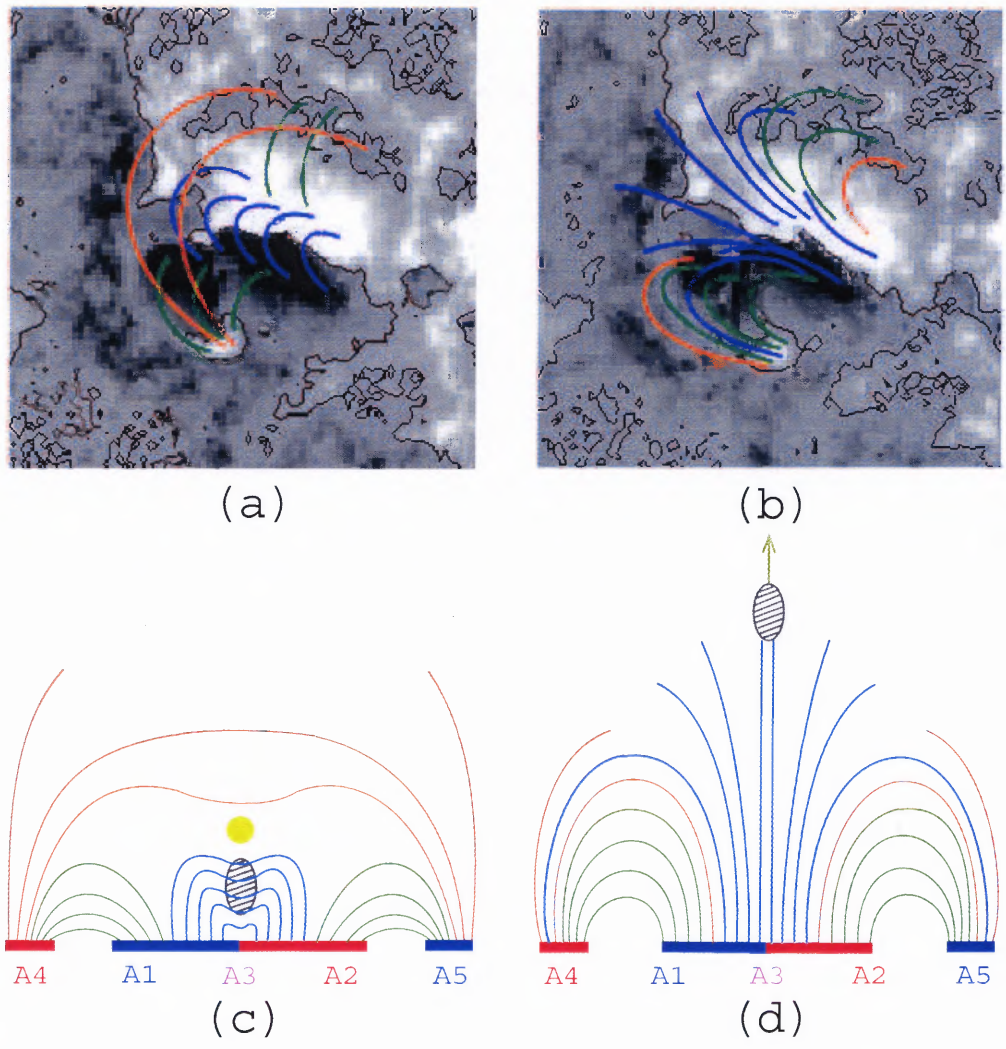

Figure 4.6 (a) MDI LOS magnetogram with neutral line before the X2.3 flare, the colored lines are a cartoon of the magnetic field topology before flare; (b) MDI LOS magnetogram with neutral line after the X2.3 flare, the colored lines are a cartoon of the magnetic field topology after flare; (c) two-dimensional scheme of magnetic field lines before the X2.3 flare; (d) two-dimensional scheme of magnetic field lines after the X2.3 flare. The magnetic topology is based on the magnetic breakout model.

For simplicity, the effect of peripheral magnetic features has been neglected. Therefore, there are three photospheric neutral lines and four distinct flux systems: a central arcade that connects the two kernels straddling the middle neutral line (blue field lines), two arcades associated with the bilateral neutral lines connecting each kernel with its opposite polarity footpoint (green field lines), and a flux system that connects the bilateral footpoints (A4 and A5) overlying the three arcades (orange field lines). Note that there are two separatrix surfaces that define the boundaries between the various flux systems and a null point (yellow dot) above the middle neutral line at the intersection of the separatrices. The bilateral (green) arcades are low-lying due to the confinement of the overlying (orange) arcade which has a tendency to hold down all the arcades below it. Therefore, magnetic field lines are very inclined in regions A1 and A2, which form the peripheral penumbrae.

As a result of large shear concentrated at the middle neutral line, which may be due to photospheric flows or emergence of new flux, rapid opening and reconnection of/between the central (blue) and the outermost overlying (orange) field lines occur at the null point when the flux systems reach their crucial condition. The breakout of the innermost flux of the central arcade causes the X2.3 flare, 11-degree long filament eruption, and full-halo CME. Figure 4.6 panels (b) and (d) show the magnetic field state after the X2.3 flare. Due to the opening and reconnection of the low-lying and overlying arcades, some flux is transferred from central (blue) and overlying (orange) systems to the bilateral (green) arcades, and the overlying (orange) arcade that tends to hold down all the other arcades is removed. Due to the removal of the confinement, the bilateral (green) arcades become high-arching, which causes the magnetic field lines in the peripheral penumbrae (A1 and A2) turn to be more vertical and turn toward the central umbrae (A3) after the flare. Once the inclination angle is larger than 45°, the Evershed flow in the penumbra will cease, the manifestation of which in continuum intensity is the disappearance or decay of the penumbra in

A1 and A2. Moreover, the magnetic flux in the peripheral penumbrae will decrease when many of magnetic field lines move out of their regions due to the increase of the inclination angle. On the other hand, the magnetic flux in the central umbrae will increase, since many field lines move from peripheral penumbral regions into their region. However, Figure 4.5 only shows a small flux increase in A3 instead of the expected large increase. This may be due to Zeeman saturation of filter-based magnetograph in strong umbral fields. But Figure 4.4 shows clearly that the central umbrae become darker in continuum-intensity due to the strengthening of their magnetic field.

CHAPTER 5

FLOW FIELDS IN FLARING SUPER ACTIVE REGION

The interaction of magnetic fields and plasma flows is one of the fundamental astrophysical processes that leads to many of the dynamic effects observed on the Sun. Flux concentrations are constantly moved around by convective flows. As a consequence, field lines get twisted and tangled, which leads to energy build-up in magnetic structures. This excess energy can eventually be released in flares. This chapter presents strong shear flows observed in complex sunspot penumbrae along magnetic inversion lines associated with a major flare. This work was published in Deng et al. (2006).

5.1 Abstract

This chapter presents high-resolution observations of horizontal flow fields measured by LCT from intensity images in three wavelengths, i.e., G-Band (GB), white-light, and Near InfraRed (NIR). The observations were obtained on 2003 October 29 within the flaring super active region NOAA 10486, which was the source of several X-class flares, including an X10 flare that occurred near the end of the observing run. The data were obtained at NSO/SP using the newly developed high-order AO system. Dopplergrams and magnetograms from MDI on board SOHO are also used to study the LOS flow and magnetic field. Persistent and long-lived (at least 5 hours) strong horizontal and vertical shear flows (both in the order of 1 km s^{-1}) were observed along the magnetic Neutral Line (NL) until the X10 flare occurred. From the lower photospheric level (NIR), the direction of the flows did not change up to the upper photosphere (GB), while the flow speeds in the shear motion regions decreased, and contrarily those in regions without shear motions increased, with increasing altitude.

Right after the X10 flare, the magnetic gradient decreased, while both horizontal and vertical shear flows dramatically enhanced, near the flaring neutral line. The results of this study suggest that photospheric shear flows and local magnetic shear near the neutral line can increase after the flare, which may be the result of shear release in the overlying large-scale magnetic system or the reflection of a twisted or sheared flux emergence carrying enough energy from the subphotosphere.

5.2 Introduction

A solar flare can suddenly release magnetic free energy, which was previously stored in the form of a stressed magnetic field topology. How is magnetic stress (shear or twist) formed, accumulated, and eventually released? This is an important but still unsolved question in solar physics. Strong flares tend to occur in the vicinity of magnetic neutral lines where the field gradients are strong and the horizontal components are highly sheared (e.g., Severny 1958; Wang et al. 1994, 2002b). Martres & Soru-Escaut (1977) found that flares are often associated with the neutral lines of the LOS velocities. Martres et al. (1974) proposed that the velocity field may be preponderant in triggering flares. Harvey & Harvey (1976) also stated that the velocity field pattern is at least as significant as the magnetic field in the flare build-up process. More and more observational evidence shows that strong shear flows in active regions are highly related to flare occurrences. Harvey & Harvey (1976) found a good association between flares and strong, oppositely moving velocity features in photospheric Dopplergrams. They also showed evidence that photospheric horizontal motions can twist and shear the magnetic field, thereby contribute to the flare production. Krall et al. (1982) studied photospheric velocity shear together with vector magnetograms and found that photospheric motions caused an increase in the magnetic shear prior to a flare. Keil et al. (1994) found evidence that the locations of flare kernels correspond to locations showing shear in the vertical and convergence

in the horizontal photospheric flows. Based on Doppler velocity maps, Meunier & Kosovichev (2003) observed long-lived fast supersonic photospheric LOS flows and possible shear flows close to the region where a flare occurred. Using AO-corrected and speckle-masking reconstructed high-resolution white-light images (Denker et al. 2004a), Yang et al. (2004) observed strong horizontal shear flows along the magnetic neutral line in the flare-productive active region NOAA 10486 several hours before a major flare. However, the evolution of flow fields around the occurrence of the flare was not included in Yang et al. (2004). So far the role of the strong photospheric flows and their interaction with the magnetic field during the evolution of an active region and their relation to solar flares are still not well understood. On the other hand, shear motion is one ingredient of flare processes that has received much attention in recent flare models (e.g., Sturrock 1989; Antiochos 1998; Antiochos, Devore, & Klimchuk 1999; Amari et al. 2000). There is evidence that the movement of magnetic footpoints by photospheric flows can lead to the destabilization of the magnetic field and hence to flares by increasing the length of the field lines in the corona (e.g., Somov et al. 2002). Some results related to the change of magnetic shear due to flares have been reported, e.g., the photospheric magnetic shear may increase after the occurrence of a major flare (Wang et al. 1994, 2002b; Liu et al. 2005), whereas investigations of the change of mass flow associated with flares are rare. Meunier & Kosovichev (2003) mentioned that the variations of the magnetic and velocity fields associated with flares occurred mostly in flare ribbon regions.

The height dependence of active region flows is also an important topic in investigating magneto-convection and providing three dimensional maps of active region dynamics. These maps are useful for developing three dimensional magnetohydrodynamic models describing the evolution of active regions. Helioseismology provides powerful diagnostics of subphotospheric convection, large-scale flows, and dynamics of active regions and sunspots (e.g., Kosovichev et al. 2002; Zhao &

Kosovichev 2003). In particular, new methods of local helioseismology, such as time-distance helioseismology, provide detailed maps of subsurface flows in flaring active regions, which can be compared with photospheric magnetic fields and flare morphology (http://www.newton.cam.ac.uk/webseminars/pg+ws/2004/msiw01/0913/kosovichev/). Using ring analysis of local helioseismology, Haber et al. (2004) assessed the subsurface horizontal flows that surrounded and permeated active region NOAA 10486 from 2003 October 18 to November 15. They found large-scale shear flows that may contribute to conditions conducive to intense flaring activities. Using time-distance helioseismology, Kosovichev et al. (2004) detected stronger than usual horizontal shear flows with velocities of $1-1.5$ km s^{-1} at a depth of 4.5 Mm almost along the neutral line, where the magnetic energy was released during the X10 flare in active region NOAA 10486. However, whether flows change when there is intense flaring still lacks conclusive evidence from these previous studies. A possible reason could be that the temporal extent of a flare-induced change in the flows is relatively short, while the temporal resolution of local helioseismic analysis is rather long ($\geq$ 8 hours). The spatial resolution of flow maps derived from local helioseismology at this moment is also quite large ($\geq$ 5 Mm) and may not resolve the flows most affected by flares. On the other hand, flow maps with high-spatial (up to $0.07''$ $pixel^{-1}$) and high-temporal (1 min) resolution can be obtained by LCT techniques (November & Simon 1988) based on direct high-resolution and high-cadence optical observations.

Active region NOAA 10486 was the largest and most complex sunspot group of solar cycle 23. It produced several X-class flares, including an X10 long-duration flare on 2003 October 29. Using chromospheric vector magnetograms spanning the X10 flare observed with the Imaging Vector Magnetograph (IVM) at Mees Solar Observatory (MSO), Metcalf, Leka, & Mickey (2005) found an unusually large amount of free magnetic energy of $(5.7 \pm 1.9) \times 10^{33}$ ergs, which is consistent with the very

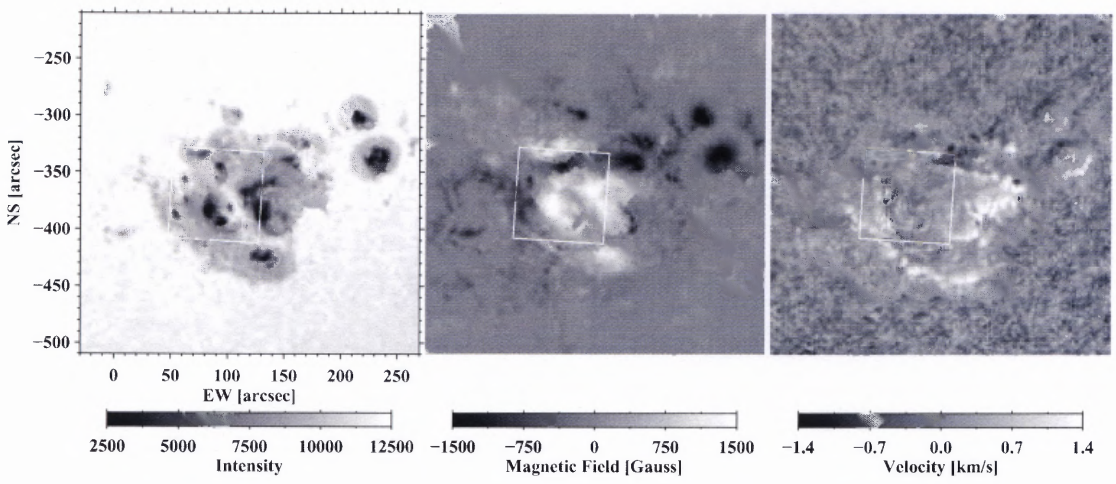

Figure 5.1 From left to right: maps of MDI continuum intensity, LOS magnetic field, and LOS Doppler velocity. The data were obtained on 2003 October 29 at 19:12 UT, 85 min before the beginning of the X10 flare. The region outlined by the slightly inclined white box is the FOV of the high-resolution observations. The velocity gradient due to solar rotation has been removed from the Dopplergram.

high level of activity observed in this active region. Liu et al. (2006) presented a multi-wavelength study focusing on the global large-scale activity associated with the X10 flare, including remote brightenings detected in Hα and soft X-rays, Moreton waves in the line wing of Hα, and Type II radio bursts. Xu et al. (2004) presented high-resolution near infrared observations of the X10 flare.

This chapter presents results of multi-wavelength high-resolution LCT flow fields in active region NOAA 10486 associated with the X10 flare. The following two aspects are addressed: (I) flow fields at different photospheric layers and (II) temporal variations of flow fields associated with the occurrence of the X10 flare. The outline of this presentation is as follows: The high-resolution observations obtained with the AO system are introduced in Section 5.3. Data reduction and processing are described in Section 5.4. The limitations of the observations are summarized in Section 5.5. The results are presented in Section 5.6: For Aspect I, the flow speeds in different regions are compared for the three wavelengths. For Aspect II, the variations of the

flows from the pre- to post-flare phase are examined. The results are summarized and discussed in Section 5.7.

5.3 Observations

5.3.1 High-Resolution Observations in Multi-Wavelength

The high-resolution observations were taken at the NSO/SP with the 76 cm DST. The high-order AO system was used to achieve diffraction-limited imaging with a high signal-to-noise ratio (Rimmele 2000; Rimmele et al. 2003). AO-corrected data were simultaneously acquired in G-band, white-light, and near infrared. In all of the cases, the images were oversampled providing more reliable information at high-spatial frequencies. The diffraction limit ($\theta = \lambda/D$) of the 76 cm DST is $0.12''$ at G-band ($\lambda = 4305$ Å), $0.14''$ at white-light ($\lambda = 5270$ Å), and $0.42''$ at near infrared ($\lambda = 1.56$ μm). Observations started at 15:16 UT and ended at 21:19 UT on 2003 October 29. The observed FOV covers the central part of the super active region NOAA 10486. Figure 5.1 shows the whole active region in MDI continuum, magnetogram, and Dopplergram at 19:12 UT on 2003 October 29. The region outlined by a slightly inclined white box is roughly the FOV of the high-resolution observations. The X10 flare occurred in the active region within the observed FOV. It began at 20:37 UT, peaked at 20:49 UT, and ended at 21:01 UT. The temporal coverage of the data sets is shown in Figure 5.2.

G-band images were obtained using a 5 Å wide interference filter centered at the CH-band head at 4305 Å. The G-band observations were taken with a 1032 $\times$ 1032 pixels CCD with an image scale of $0.07''$ pixel^{-1}. The FOV was approximately $72'' \times 72''$. The exposure time was 2 ms and cadence was 2 s. The best images were selected every 20 s for further processing and analysis using the image contrast as a selection criterion.

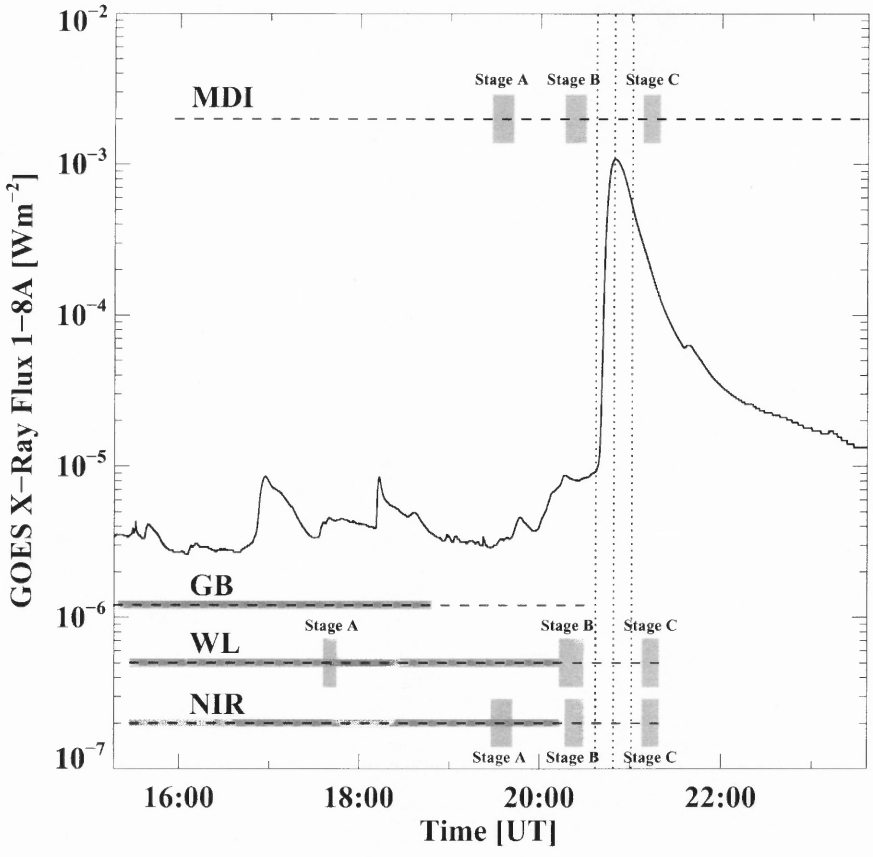

Figure 5.2 GOES soft X-ray flux in the range 1−8 Å on 2003 October 29. The X10 flare started at 20:37 UT, peaked at 20:49 UT, and ended at 21:01 UT as indicated by the three vertical dotted lines. The horizontal dashed lines indicate the duration of the data sets. There are some data gaps during these time intervals. The horizontal solid lines superposed on each dashed lines represent the time range over which the flow fields are averaged for Aspect I. The widths of the vertical gray bars indicate the time stages over which the data are averaged for Aspect II.

Green continuum white-light data were obtained with a 52 Å bandpass interference filter centered at 5270 Å and recorded by a 1024 × 1024 pixel, 12-bit Dalsa 1M15 CCD camera. The FOV was 81″ × 81″, which corresponds to an image scale of 0.08″ pixel^{-1}. The exposure time was 4 ms. The best frame with the highest granular rms-contrast was selected out of a total of 200 frames every minute.

In addition to the G-band and white-light data, near infrared data were recorded at 1.56 μm with the band pass restricted to 50 Å by an interference filter.

There are a few Fraunhofer lines within this 50 Å range, but they contribute less than 3% to the radiation passing through the filter. Therefore, the continuum contamination is negligible. The near infrared camera is based on a liquid nitrogen cooled HgCdTe/Al_2O_3 Focal Plane Array (FPA) with 1024 × 1024 pixels and 14-bit digitization depth (Cao et al. 2005). The FOV was 91″ × 91″ resulting in an image scale of 0.09″ pixel^{-1}. The exposure time was 13 ms, which is sufficiently short to freeze the atmospheric wave front aberrations in the near infrared. The best frame with the highest granular rms-contrast was selected every minute out of a total of 50 frames.

5.3.2 Full-Disk MDI Magnetograms and Dopplergrams

The space observations from the MDI (Scherrer et al. 1995) on board SOHO (Domingo et al. 1995) provide a unique opportunity to study the structure and evolution of the LOS component of magnetic and velocity fields in full-disk mode. The MDI observations are made in the Ni I photospheric absorption line at 6767.8 Å with a typical cadence of 1 min and an image scale of 2″ pixel^{-1}. MDI data from 15:56 UT on 2003 October 29 to the next day at 02:59 UT were used in this study.

5.3.3 High Resolution TRACE Coronal Images

Coronal images observed by TRACE (Handy et al. 1999) in the Fe XII/XXIV line at 195 Å are used to study any change of the magnetic field topology in the lower coronal environment (T ≈ 1.5 × 10^6 K) between pre- and post-flare states.

5.4 Data Reduction

After flat-field and dark-frame correction, each time series (G-band, white-light, and near infrared) were carefully aligned by removing the rigid displacement due to seeing and telescope guiding errors with respect to a reference image. In order to further

reduce the atmospheric distortion, a destretching algorithm (Shine et al. 1994) was applied using running references.

LCT is a powerful cross-correlation technique for the precise measurement of the proper motion of contrast features seen in successive images of a time-series of solar images. The cross-correlation is defined as a function of position in the image, within a spatially localized apodization window (a two-dimensional Gaussian function). The window size and seeing define the effective resolution of the vector displacement determination (November & Simon 1988). The Interactive Data Language (IDL) implementation of the LCT algorithm (Version 3 released on 1999 February 3, http://ana.lmsal.com/ana/) was used in this study, which works by comparing bounded cells in each image with the same cells in the subsequent image. The rigid shift that gives the best match for each cell is interpreted as an horizontal displacement vector (dx, dy) for the center of the cell. The shifts are applied to all the cells in opposite direction to guarantee stable behavior near zero shift values. The data values in a cell are apodized with a centered Gaussian. This causes features near the center to be weighted more than those near the perimeter of each cell and determines the spatial resolution of the LCT flow map (Shine et al. 2000). For the present work a cell size of 32×32 pixels was used. The cell centers are spaced one pixel apart in order to show fine-structure contents of the flow field brought out by high-resolution imaging. Considering that the three data sets were obtained at different wavelengths and have different image scales, the same Gaussian weighting function with a FWHM of $1.4''$ (corresponding to 20 pixels in G-band, 18 pixels in wight-light, and 16 pixels in near infrared) was applied to the respective data sets, which guarantees that the LCT flow maps have the same spatial resolution ($1.4''$ or 1200 km on the solar surface) by tracking the same features. The measured displacements were then converted to horizontal velocity vectors at the centers of the cells by taking into account the elapsed time between two successive images.

Table 5.1. Time Average Flow Maps (Aspect I)

Wavelength	Time (UT)	Number of FMs
NIR	15:27 ~ 20:13	206
WL	15:27 ~ 20:13	90
GB	15:19 ~ 18:48	443

The individual flow maps are noisy, due to both residual seeing distortion and intensity variations of the 5-minute oscillation. The noise can be significantly reduced by averaging the flow maps leaving reliable systematic motions, since temporally averaging the time-series of flow maps does not add the contributions from random noises but adds those from proper motions. For data presented here, one-hour averages show an organized pattern with persistent velocity features down to the resolution limit (1.4″). As long as the flow fields do not substantially change, averaging over more flow maps or longer time period improves the signal-to-noise ratio and provides more accurate result. The time sequence was divided into several intervals and the data sets were interlaced to verify that the flow patterns were persistent before the occurrence of the X10 flare. Averages were taken from 15:27 UT to 20:13 UT over all 206 and 90 flow maps for near infrared and white-light data sets, respectively. After 18:48 UT the FOV of G-band data changed significantly. Therefore, the average over 443 flow maps from 15:19 UT to 18:48 UT was taken for G-band data. Table 5.1 provides the information (time range and number of Flow Maps (FMs)) for calculating the Average Flow Maps (AFMs) for the three wavelengths settings. The time ranges are also shown in Figure 5.2 as horizontal solid lines. The average flow maps for the three wavelengths will be used to compare horizontal velocity fields at different altitudes, which will address Aspect I.

White-light and near infrared data cover the flare, which gives us a chance to investigate any change in horizontal velocity fields associated with the flare. Three time stages (A, B, and C) are defined. Stage A serves as reference and is far before the

Table 5.2. Time Stage Average Flow Maps (Aspect II)

Wavelength	Stage A Time (UT)	FMs	Stage B Time (UT)	FMs	Stage C Time (UT)	FMs
NIR	19:28 ~ 19:42	12	20:17 ~ 20:29	12	21:08 ~ 21:19	12
WL	17:36 ~ 17:45	9	20:13 ~ 20:29	9	21:08 ~ 21:19	9
Magnetogram	19:28 ~ 19:42	13	20:16 ~ 20:30	15	21:08 ~ 21:19	10
Dopplergram	19:28 ~ 19:42	15	20:16 ~ 20:30	15	21:08 ~ 21:23	15

flare. Stages B and C are the pre- and post-flare phase, respectively. The post-flare average flow map for near infrared is obtained by averaging all the 12 flow maps in time Stage C. The post-flare average flow map for white-light is the result of averaging all 9 flow maps. The investigation of the flare-associated changes in the flow fields can be made by comparing the average flow maps in the post- and pre-flare phases. In order to compare them fairly, the same number of flow maps have to be combined in pre-flare phase for each wavelength setting. Therefore, 12 and 9 successive flow maps were averaged just before the flare for near infrared and white-light, respectively, which cover time Stage B. The averages over 12 and 9 consecutive flow maps in time Stage A were also taken for reference purpose for near infrared and white-light, respectively. Table 5.2 provides information for these time stages. The time stages are also shown in Figure 5.2 by gray vertical bars in the background of the dashed lines. Note that Stage C began 7 min after the end of the flare. Stage B ended 7 or 8 min before the beginning of the flare. Stages B and C are about 50 min apart. Stages A and B are also about 50 min apart. The only reason for choosing Stage A far before Stage B for white-light is the lack of white-light data during the proper time period. These time stage average flow maps will be used to study the temporal variation of the mass flow associated with the occurrence of the X10 flare, which will address Aspect II.

Solar differential rotation was corrected before analyzing the MDI time-series data using standard procedures in SolarSoftWare (SSW, Freeland & Handy 1998).

In order to co-align MDI data with the small FOV of the high-resolution data, MDI images were rotated counterclockwise by 3.75°. MDI magnetograms and Dopplergrams are also averaged in each time stage corresponding to those for high-resolution average flow maps mentioned above.

5.5 Limitations of the Observations

Some limitations of the observations are summarized in the following list:

1. *Image Motion and Seeing.* Although the high-order AO system was used to observe, some residual seeing contributions remain. The images were rigidly aligned. However, sub-pixel shifts were not corrected. In addition, the AO correction is best near the lock point of the AO system and decreases towards the image periphery (Denker et al. 2007b). Frame selection has been employed to improve the image quality. Differential image motion was corrected by a destretching algorithm. Taking into account the wavelength dependence of the image stability ($r_0 \sim \lambda^{6/5}$, Roddier 1999), the image quality is in general the best in near infrared and worst in G-band images. However, the contrast is highest in G-band resulting in a higher accuracy of LCT techniques.

2. *Data Gap and Duration.* The typical cadence of the observed data is 1 min for near infrared and white-light and 2 s for G-band. However, not all images are equally spaced in time. There are some data gaps as large as 20 min to 60 min. There is no sufficient data after the X10 flare to conclusively address the post-flare evolution. The observations ended at 21:19 UT, i.e., 18 min after the end of the flare, which leaves us with only 12 and 9 flow maps after the flare in near infrared and white-light, respectively. In addition, although the X10 flare ended at 21:01 UT as reported by GOES, it was actually a long-duration event. The GOES flux did not restore to the pre-flare level even after 22:00 UT. For

these reasons, it is not clear whether the changes in the horizontal flow fields associated with the flare are permanent or temporary.

3. *Uncertainties Related to LCT.* LCT identifies certain features based on their intensity contrast and size. It provides more reliable results when the local contrast does not significantly change within two successive images. Otherwise, it is uncertain whether LCT tracks real plasma motions or just optical flows. Detailed discussions of the limitations of LCT and alternate methods to determine optical flows are given in, for example, Potts et al. (2003, 2004) and Schuck (2006)

4. *Uncertainty of Dopplergrams and Magnetograms.* The MDI instrument measures the line shift parameters of Ni I 6767.8 Å spectral profile and then converts them to the Doppler shift using a nearly linear approximation, i.e., weak magnetic/velocity field approximation (Scherrer et al. 1995; Qiu & Gary 2003). Generally, for each pixel, the uncertainty for Dopplergram and magnetogram is equivalent to 20 m s^{-1} and 20 Gauss, respectively. When the magnetic or velocity field is very strong however, e.g., in a complex sunspot, there will be some cross-talk between magnetogram and Dopplergram, which leads to a larger uncertainty.

5.6 Results

5.6.1 Aspect I: Flow Fields at Different Photospheric Layers

The height range covered in the observations includes the levels of near infrared, white-light, and G-band. The formation height for near infrared at 1.56 μm is about 50 km below the $\tau_{5000} = 1$ level, which is about half a scale height (Wang et al. 1998). The G-band forms in the mid-photosphere over a broad height range from 0 to 300 km above the $\tau_{5000} = 1$ level (Rimmele 2004). White-light at 5270 Å represents

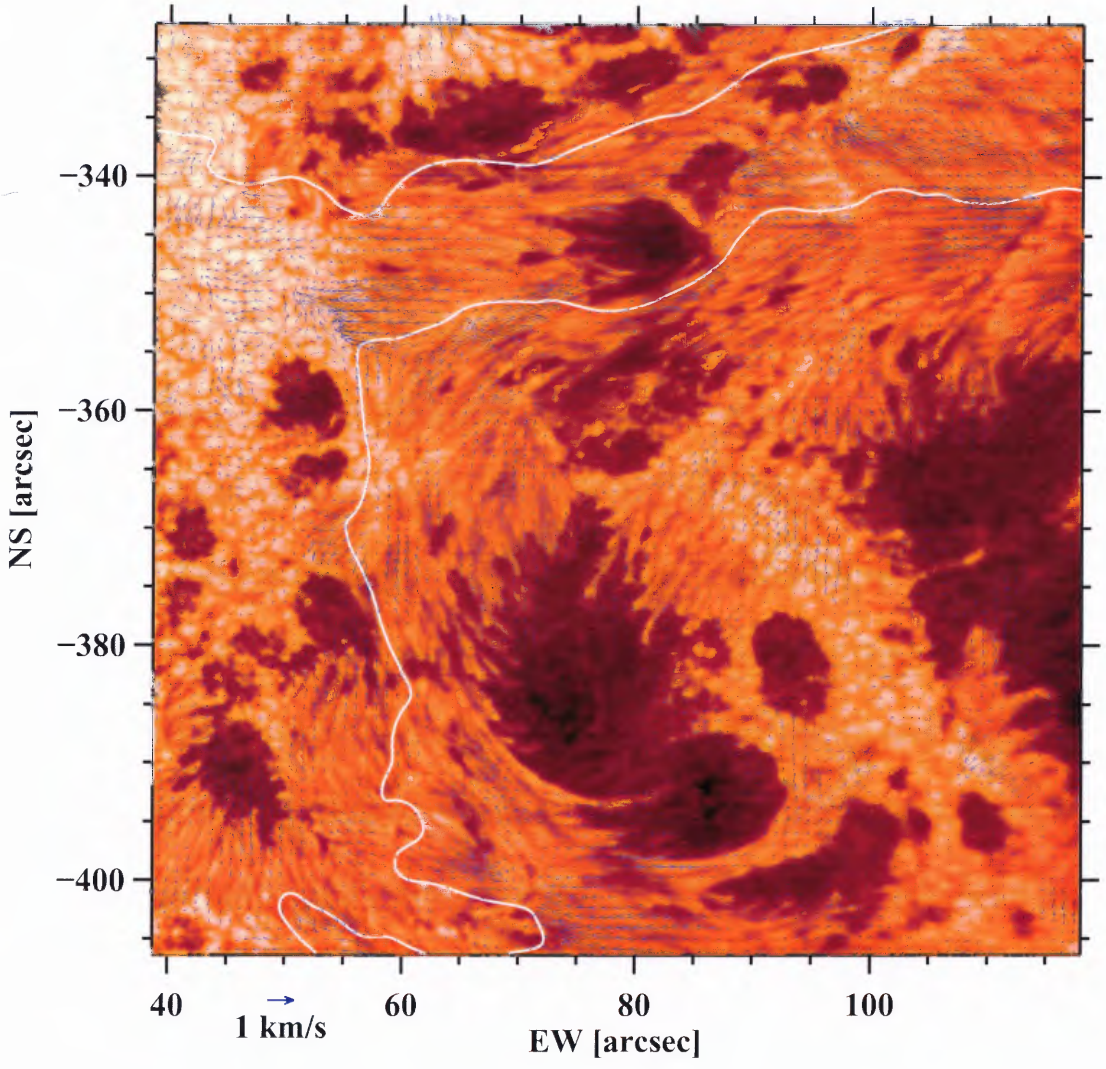

Figure 5.3 High-spatial resolution near infrared image at 18:14 UT on 2003 October 29. The white contours mark the magnetic neutral line. The arrows show the average flow vectors over the time period from 15:27 UT to 20:13 UT obtained with LCT.

the information at the solar surface. This section concentrates on the average flow maps of the three wavelengths averaged before the X10 flare on 2003 October 29.

Figure 5.3 shows the flow vectors of near infrared average flow map and LOS magnetic neutral lines superposed on the near infrared intensity image at 18:14 UT. Penumbral and umbral fine structures can clearly be seen in this kind of high-resolution image. Movies of the intensity time sequences clearly show oppositely

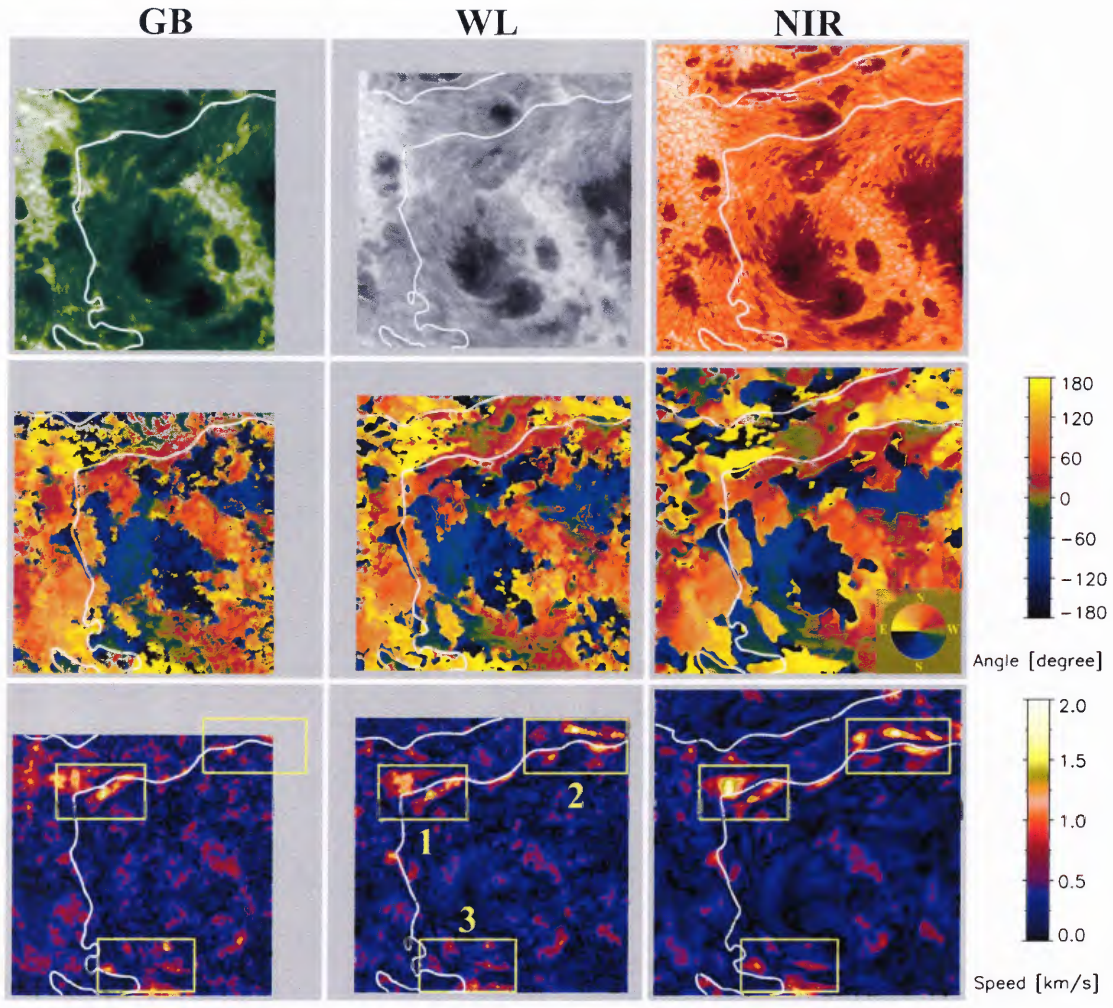

Figure 5.4 The top row from left to right are G-band (GB), white-light (WL), and near infrared (NIR) intensity images on 2003 October 29 at 18:14 UT. The middle row are the respective azimuth maps of the average flow maps, a color-coded disk has been inserted into the rightmost panel as a visualization guide of the azimuth angle. The bottom row are the respective speed maps of the average flow maps. The magnetic neutral lines based on co-aligned MDI LOS magnetograms are superposed on each map. The average flow maps are averaged over the time periods as shown in Figure 5.2 by horizontal solid lines. Boxes 1, 2, and 3 are regions with strong shear motions, which are used in studies of the detailed speed distributions shown in Figure 5.5.

directed parallel flows, i.e., horizontal shear flows, along the neutral lines for all three wavelengths. Figure 5.4 shows the intensity maps at the three wavelengths in the top row. The vector average flow maps were decomposed into azimuth (middle row) and speed (bottom row) maps for each pixel in the FOV. This kind of display can better distinguish the fine-structure contents of the flow fields inherent to the high-resolution observations. The flow fields at the three wavelengths show very similar patterns both in the azimuth and speed maps, indicating that the flow is maintained over the height range from near infrared to G-band. The azimuth maps illustrate that the flow angle difference between the two sides of the neutral lines is around 180° ranging from 135° to 225° at certain places, which is the signature of the shear flow. These shear flows also have the highest speed in the entire FOV as shown in the speed maps. Yang et al. (2004) studied these strong shear flows using speckle masking reconstructed images based on white-light intensity data. The authors reported that the flow speed can reach up to 1.6 km s^{-1}. In the present work, the average flow maps of near infrared, white-light, and G-band give a similar result. In particular, the strong horizontal shear flow in the order of 1.0 km s^{-1} along the neutral line is present for at least 5 hours before the flare. The size of the regions showing horizontal shear motion is typically $25'' \times 10''$. These strong shear motion regions are outlined by Boxes 1, 2, and 3 and the flow speed distributions are computed within each box region for all three wavelengths. The results are shown in Figure 5.5. The flow speeds at the three wavelengths have similar distributions with slight differences at the high speed end. The majority of the data have speeds of less than 0.5 km s^{-1}. Since large shear flow speeds are more interesting, the values at the 10th percentile of the high speed end are calculated, i.e., 10% of the data points have speeds exceeding this value. Vertical lines are plotted at these values, which are also included in the plots as well. Note that G-band data do not cover the whole area of Box 2. Therefore, the result of G-band data in Box 2 should be interpreted with caution. These plots illustrate that at the

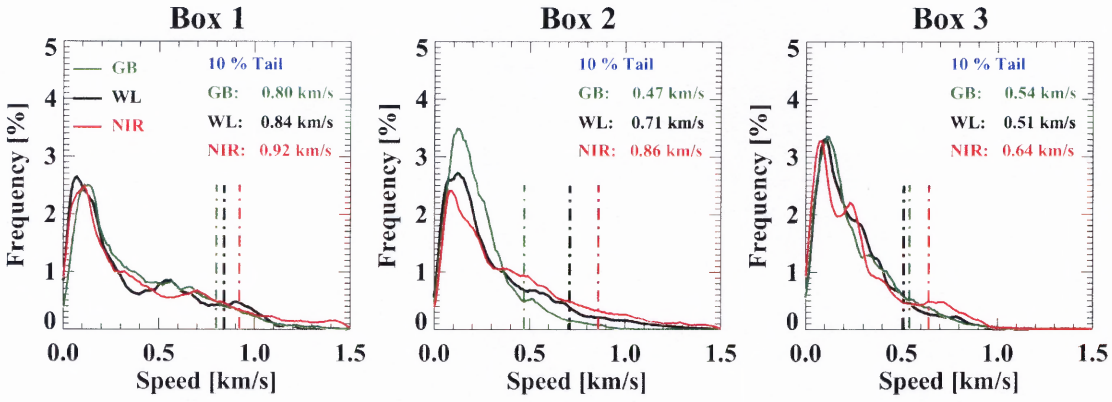

Figure 5.5 Flow speed distributions for G-band (GB), white-light (WL), and near infrared (NIR) in regions outlined by Boxes 1, 2, and 3 in Figure 5.4, respectively. The vertical dot-dashed lines mark the speed values at the 10th percentile of the high speed end.

10th percentile of the high speed end, the speed is largest in the near infrared, while the G-band speed is smallest with only one exception in Box 3, where the white-light speed is slightly smaller compared to the G-band. Despite this exception, an inference can be made that from the height (-50 km) close to where the 1.56 μm continuum is formed to the height of G-band formation (300 km), the flow direction remains the same while the shear flow speed decreases in the shear motion regions.

Table 5.3 is provided in order to quantitatively compare the flow speeds in other regions besides the shear motion regions for the three wavelengths. Figure 5.6 shows the selected regions for this purpose. Note that the shear motion regions are generally inside the sunspot penumbra. Only penumbral regions without shear motions are considered as the general penumbral regions in Table 5.3. In the shear motion regions, the result is consistent with that shown in Figure 5.5, i.e., the shear flow speed decreases with the increasing height. In contrast, the flow speed increases with increasing height in other regions, such as the quiet Sun, the penumbra, and the umbra.

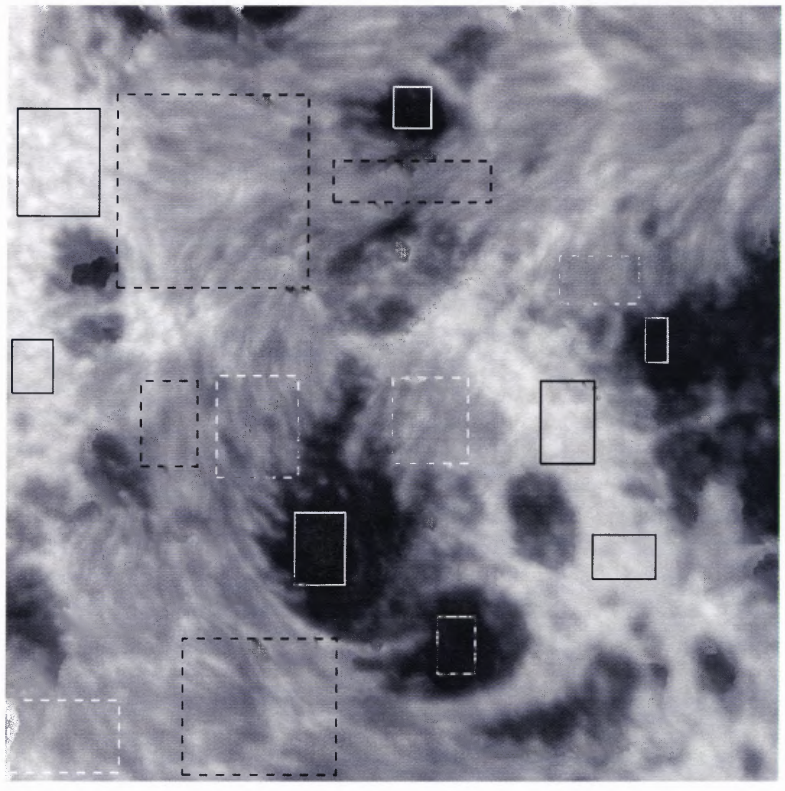

Figure 5.6 The selected regions for Table 5.3. The quiet Sun regions are outlined by black solid boxes. The penumbral regions without shear motion are outlined by white dashed boxes. The umbral regions are outlined by white solid boxes. The regions with shear motions are outlined by black dashed boxes. The background is the white-light image at 18:14 UT on 2003 October 29.

5.6.2 Aspect II: Variation of Flow Fields Associated with Flare

This part of the study concentrates on the magnetic and velocity fields averaged within the time stages right before and right after the X10 flare obtained with MDI, near infrared, and white-light data. Figure 5.7 shows the stage-averaged MDI magnetograms, Dopplergrams, and flow speed maps in near infrared and white-light at three time stages: far before the flare (Stage A), right before the flare (Stage B), and right after the flare (Stage C), and their respective difference images (Stages B−A and C−B). The data of Stage A and the difference of Stages B−A are used as reference to check whether features are associated with the occurrence of the flare or not. Since the observed active region was close to central meridian (μ=cos $\theta \approx$0.9),

Table 5.3. Horizontal Flow Speeds

Wavelength	Quiet Sun [km s^{-1}]	Penumbra [km s^{-1}]	Umbra [km s^{-1}]	Shear Motion Region [km s^{-1}]
GB	0.37 ± 0.23	0.24 ± 0.11	0.12 ± 0.08	0.29 ± 0.23
WL	0.25 ± 0.13	0.21 ± 0.11	0.09 ± 0.07	0.31 ± 0.26
NIR	0.26 ± 0.15	0.19 ± 0.13	0.07 ± 0.06	0.34 ± 0.30

the MDI LOS magnetic and velocity field can be treated as vertical ones. For the convenience of description and analysis, the neutral line is divided into three parts, as shown in the first panel of Figure 5.7, in which NL3 is the site where the X10 flare occurred. At the left side of NL3, the MDI Dopplergrams appear white (redshifted downflow), while at the right side, they appear black (blueshifted upflow), which indicates strong persistent vertical shear flows along NL3. The size of the region showing vertical shear motion is typically $20'' \times 40''$. The speed of strong vertical shear flows is also in the order of 1 km s^{-1}.

After the flare, the LOS magnetic field has a rapid and significant change: Both the left side negative polarity and the right side positive polarity dramatically decayed near NL3, which is illustrated by the difference magnetogram of Stages C−B as the originally black region becomes white at the left side and originally white region becomes black at the right side of NL3. Thus, the magnetic gradient near NL3 decreased after the flare. Meanwhile, the vertical shear flow enhanced after the flare, which can be seen from the difference Dopplergram of Stages C−B as the originally white region becomes brighter and the originally black region becomes darker along NL3. The reference difference images do not show this kind of distinct change. Therefore, a conclusion can be made that the rapid and dramatic changes in the LOS magnetic and velocity field near the neutral line, where the flare occurred, are associated with the flare. Moreover, the regions that have the largest change in magnetic field and in velocity field are the same. They are also spatially correlated with the flare kernels (see Figure 1 in Yang et al. 2004) as well as the 50−100 keV

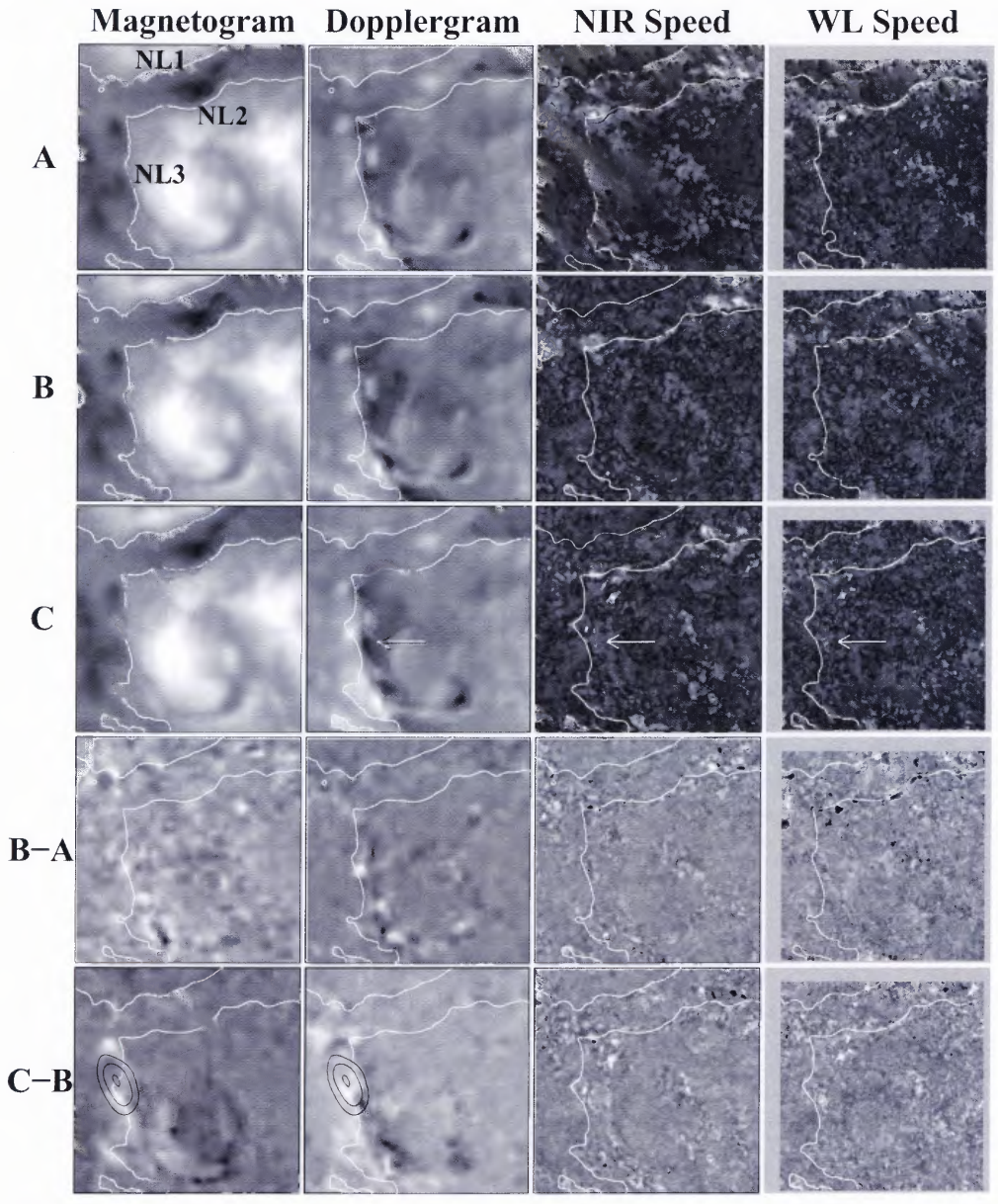

Figure 5.7 From left to right are stage-averaged MDI magnetogram, Dopplergram, near infrared flow speed map, and white-light flow speed map. Stage A corresponds to the first row, Stage B to the second row, and Stage C to the third row. The stage divisions are shown in Table 5.2 or in Figure 5.2 as the gray vertical bars. The FOV of MDI magnetograms and Dopplergrams are the same as near infrared maps. The forth row are the difference maps of the corresponding maps in Stage B minus Stage A. The fifth row contains the respective difference maps of Stage C minus Stage B. Appropriate magnetic neutral lines are superposed on each map. The black concentrical contours in the fifth row show a snapshot of the strongest RHESSI 50−100 keV hard X-ray source in levels of 50%, 70%, and 90% of the maximum counts integrated from 20:40 UT to 20:41 UT. The arrows mark the region with increased horizontal flow speed after the flare. It is also the region with upflow shown in the Dopplergrams.

hard X-ray source observed by the RHESSI, which is shown as black contours in Figure 5.7. Note that Figure 5.7 only shows a snapshot of the strongest hard X-ray source shortly after the flare onset. The evolution of the RHESSI hard X-ray sources during the flare were studied in detail by Liu et al. (2006). The changes in horizontal flow fields are not so obvious as those in vertical flow fields. The situation is more complicated owing to the fact that the horizontal flow fields are two-dimensional instead of one-dimensional for the vertical flow fields. Nevertheless, the region with increased horizontal flow speed can still be identified near NL3 after the flare. They are indicated by the arrows in Figure 5.7. They also correspond to the upflow region shown in the Dopplergrams.

To examine the complete evolution of the magnetic gradient near NL3 region and its correlation with the flare, a mask is constructed that encompasses regions immediately near NL3 and the magnetic gradient is calculated within the mask based on the time-series of MDI LOS magnetograms. Figure 5.8 shows the time-averaged magnetogram (Panel 5.8a), the magnetic gradient image constructed using the time-averaged magnetogram (Panel 5.8b), the magnetic gradient image within the mask (Panel 5.8c), and the evolution of the mean magnetic gradient within the mask (Panel 5.8d). The time-averaged magnetogram was used to define the mask. The magnitude of the gradient of the LOS magnetogram is defined as $\mid \nabla B_z \mid = \sqrt{(\partial B_z/\partial x)^2 + (\partial B_z/\partial y)^2}$. The mean magnetic gradient near NL3 suddenly and permanently decreased from 0.16 G km^{-1} before the flare to 0.14 G km^{-1} after the flare.

Although there is not sufficient high-resolution data after the X10 flare, MDI Dopplergrams give us an opportunity to study the complete evolution of the vertical shear flow associated with the flare. Figure 5.9 shows the evolution of the vertical shear flow speed measured in the region outlined by the box covering NL3. The vertical shear flow speed is defined as the difference between the mean downflow and

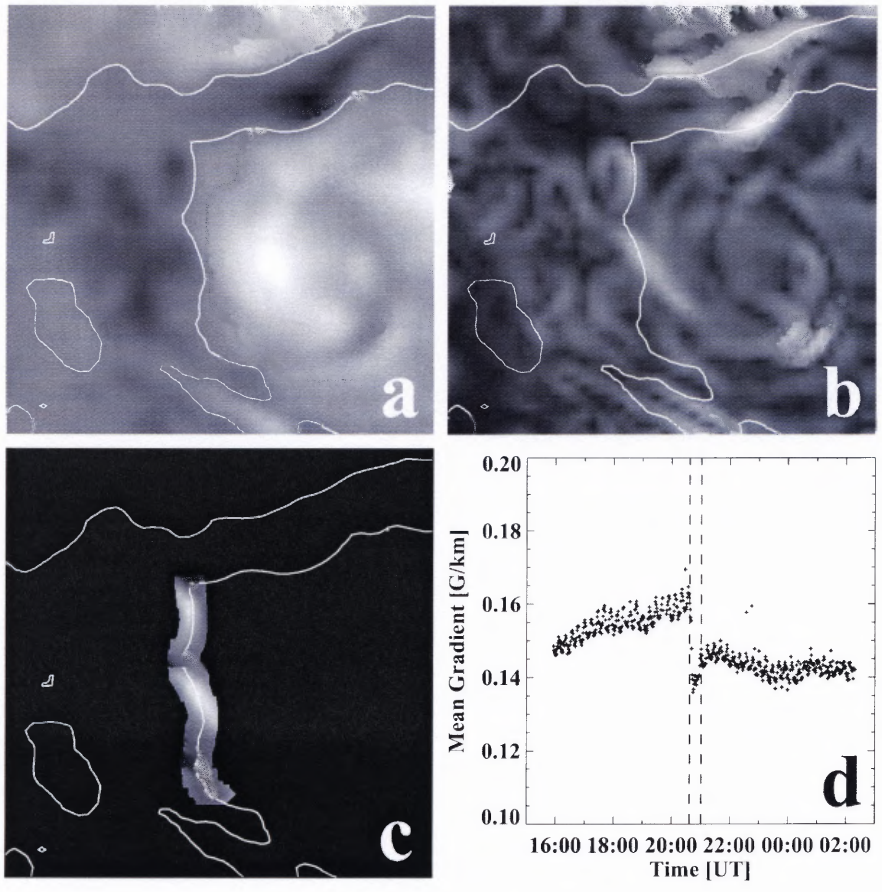

Figure 5.8 (a) Time-averaged magnetogram corresponding to the time period from 15:56 UT on 2003 October 29 to 02:18 UT on the following day. The contour is the magnetic neutral line based on the average magnetogram. (b) Magnetic gradient image calculated using the time-averaged magnetogram. (c) Magnetic gradient within the mask encompassing NL3 region. The mask is obtained from the time-averaged magnetogram. (d) Evolution of the mean magnetic gradient within the defined mask calculated from the time-series of LOS magnetograms. The two vertical dashed lines mark the beginning and end of the X10 flare.

upflow speeds within the region of interest. The vertical shear flow speed increased gradually and continuously before the flare. Subsequent to the flare it suddenly increased, then dropped to a level higher than the value before the flare, and kept slowly increasing.

In order to study the changes of the horizontal flow fields relative to the neutral line, they are decomposed into shear flow (tangential) components and

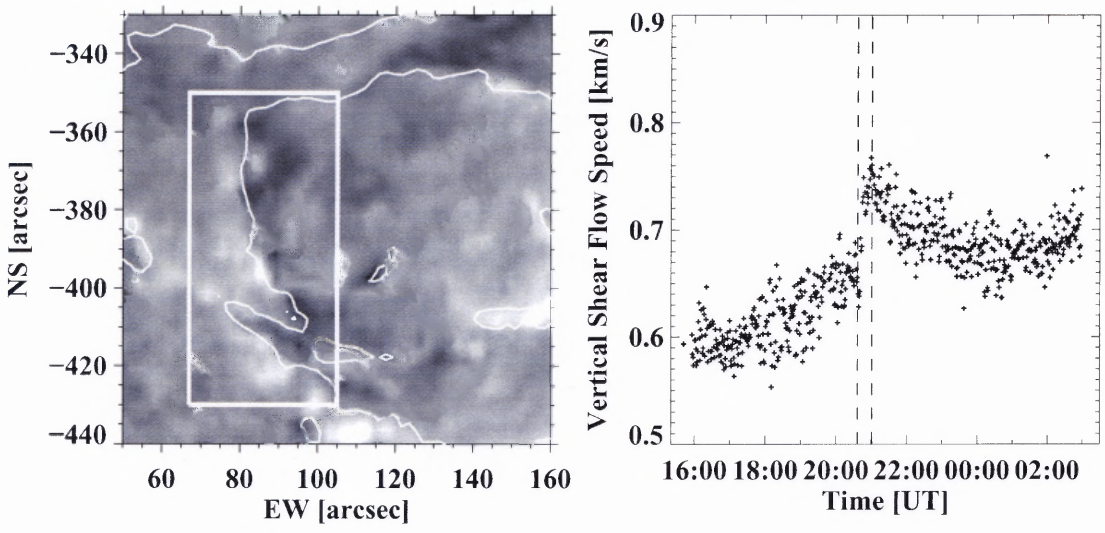

Figure 5.9 The left panel is the MDI Dopplergram at 19:12 UT on 2003 October 29 superposed with the magnetic neutral line. The right panel shows the evolution of the vertical shear flow speed calculated in the box region of the left panel. The two vertical dashed lines mark the beginning and end of the X10 flare.

converging/diverging flow (normal) components with respect to the neutral line. Figure 5.10 depicts the decompositions of the horizontal velocity field. The solid arc is a small section of the neutral line. A Local Tangential (LT) line and a Local Normal (LN) line are plotted on an arbitrary point NL[j] on the neutral line. At one side of the neutral line, the flow velocity v_1 at location $P[m]$ is decomposed into tangential component v_{t1} and normal component v_{n1}. D is the perpendicular distance between $P[m]$ and the neutral line. The local shear flow angle S_1 is defined as the angular separation between the directions of the local flow field and the neutral line's local normal. On the other side of the neutral line, flow velocity v_2 and local shear flow angle S_2 at location P[n] is decomposed and defined in a similar way. The shear flow angle corresponding to the neutral line's local point NL[j] is defined as $S = (\overline{S_1} + \overline{S_2})/2$, where $\overline{S_1}$ and $\overline{S_2}$ are the average values of the local shear flow angles at opposite sides of the neutral line, respectively. A shear flow angle of 90° represents the highest shear and 0° represents no shear. The shear flow speed corresponding to the neutral line's local point NL[j] is defined as $v_t = |\overline{\vec{v}_{t1}} - \overline{\vec{v}_{t2}}|$, where $\overline{\vec{v}_{t1}}$ and $\overline{\vec{v}_{t2}}$ are

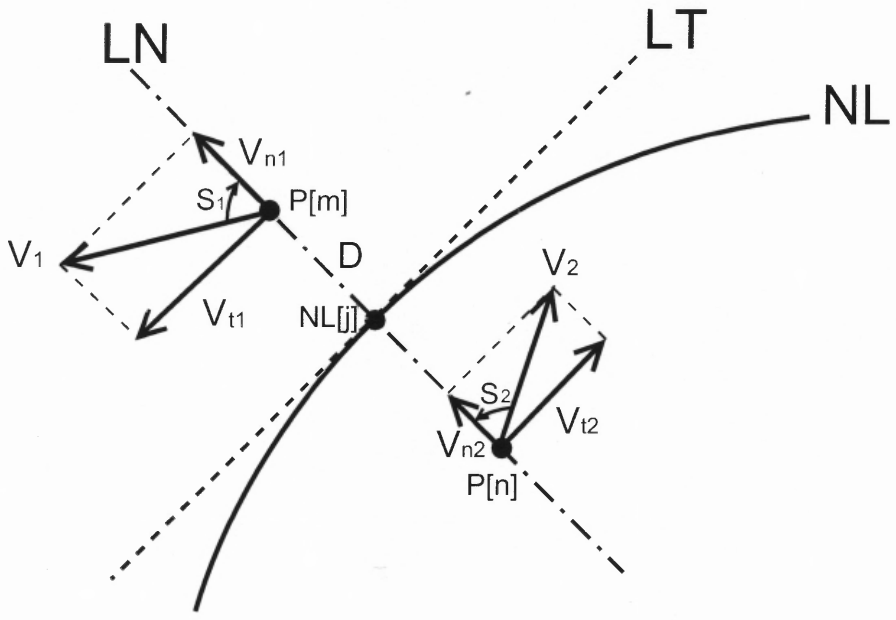

Figure 5.10 This cartoon shows the decomposition of flow fields into tangential and normal components with respect to the neutral line. NL[j] is a local point on the neutral line (NL). P[m] is a point on the local normal (LN) of the neutral line at one side. P[n] is a point on the local normal at the other side. The tangential components of the flow fields contribute to the shear flow speed. The angle S_1 and S_2 are defined as local shear flow angles.

the average results of the tangential components of the flow fields at two opposite sides of the neutral line. The closer to the neutral line, the more important becomes the shear flow field. Therefore, the aforementioned quantities are averaged using the importance, i.e., the inverse of the perpendicular distance between the flow field and the neutral line, as weight: $\overline{X} = \sum X_i {D_i}^{-1} / \sum {D_i}^{-1}$, where X represents either S_1, S_2, $\vec{v}_{t1}$, or $\vec{v}_{t2}$. The flow fields within 2.4″ (1,740 km on the solar surface) to the neutral line are taken into account for the results to be presented next.

For each stage-averaged average flow maps, shear flow angle and shear flow speed corresponding to each point on the neutral lines are calculated for near infrared and white-light using the above definitions. Figures 5.11 and 5.12 visualize the results, in which the centroids of the highlighted lines are the locations of the neutral lines and the local thickness of the lines is proportional to the magnitude of the shear flow

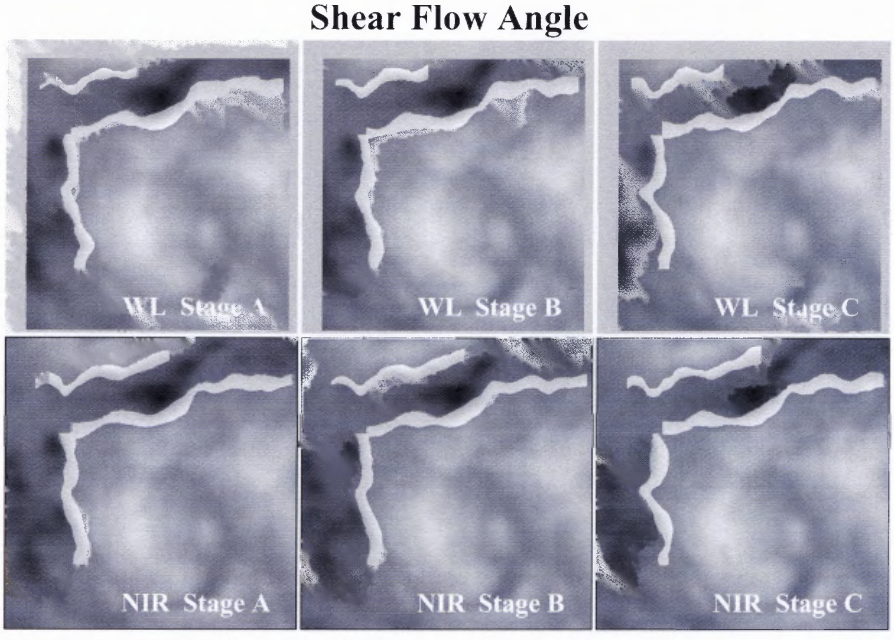

Figure 5.11 The background gray scale images correspond to the mean MDI LOS magnetograms at the three time stages. The highlighted lines center at the locations of the three neutral lines. The local thickness of these lines indicates the magnitude of the shear flow angle calculated for that location.

angle or shear flow speed calculated for that location of the neutral line. Both the shear flow angle and shear flow speed increased right after the flare along NL3 as the lines along NL3 become thicker from Stage B to Stage C. This type of increase is not obvious along NL1 and NL2. Near infrared data provide more pronounced results compared to white-light for the following reasons: (1) The near infrared average flow map in each time stage averages 12 flow maps while white-light average flow map is comprised of only nine flow maps; (2) The seeing and thus the quality of LCT flow map improves proportional to $\lambda^{6/5}$. In the near infrared at 1.56 μm it is about four times better than in white-light at 5270 Å. The shear flow angle increased up to 27° and the shear flow speed increased up to 0.2 km s^{-1} at some locations of NL3. Liu et al. (2005) studied the same active region using vector magnetograms observed in the Fe I 5250 Å absorption line. They defined the magnetic shear angle as the angular difference between the potential and the measured transverse fields, weighted by the

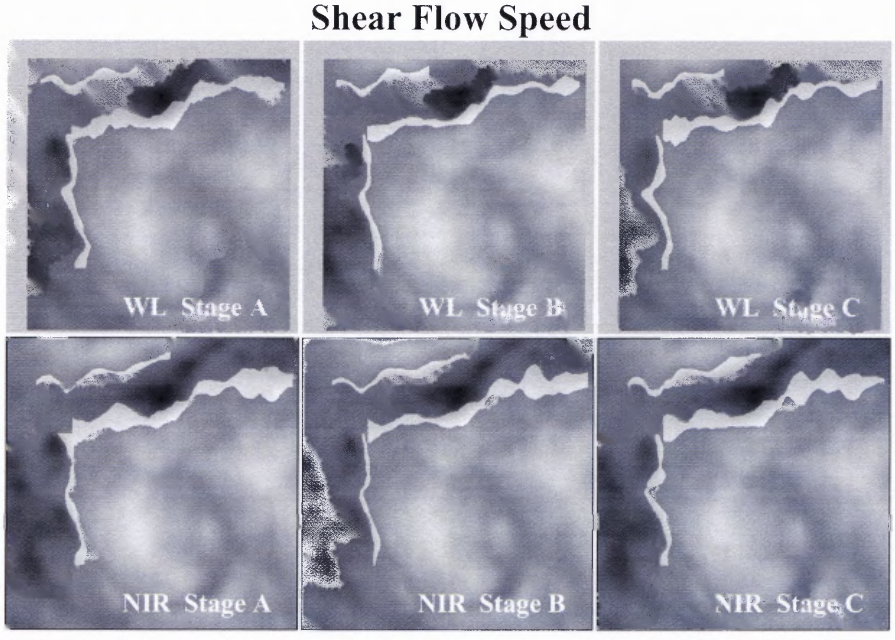

Figure 5.12 Same as Figure 5.11 but the local thickness of the lines indicates the magnitude of the shear flow speed calculated for that location.

measured transverse field strength. They discovered an 10° increase of the weighted mean magnetic shear angle around NL3 right after the X10 flare (see Figures 3 and 4 in Liu et al. 2005). The increase of the magnetic shear found in Liu et al. (2005) is temporally and spatially consistent with the increase of the shear flow found in this study, which indicates that magnetic shear and shear flow are highly connected and closely related to flare production.

5.7 Summary and Discussion

This chapter has presented photospheric horizontal flow fields in super active region NOAA 10486 derived using LCT from successive AO-corrected, high-spatial resolution intensity images in G-band, white-light, and near infrared obtained with the DST at NSO/SP. MDI LOS Dopplergrams and magnetograms were also used to study the vertical velocity field and the relationship between the flow and magnetic fields. Strong shear flows, both horizontal and vertical, were observed along certain locations

of the magnetic neutral lines. These strong horizontal and vertical shear flows, both in the order of 1 km s^{-1}, are persistent and long-lived (at least 5 hours) before the occurrence of an X10 flare. The time sequences were divided into several intervals and the data sets were interlaced to verify that the horizontal flow patterns were consistent and did not change dramatically before the flare. From 50 km below the solar surface observed in the 1.56 μm near infrared continuum up to 300 km above the solar surface observed in the G-band, the spatial structures of the horizontal flow fields remained the same, while the flow speeds in the shear motion regions decreased and contrarily those in other regions, such as quiet Sun, sunspot penumbra, and umbra, increased with increasing height. After the flare, the LOS magnetic gradient rapidly decreased by 0.02 G km^{-1} near the neutral line where the flare occurred. Meanwhile and almost at the same location, both horizontal and vertical shear flows suddenly enhanced. The vertical shear flow speed increased by up to 0.1 km s^{-1} and the horizontal shear flow speed increased by up to 0.2 km s^{-1}. In addition, the shear angles of both magnetic field and horizontal flow field increased after the flare along the flaring neutral line. The region undergoing these rapid changes is well correlated with the hard X-ray core of the flare.

It is not surprising that the flow speed increases with increasing height at the photospheric level, since one would expect that the plasma motions will be suppressed by magnetic field. From lower to higher altitude the strength of magnetic field drops, thus the suppression to the plasma motion decreases. In addition, the density of the plasma also decreases, therefore, the flow speed increases. While the decreasing of the flow speed with height in the shear motion regions gives us a hint that the mechanism of the shear motion is quite different from that of the general plasma motions in an active region. The observed result implies that the origin of the shear motion comes from a deep source in the subphotosphere.

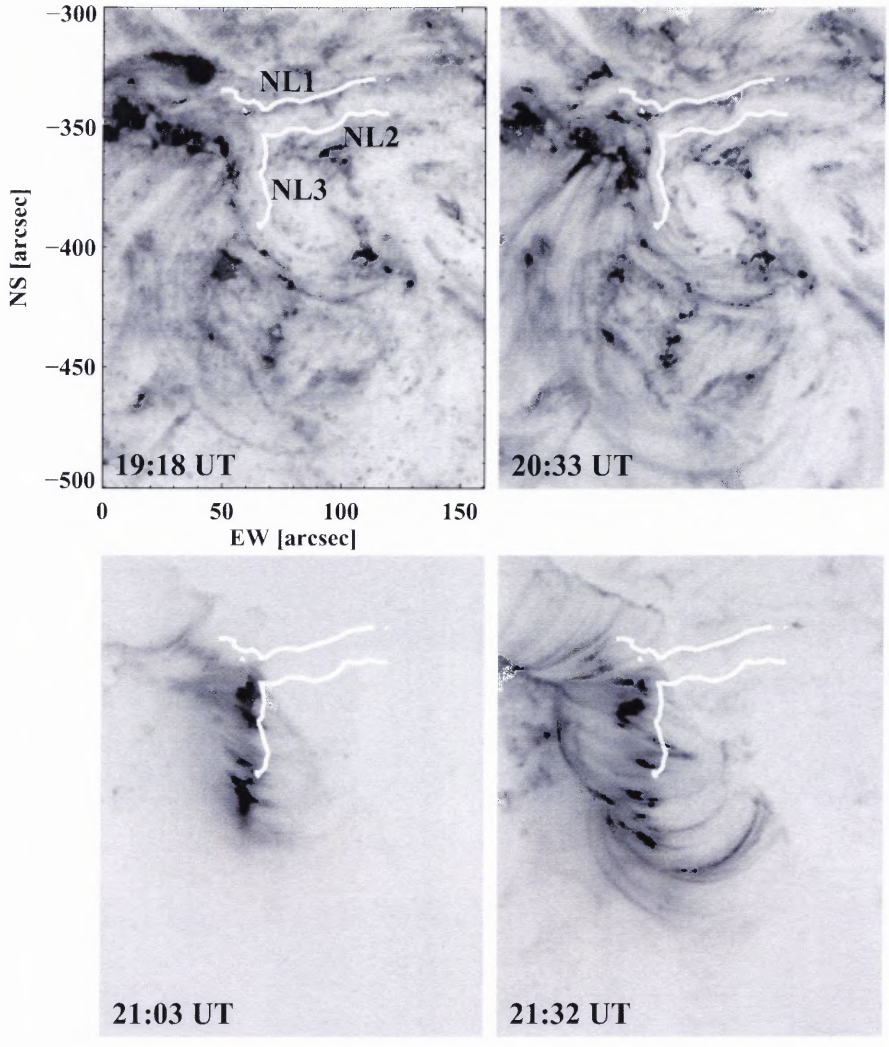

Figure 5.13 TRACE 195 Å negative images show the coronal morphology of active region NOAA 10486 at different times: the top two panels before the X10 flare and the bottom two panels after the flare. The FOV is $160'' \times 200''$. The three magnetic neutral lines that were defined in Figure 5.7 are superposed on each panel to visualize their positions.

The rapid enhancement of the shear flow right after the flare, for both horizontal and vertical flows as discussed in this chapter, and the increase of the magnetic shear revealed in Liu et al. (2005), are surprising because one would expect a decrease in the shear similar to the release of tectonic stress after an earthquake. One possible interpretation considers that the magnetic energy released during a flare is stored in the whole 3D magnetic system extending from photosphere to corona. Although

the overall magnetic stress will be relaxed after the flare, the local magnetic shear may increase. The shear motion of the photospheric and subphotospheric plasma plays an important role in building up the sheared magnetic configuration that stores magnetic free energy by dragging the footpoints of magnetic field lines along with it. The sheared configuration is transferred gradually from lower to higher altitude of the magnetic loops by the continuous shearing motion of the footpoints. As more and more magnetic shear thus magnetic free energy has been built up, more and more resistance to the shear flow is established by the increasing magnetic tension as a result of the overlying sheared magnetic configuration, which prevents further energy built-up. When the whole magnetic system is highly sheared from photosphere to corona, and the magnetic free energy therein is large enough, a critical point is reached, where the equilibrium breaks down and the flare occurs. The magnetic free energy is released and the whole magnetic system restores to a more potential configuration. Consequently, the resistance from the overlying non-potentially sheared magnetic loops acting on the shear flow in the photosphere is suddenly removed or reduced due to the overall relaxation of the magnetic field. Therefore, the photospheric shear flow can enhance to build up new magnetic shear for subsequent events. Due to the enhancement of the photospheric shear flow along the neutral line, the local magnetic shear also increases, which however cannot compete with the overall magnetic shear decrease in the whole flux system. In Figure 5.13, the TRACE 195 Å images show the magnetic field configurations in the lower corona at pre- and post-flare phases. The three photospheric neutral lines defined in Figure 5.7 are plotted in the proper positions. The magnetic field morphology changed drastically after the flare. The loops changed from more parallel to NL3 in pre-flare phase to more perpendicular to NL3 in post-flare phase, which implies that the strongly sheared pre-flare magnetic system was restructured by the flare into a relaxed configuration being close to the potential state. This may be one of the observational evidences to support the above

scenario. Several flare models (e.g., Antiochos, Devore, & Klimchuk 1999; Amari et al. 2000) also show that photospheric shear motions can be responsible for the energy build-up and flare eruption. The shear motions along the magnetic neutral line are usually used as one of the initial conditions. However, the questions where do the shear motions come from and how do they change after flares are not addressed in detail in these flare models.

Another possible interpretation for the observed shear flows and their enhancement after the flare considers the emergence of twisted or sheared flux tubes originating in the subphotosphere near the neutral line. The twisted or sheared emerging flux may carry enough magnetic free energy, some of it may be released during the flare and the rest may contribute to the increase of local shear. Based on 3D magnetohydrodynamic models, several authors (Manchester 2001; Fan 2001; Magara & Longcope 2001, 2003; Magara 2004; Manchester et al. 2004) have recently simulated the effects of an emerging twisted magnetic flux tube from the solar convection zone through the photosphere and chromosphere into the corona. In these simulations, the twisted flux tube is initially placed in the convection zone at a certain depth. The twisted part of the flux tube moves upward due to buoyancy force (Fan 2004). As the top of the flux tube reaches the photosphere, due to the magnetic tension force associated with the twisted field lines, a shear flow pattern develops on the photosphere, i.e., the plasma on the two sides of the polarity inversion line moves in the opposite direction (Manchester 2001; Fan 2001; Magara & Longcope 2003; Manchester et al. 2004). This self-induced shear transports the axial magnetic flux upward into the solar atmosphere, which is the main effect that leads to the eventual eruption of the flux tube into the corona (Manchester et al. 2004). However, how the shear flow changes with altitude and with the eruption is not discussed in detail in the simulations. The shear flow and the upflow pattern near the flaring neutral line revealed in this study provide observational evidence for the above models. Although

these models just consider a twisted flux emergence, a sheared flux emergence is expected to give a similar result, since both of them represent the stress in the magnetic field and the twist could be considered as the internal shear of a flux tube. Therefore, a conclusion can be made that the shear flow can be an indicator of a twisted or sheared flux emergence. Flux emergence is strongly related to triggering of the flare (e.g., Feynman & Martin 1995). The twisted or sheared flux may emerge more easily and quickly after the flare leading to the enhancement of the induced shear flow, which however needs further observations and simulations to confirm.

CHAPTER 6

SUMMARY OF THE DISSERTATION

The 65 cm telescope at BBSO and 76 cm DST at NSO/SP, in combination with AO and post-facto image reconstruction, have successfully provided high-resolution observations for much of this study. The high-resolution observations presented in these studies are some of the best data that have been taken at BBSO so far. Some new phenomena were discovered and some recent discoveries were confirmed by these studies.

A simple sunspot was tracked for six days during its decaying phase. Its evolution, morphology and flow field were studied in detail with speckle reconstructed images and two-dimensional spectroscopy. The total-to-umbral area ratio was calculated on each day during the decay phase of the sunspot, which is in agreement with others previous studies. Throughout the decaying process the penumbra decays faster than the umbra. The brightness contrast CLV was calculated for different sunspot parts in both white-light and line core images. The results show an increase in the relative brightness corresponding to a decrease in the contrast of the sunspot toward the limb, which suggests that the temperature of the sunspot increases with height faster than that of the quiet Sun. Furthermore, the rate of the umbral temperature increase with height is larger than that of the penumbra. The results challenge some semi-empirical umbra models, which predict the opposite behavior. However, they are consistent with the overall temperature profile with height of active regions.

In addition, three-dimensional flow fields were constructed using LCT and Dopplergrams. A distinct line of diverging flows divides the penumbra in the middle. Remnants of these diverging flows can still be found around the remaining pore when

the penumbra has completely vanished towards the end of the sunspot decay. This can be explained by the moving flux tube model (Schlichenmaier et al. 1998a,b) or giant convective rolls underneath the sunspots (e.g., Bovelet & Wiehr 2003). The results of this study favor the cluster (Parker 1979) over the monolithic (e.g., Cowling 1957) sunspot model. The Evershed flow and its skew toward the limb-side penumbra as well as unbalanced red and blue Dopplershifts were observed, which support a convex penumbral flow structure and downflows at the outer edge of the penumbra.

Rapid morphology change of active sunspots associated with flare occurrence is a topic that has recently attracted much attention. This phenomenon has been discovered by the BBSO research group and this study has expanded the initial findings and strengthened its theoretical foundation. Morphology changes include the rapid decay of penumbral segments and an enhancement of the central umbra right after a flare. By examining the evolution of the intensity and magnetic flux in these regions, a conclusion can be made that the changes are substantial and permanent. They are not transient and are quite different from the overall sunspot evolution. They are highly correlated in both time and location with flare occurrence. No such rapid changes have been found in the absence of flares, not even when using speckle-restored, high-resolution data. These rapid changes are interpreted in terms of magnetic reconnection, which alters the magnetic field topology during flares. The magnetic breakout model (Antiochos 1998; Antiochos, Devore, & Klimchuk 1999) was employed to successfully describe a flare/filament eruption/CME event and the associated rapid sunspot structure change.

Besides post-flare signatures in the photosphere, a pre-flare signature was also found in the flow field of sunspots, i.e., photospheric shear flows along flaring magnetic inversion lines. Strong and persistent shear flows were observed in a complex sunspot penumbra at least five hours before a major flare along the magnetic inversion line. These flows can be identified in near infrared, white-light, and G-band

images, which span the solar atmosphere from lower to higher photospheric layers. The flow structure remains the same, while the shear flow speed decreases, which suggest that the shear flow originates in subphotospheric regions. Shear flows are strongly connected to the occurrence of flares. They contribute to the build-up of magnetic shear and free energy. After the flare, a local enhancement of the photospheric magnetic shear and of the shear flow was observed, which can be the result of an overall release of the large-scale magnetic stress or a signature of a highly non-potential magnetic flux emergence near the flaring neutral line. Since the shear flow is also observed in flare-quiet sunspots, a conclusion can be made that the shear flow is associated with flare occurrence but it is not a sufficient condition for flaring.

The results of this Ph.D. thesis should be viewed in the context of the next generation of solar telescope such as the NST at BBSO. The modern off-axis 1.6-meter NST will replace the 65 cm vacuum reflector at BBSO in 2008. The current post-focus instruments can be seamlessly integrated into the new telescope. These instruments are carefully matched with NST's scientific objectives, which include small-scale dynamics of magnetic flux tubes, solar activity studies and space weather monitoring (Goode et al. 2003; Denker et al. 2006b). Using AO, image restoration and two-dimensional spectro-polarimetry will make large-aperture telescopes very powerful tools in studying the Sun. Some facets of high-resolution observations were presented in this work, which provide a first glimpse of the science to come with NST.

REFERENCES

Albregtsen, F., & Maltby, P. 1981a, Sol. Phys., 71, 269.

Albregtsen, F., & Maltby, P. 1981b, Sol. Phys., 74, 147.

Albregtsen, F., Joras, P. B., & Maltby, P. 1984, Sol. Phys., 90, 17.

Amari, T., Luciani, J. F., Mikic, Z., & Linker, J. 2000, ApJ, 529, L49.

Ambastha, A., Hagyard, M.J., & West, E.A. 1993, Sol. Phys., 148, 277.

Antiochos, S. K. 1998, ApJ, 502, L181.

Antiochos, S. K., Devore, C. R., & Klimchuk, J. A. 1999, ApJ, 510, 485.

Aulanier, G., Deluca, E.E., Antiochos, S. K., Mcmullen, R.A., & Golub, L. 2000, ApJ, 540, 1126.

Bovelet, B., & Wiehr, E. 2003, A&A, 412, 249.

Bray, R. J., & Loughhead, R. E. 1964, The International Astrophysics Series, London: Chapman & Hall.

Bray, R. J. 1981, Sol. Phys., 69, 3.

Cagigal, M. P., & Canales, V. F. 2000, Opt. Soc. Am. A 17, 903.

Cao, W., Xu, Y., Denker, C., & Wang, H. 2005, Proc. SPIE, 5881, 245.

Chaisson, E., & McMillan, S. 2002: *Astronomy Today* (4th edition) Prentice-Hall, Upper Saddle River, New Jersey.

Chapman, G. A., Dobias, J. J., Preminger, D. G., & Walton, S. R. 2003, Geophys. Res. Lett., 30, 27.

Chen, J., Wang, H., Zirin, H., & Ai, G. 1994, Sol. Phys., 154, 261.

Chen, W., Liu, C., Song, H., Deng, N., Tan, C., & Wang, H. 2007, ApJ, submitted.

Choudhuri, A. R. 1986, ApJ, 302, 809.

Cowling, T. G. 1957, Interscience, New York.

de Boer, C. R. 1993, Ph.D. Thesis, Georg-August Universität Göttingen, Germany.

de Boer, C. R. 1996, A&ASS, 120, 195.

Deng, N., Liu, C., Yang, G., Wang, H., & Denker, C. 2005, ApJ, 623, 1195.

Deng, N., Xu, Y., Yang, G., Cao, W., Liu, C., Rimmele, T. R., Wang, H., & Denker, C. 2006, ApJ, 644, 1278.

Deng, N., Tritschler, A., Liu, C., Wang, H., & Denker, C. 2007, ApJ, in preparation.

Denker, C. 1998, Sol. Phys., 180, 81.

Denker, C., & Wang, H. 1998, ApJ, 502, 493.

Denker, C., Johannesson, A., Goode, P. R., Marquette, W., Wang, H., & Zirin, H. 1998, Sol. Phys., 184, 87.

Denker, C., Yang, G., & Wang, H. 2001, Sol. Phys., 202, 63.

Denker, C., Didkovsky, L., Ma, J., Shumko, S., Varsik, J., Wang, J., Wang, H., & Goode, P. R. 2003a, Astron. Nachr., 324/4, 332.

Denker, C., Ma, J., Wang, J., Didkovsky, L. V., Varsik, J. R., Wang, H., & Goode, P. R. 2003b, Proc. SPIE, 4853, 223.

Denker, C., Mascarinas, D., Xu, Y., Cao, W., Yang, G., Wang, H., Goode, P. R., & Rimmele, T. 2004a, Sol. Phys., 227, 217.

Denker, C., Tritschler, A., & Löfdahl, M. 2004b, Encyclopedia of Optical Engineering, R. Barry Johnson and Ronald G. Driggers (eds.), Marcel Dekker Inc., New York.

Denker, C. 2005, Astronomy and Astrophysics Space Science Library, 320, 1.

Denker, C., & Tritschler, A. 2005, PASP, 117/838, 1435.

Denker, C., Mascarinas, D., Xu, Y., Cao, W., Yang, G., Wang, H., Goode, P. R., & Rimmele, T. 2005, Sol. Phys., 227, 217.

Denker, C., Tritschler, A., Rimmele, T., Richards, K., Hegwer, S., & Wöger, F. 2006a, PASP, submitted.

Denker, C., Goode, P. R., Ren, D., Saadeghvaziri, M. A., Verdoni, A. P., Wang, H., & 14 co-authors 2006b, Proc. SPIE, 6267.

Denker, C., Deng, N., Yurchyshyn, V., & Tritschler, A. 2007a, Sol. Phys., submitted.

Denker, C., Deng, N., Rimmele, T., Tritschler, A, & Verdoni, A. 2007b, Sol. Phys., submitted.

Didkovsky, L. V., Dolgushyn, A., Marquette, W., Nenow, J., Varsik, J., Goode, P. R., & 7 co-authors 2003, Proc. SPIE, 4853, 630.

Domingo, V., Fleck, B., & Poland, A. I. 1995, Sol. Phys., 162, 1.

Duvall, T. L. J., D'Silva, S., Jefferies, S. M., Harvey, J. W., & Schou, J. 1996, Nature, 379, 235.

Evershed, J. 1909, Obs., 32, 291.

Fan, Y. 2001, ApJ, 554, L111.

Fan, Y. 2004, Living Rev. Sol. Phys., 1, 1.

Feynman, J., & Martin, S. F. 1995, JGR, 100, 3355.

Freeland, S. L., & Handy, B. N. 1998, Sol. Phys., 182, 497.

Fried, D. L. 1966, JOSA, 56, 1372.

Fried, D. L. 1982, JOSA, 72, 52.

Gilbert, H. R., Holzer, T. E., Burkepile, J. T., & Hundhausen, A. J. 2000, ApJ, 537, 503.

Gizon, L., Duvall, T. L., Jr., & Larsen, R. M. 2000, J. Astrophys. Astron., 21, 339.

Goode, P. R., Denker, C., Didkovsky, L. I., Kuhn, J. R., & Wang, H. 2003, J. Korean Astron. Soc., 36, 125.

Gosling, J. T., Hildner, E., MacQueen, R. M., Munro, R. H., Poland, A. I., & Ross, C. L. 1976, Sol. Phys., 48, 389.

Haber, D. A., Hindman, B. W., Toomre, J., Bogart, R. S., & Thompson, M. J. 2004, ESA SP-559: SOHO 14 Helio- and Asteroseismology: Towards a Golden Future, 14, 148

Hagyard, M. J., Start, B.A., & Venkatakrishnan, P. 1999, Sol. Phys.184, 133.

Hale, G. E. 1909, PASP, 21, 205.

Hale, G. E., Seares, F. H., van Maanen, A., & Ellerman, F. 1918, ApJ, 47, 206.

Handy, B. N., Acton, L. W., Kankelborg, C. C., Wolfson, C. J., Akin, D. J., Bruner, M. E., & 42 co-authors 1999, Sol. Phys.187, 229.

Harvey, K. L., & Harvey, J. W. 1976, Sol. Phys., 47, 233.

Howard, R. A., Sheeley, N. R., Jr., Michels, D. J., & Koomen, M. J. 1985, JGR, 90, 8173.

Howard, R., & Murdin, P. 2000, Enc. Astron. Astrophys., 2297, 3173.

Hurlburt, N. E., & Rucklidge, A. M. 2000, MNRAS, 314, 793.

Keil, S. L., Balasubramaniam, K. S., Bernasconi, P., Smaldone, L. A., & Cauzzi, G. 1994, ASP Conf. Ser., 68, 265.

Keil, S. L., Rimmele, T., Keller, C. U., Hill, F., Radick, R. R., Oschmann, J. M., & 5 co-authors 2003, Proc. SPIE, 4853, 240.

Kitai, R. 1986, Sol. Phys., 104, 287.

Knobloch, E., & Weiss, N. O. 1984, MNRAS, 207, 203.

Kollatschny, W., Wiehr, E., Stellmacher, G., & Falipou, M. A. 1980, A&A, 86, 245.

Kopp, R. A., & Pneuman, G.W. 1976, Sol. Phys., 50, 85.

Korff, D. 1973, JOSA, 63, 971.

Kosovichev, A. G. 1996, ApJ, 461, L55.

Kosovichev, A. G., & Zharkova, V. V. 1999, Sol. Phys., 190, 459.

Kosovichev, A. G., & Zharkova, V. V. 2001, ApJ, 550, L105.

Kosovichev, A. G. 2002, Astron. Nachr., 323, 186.

Kosovichev, A. G., Duvall Jr., T. L., Birch, A. C., Gizon, L., Scherrer, P. H., & Zhao, J. 2002, Adv. Space Res., 29/12, 1899.

Kosovichev, A. G., Duvall, T. L., & Zhao, J. 2004, AGU Fall Meeting Abstracts, A1144.

Krall, K. R., Smith, J. B., Hagyard, M. J., West, E. A., & Cummings, N. P. 1982, Sol. Phys., 79, 59.

Kumar, M. 2006, Space Weather, 3/3, 14.

Kurokawa, H., Wang, T., & Ishii, T.T. 2002, ApJ, 572, 598.

Künzel, H. 1960, Astron. Nachr., 285, 271.

Labeyrie, A., 1970, A&A, 6, 85.

Leka, K. D., Canfield, R. C., McClymont, A. N., & van Driel-Gesztelyi, L. 1996, ApJ, 462, 547.

Leka, K. D., & Skumanich, A. 1998, ApJ, 507, 454.

Lin, R. P., et al. 2002, Sol. Phys., 210, 3.

Linton, M. G., Fisher, G. H., Dahlburg, R. B., & Fan, Y. 1999, ApJ, 522, 1190.

Lites, B. W., Thomas, J. H., Bogdan, T. J., & Cally, P. S. 1998, ApJ, 497, 464.

Lites, B. W., Socas-Navarro, H., Skumanich, A., & Shimizu, T. 2002, ApJ, 575, 1131.

Lites, B. W., Scharmer, G. B., Berger, T. E., & Title, A. M. 2004, Sol. Phys., 221, 65.

Liu, C., Deng, N., Liu, Y., Falconer, D., Goode, P. R., Denker, C., & Wang, H. 2005, ApJ, 622, 722.

Liu, C., Lee, J., Deng, N., Gary, D., & Wang, H. 2006, ApJ, 642, 1205.

Löfdahl, M. G., van Noort, M. J., & Denker, C. 2007, in: Modern Solar Facilities - Advanced Solar Science; Kneer, F., Puschmann, K. G., Wittmann, A. D. (eds.); Universitätsverlag Göttingen.

Lohmann, A. W., Weigelt, G. P., & Wirnitzer, B., 1983, Appl. Opt., 22, 4028.

Lynch, B. J., Antiochos, S. K., MacNeice, P. J., Zurbuchen, T. H., & Fisk, L. A. 2004, ApJ, 617, 589L.

Magara, T., & Longcope, D. W. 2001, ApJ, 559, L55.

Magara, T., & Longcope, D. W. 2003, ApJ, 586, 630.

Magara, T. 2004, ApJ, 605, 480.

Maltby, P., & Mykland, N. 1969, Sol. Phys., 8, 23.

Maltby, P. 1970, Sol. Phys., 13, 312.

Maltby, P. 1972, Sol. Phys., 26, 76.

Maltby, P., Avrett, E. H., Carlsson, M., Kjeldseth-Moe, O., Kurucz, R. L., & Loeser, R. 1986, ApJ, 306, 284.

Manchester, W. I. 2001, ApJ, 547, 503.

Manchester, W., Gombosi, T., DeZeeuw, D., & Fan, Y. 2004, ApJ, 610, 588.

Martínez Pillet, V. 2002, Astron. Nachr., 323, 342.

Martres, M. J., Rayrole, J., Ribes, E., Semel, M., & Soru-Escaut, I. 1974, in *Flare Related Magnetic Field Dynamics Conference*, Boulder, Colorado, p. 333.

Martres, M. J., & Soru-Escaut, I. 1977, Sol. Phys., 53, 225.

McIntosh, P. S. 1981, The Physics of Sunspots, 7.

Metcalf, T. R., Leka, K. D., & Mickey, D. L. 2005, ApJ, 623, L53.

Meunier, N., & Kosovichev, A. 2003, A&A, 412, 541.

Miller, J. A., Cargill, P. J., Emslie, A. G., Holman, G. D., Dennis, B. R., LaRosa, T. N., & 3 co-authors 1997, JGR, 102, 14631.

Molowny-Horas, R. 1994, Sol. Phys., 154, 29.

Moore, R. L., Hurford, G. J., Jones, H. P., & Kane, S. R. 1984, ApJ, 276, 379.

Moore, R. L., & Roumeliotis, G. 1992, Eruptive Solar Flares, Z. Svestka, B. V. Jackson, & M. E. Machado (eds.), Springer, Berlin.

Muller, R. 1976, Sol. Phys., 48, 101.

Munro, R. H., Gosling, J. T., Hildner, E., MacQueen, R. M., Poland, A. I., & Ross, C. L. 1979, Sol. Phys., 61, 201.

November, L. J., Simon, G. W., Tarbell, T. D., Title, A. M., & Ferguson, S. H. 1986, in: G. Athay and D. S. Spicer (eds.), Proc. Theoretical Problems in High Resolution Solar Physics II, p. 121.

November, L. J., & Simon, G. W. 1988, ApJ, 333, 427.

Parker, E. N. 1975, Sol. Phys., 40, 291.

Parker, E. N. 1979, ApJ, 230, 905.

Parker, E. N. 1992, ApJ, 390, 290.

Patty, S. R., & Hagyard, M. J. 1986, Sol. Phys., 103, 111.

Pehlemann, E., & von der Lühe, O., 1989, A&A, 216, 333.

Potts, H. E., Barrett, R. K., & Diver, D. A. 2003, Sol. Phys., 217, 69.

Potts, H. E., Barrett, R. K., & Diver, D. A. 2004, A&A, 424, 253.

Priest, E. R. 1982, Solar Magneto-hydrodynamics, Reidel, Dordrecht.

Priest, E. R., & Forbes, T. G. 1986, JGR, 91, 5579.

Puschmann, K., & Sailer M. 2006, A&A, 454, 1011.

Qiu, J., & Gary, D. E. 2003, ApJ, 599, 615.

Ren, D., Hegwer, S. L., Rimmele, T. R., Didkovsky, L. V., Goode, P. R. 2003, Proc. SPIE, 4853, 593.

Rimmele, T. R. 1995, ApJ, 445, 511.

Rimmele, T. R. 2000, Proc. SPIE, 4007, 218.

Rimmele, T. R., Richards, K., Hegwer, S. L., Ren, D., Fletcher, S., Gregory, S., & 5 co-authors 2003, Proc. SPIE, 4839, 635.

Rimmele, T. R. 2004, ApJ, 604, 906.

Rimmele, T. R., Richards, K., Hegwer, S., Fletcher, S., Gregory, S., Moretto, G., and 7 co- authors 2004, Proc. SPIE, 5171, 179.

Rimmele, T., & Marino, J. 2006, ApJ, 646, 593.

Rödberg, H. 1966, Nature, 211, 394.

Roddier, F. 1981, in: Progress in Optics 19, E. Wolf (ed.), North-Holland Publishing Company, Amsterdam, pp. 281-376.

Roddier, F. 1999, Imaging through the Atmosphere. in: Adaptive Optics in Astronomy, F. Roddier (ed.), Cambridge University Press, Cambridge, UK, pp. 9-22.

Sakurai, T., & Hiei, E. 1996, Adv. Space Res., 17, 91.

Schatten, K. H. 1993, JGR, 98, 18907.

Scherrer, P. H., Bogart, R. S., Bush, R. I., Hoeksema, J. T., Kosovichev, A. G., Schou, J., & 7 co-authors 1995, Sol. Phys., 162, 129.

Schlichenmaier, R., Jahn, K., & Schmidt, H. U. 1998a, ApJ, 493, L121.

Schlichenmaier, R., Jahn, K., & Schmidt, H. U. 1998b, A&A, 337, 897.

Schlichenmaier, R., & Schmidt, W. 1999, A&A, 349, L37.

Schlichenmaier, R., & Schmidt, W. 2000, A&A, 358, 1122.

Schmidt, W., & Schlichenmaier, R. 2000, A&A, 364, 829.

Schrijver, C. J., Title, A. M., Berger, T. E., Fletcher, L., Hurlburt, N. E., Nightingale, R. W., & 11 co-authors 1999, Sol. Phys., 187, 261.

Schröter, E. H. 1962, Z. Astrophys., 56, 183.

Schuck, P. W. 2006, ApJ, 646, 1358.

Severny, A. B. 1958, Izv. Krym. Astr. Obs., 20, 22.

Severny, A. B. 1964, ARA&A, 2, 363.

Shine, R. A., Title, A. M., Tarbell, T. D., Smith, K., Frank, Z. A., & Scharmer, G. 1994, ApJ, 430, 413.

Shine, R. A., Simon, G. W., & Hurlburt, N. E. 2000, Sol. Phys., 193, 313.

Sobotka, M., Brandt, P. N., & Simon, G. W. 1999, A&A, 348, 621.

Solanki, S. K. 2003, A&A Rev., 11, 153.

Somov, B. V., Kosugi, T., Hudson, H. S., & Sakao, T., 2002, ApJ, 579, 863.

Spirock, T., Denker, C., Chen, H., Chae, J., Qiu, J., Varsik, J., Wang, H., Goode, P. R., & Marquette, W. 2001, ASP Conf. Ser., 236, 65.

Spirock, T. J., Yurchychyn, V., & Wang, H. 2002, ApJ, 572, 1072.

St. Cyr, O. C., Burkepile, J. T., Hundhausen, A. J., & Lecinski, A. R. 1999, JGR, 104, 12493.

Stein, R. F., & Nordlund, A. 1998, Astrophys. J. 499, 914.

Sturrock, P. A. 1989, Sol. Phys., 121, 387.

Svestka, Z. 2001, Space Sci. Rev., 95, 135.

Thomas, J. H., & Weiss, N. O. 2004, ARA&A, 42, 517.

Toenjes, K., & Woehl, H. 1982, Sol. Phys., 75, 63.

van Ballegooijen, A. A., & Martens, P. C. H. 1989, ApJ, 343, 971.

van Driel-Gesztelyi, L. 2005, Astronomy and Astrophysics Space Science Library, 320, 57.

Volkmer, R., von der Lühe, O., Kneer, F., Staude, J., Hofmann, A., Schmidt, W., & 5 co-authors 2003, Proc. SPIE, 4853, 360.

von der Lühe, O. 1984, JOSA, 1, 510.

Vrsnak, B. 1990, Sol. Phys., 129, 295.

Vrsnak, B., Ruzdjak, V., & Rompolt, B. 1991, Sol. Phys., 136, 151.

Vrsnak, B. 2005, Astronomy and Astrophysics Space Science Library, 320, 27.

Wang, H., Tang, F., Zirin, H., & Ai, G. 1991, ApJ, 380, 382.

Wang, H., & Zirin, H. 1992, Sol. Phys., 140, 41.

Wang, H., Ewell, M. W., Zirin, H., & Ai, G. 1994, ApJ, 424, 436.

Wang, H., Spirock, T., Goode, P. R., Lee, C., Zirin, H., & Kosonocky, W. 1998, ApJ, 495, 957.

Wang, H., Ji, H., Schmahl, E. J., Qiu, J., Liu, C., & Deng, N. 2002a, ApJ, 580, L177.

Wang, H., Spirock, T. J., Qiu, J., Ji, H., Yurchychyn, V., Moon, Y.-J., Denker, C., & Goode, P. R. 2002b, ApJ, 576, 497.

Wang, H., Liu, C., Qiu, J., Deng, N., Goode, P. R., & Denker, C. 2004a, ApJ, 601, L195.

Wang, H., Qiu, J., Jing, J., Spirock, T.J., Yurchyshyn, V., Abramenko, V., Ji, H., & Goode, P.R. 2004b, ApJ, 605, 931.

Wang, H., Liu, C., Deng, Y., Zhang, H. 2005, ApJ, 627, 1031.

Webb, D. F., & Hundhausen, A. J. 1987, Sol. Phys., 108, 383.

Weigelt, G. P., 1977, Opt. Comm., 21, 55.

Weigelt, G., & Wirnitzer, B., 1983, Opt. Lett., 8, 389.

Weiss, N. O., Brownjohn, D. P., Matthews, P. C., & Proctor, M. R. E. 1996, MNRAS, 283, 1153.

Westendorp Plaza, C., del Toro Iniesta, J. C., Ruiz Cobo, B., Martinez Pillet, V., Lites, B. W., & Skumanich, A. 1997, Nature, 389, 47.

Wiehr, E., Bovelet, B., & Hirzberger, J. 2004, A&A, 422, L63.

Wilken, V., de Boer, C. R., Denker, C., & Kneer, F. 1997, A&A, 325, 819.

Wittmann, A., & Schröter, E. H. 1969, Sol. Phys., 10, 357.

Wöhl, H., Wittmann, A., & Schröter, E. H. 1970, Sol. Phys., 13, 104.

Xu, Y., Cao, W., Liu, C., Yang, G., Qiu, J., Jing, J., Denker, C., & Wang, H. 2004, ApJ, 607, L131.

Yang, G., Xu, Y., Wang, H., & Denker, C. 2003, ApJ, 597, 1190.

Yang, G., Xu, Y., Cao, W., Wang, H., Denker, C., & Rimmele, T. R. 2004, ApJ, 617, L151.

Yurchyshyn, V.B., Wang, H., Abramenko, V., Spirock, T.J., & Krucker, S. 2004, ApJ, 605, 546.

Zhang, H. 1995, A&A, 297, 869.

Zhang, J., Dere, K. P., Howard, R. A., Kundu, M. R., & White, S. M. 2001, ApJ, 559, 452.

Zhao, J., Kosovichev, A. G., & Duvall, T. L., Jr. 2001, ApJ, 557, 384.

Zhao, J., & Kosovichev, A. G. 2003, ApJ, 591, 446.

Zhou, G., Wang, J., & Cao, Z. 2003, A&A, 397, 1057.

Zirin, H., & Liggett, M. A. 1987, Sol. Phys., 113, 267.

Zirin, H. 1988, Astrophysics of the Sun. Cambridge University Press.

Zirin, H., & Wang, H. 1989, Sol. Phys., 119, 245.

Zvereva, A. M., & Severny, A. B. 1970, Izv. Krymskoi Astrofiz. Obs., 41-42, 97.

Zwaan, C. 1968, ARA&A, 6, 135.

Zwaan, C. 1974, Sol. Phys., 37, 99.

Zwaan, C. 1975, Sol. Phys., 45, 115.

Zwaan, C. 1992, NATO ASIC Proc., 375, 75.